
# TOMOGRAPHIC SCANNING IMAGERS

BY

HARALD HOVLAND

PHILOSOPHIAE DOCTOR (PHD) THESIS

SUBMITTED TO THE FACULTY OF MATHEMATICS AND NATURAL SCIENCES

UNIVERSITY OF OSLO

JANUARY 2015

*Series of dissertations submitted to the*
*Faculty of Mathematics and Natural Sciences, University of Oslo*
*No. 1638*

ISSN 1501-7710



Cover: Hanne Baadsgaard Utigard.
Printed in Norway: AIT Oslo AS.

Produced in co-operation with Akademika Publishing.
The thesis is produced by Akademika Publishing merely in connection with the thesis defence. Kindly direct all inquiries regarding the thesis to the copyright holder or the unit which grants the doctorate.

# Abstract

The tomographic scanning (TOSCA) family of imagers collects their raw signals from a line-shaped sensitive area scanned across the image plane. An image is then formed by tomographic reconstruction techniques. A TOSCA imager can be implemented by scanning knife edges, thin slots or thin line detectors across the image plane, repeating the scan at regularly distributed angular intervals.

This thesis describes the conception, theory and practical realization of the TOSCA imaging technique, originally based on a simple hot spot scanner. The treatment incudes analysis of noise characteristics, sensitivity to alignment errors and errors in the scanning process, such as temporal offset and jitter. Detailed simulations are used as a tool to establish the different mechanisms that can degrade the image and the extent of their effect.

Several experimental demonstrators are presented, operating in the visible, short wave infrared and mid wave infrared spectral domains, and also multispectral operation to demonstrate special features of the TOSCA imager system. Experimental noise measurements are shown to be in good agreement with theory.

The reconstruction algorithms of these systems have demonstrated ability to handle illumination intensity modulation frequencies higher than the corresponding frame rate.

It is demonstrated that a TOSCA imager can be created using simple and low cost components and consumer grade 3D-printers, opening up for the development of low-cost infrared imagers for use in low-cost survey drones, or for educational purposes.

# Preface

This thesis has been submitted to the Faculty of Mathematics and Natural Sciences at the University of Oslo (UiO) in partial fulfilment of the requirements for the degree of Philosophiae Doctor (Ph. D.).

The research has been fully funded by the Norwegian Defence Research Establishment (FFI) under the P1008 OPEK, P1107 OPEK II and P1248 OPEK III projects. The research has been conducted at FFI during the period 2005-2015 under the supervision of Professor Svein Erik Hamran at the Department of Geosciences and the Department of Informatics at UiO, and the co-supervision of chief scientist, Dr. Torbjørn Skauli at the Land and Air Systems Division, FFI.

# Acknowledgements

As can be seen from the publication list, I feature as single author for all the papers. I am nevertheless indebted to several people for helping me out with this work. First and foremost I would like to thank Professor Svein Erik Hamran and Dr. Torbjørn Skauli, for the many fruitful discussions and able guidance during the work. Torbjørn and Dr. Alexander Wold have helped me by reading through the thesis manuscript and improving both the language and the precision of the thesis. I would also like to thank other colleagues at FFI, in particular many of the people working in the OPEK projects. Of these, Dr. Jonas Moen deserves extra credit for helping me with brainstorming in the early days of the work, and Dr. Jan Kenneth Bekkeng who assisted me with the implementation of real-time signal acquisition in LabView®. I would also like to thank my project manager, Mr. Tor-Odd Høydal, for supporting my work.

At FFI we have a lot of talented persons that help bring problems towards optimal solutions. For this work, I would like to thank in particular Dr. Stéphane Nicolas for helping me with optimizing the optical configurations using Zemax® software, and Mr. Sverre Dyrkorn (currently at AIM Norway) and Mr. Pål Halvorsen for bringing some of my conceptual sketches into practical technical drawings using SolidWorks®, and the other people at the Mechanical Design and Workshop for producing components and assembling

some of the experimental imagers. I am indebted to Mr. Jan Rune Nilssen for enjoyable and fruitful discussions on 3D-printers. I am also indebted to Dr. Roy Edgar Hansen, Mrs. Nina Ødegaard, Mr. Hans Erling Torkildsen and Dr. Torbjørn Skauli (again) for kindly providing me with illustrative images that have been used in the thesis.

From outside FFI I would like to thank Major Øystein Bringe and Lieutenant Colonel Tom-Ivar Punsvik, for their support of this work. I would also like to thank GE Healthcare for providing me with tomography images produced by their equipment.

Finally, I would like to thank my family for their patience with me during late working hours, and their lasting inspiration, encouragement, support, love and care.

Harald Hovland
January, 2015

# Abbreviations

The following list contains the abbreviations used in this work:

- 2D, 3D - 2/3-dimensional
- AC - Alternating current
- AM - Amplitude modulation
- CCD - Charge coupled device
- CMOS - Complementary metal oxide semiconductor
- CT - Computer tomography
- DC - Direct current
- EK, EW - Elektronisk krigføring (electronic warfare)
- FFI - Forsvarets forskningsinstitutt (Norwegian Defence Research Establishment)
- FM - Frequency modulation
- FOV - Field of view
- FPA - Focal plane array
- Hz - Hertz
- InGaAs - Indium gallium arsenide
- InSb - Indium antimonide

- IR - Infrared
- MCT - Mercury cadmium telluride
- mK - millikelvin
- OPEK - Operativ EK støtte til Forsvaret (Operational EW support for the Norwegian Defence)
- PET - Positron-electron tomography
- RGB - Red green blue
- RGBG - Red green blue green
- ROIC - Read-out integrated circuit
- SAR - Synthetic aperture radar
- SAS - Synthetic aperture sonar
- Si - Silicon
- SLM - Spatial light modulator
- SPIFI - Spatial frequency modulation for imaging
- THz - terahertz
- TOSCA - Tomographic scanning
- UiO - Universitetet i Oslo (University of Oslo)
- Å - Ångstrøm

# List of publications

I. Harald Hovland, (2004), "Tomographic scanning imaging seeker," SPIE Proceedings Vol. 5430, Acquisition, Tracking and Pointing XVIII, pp. 58-64, SPIE 2004.

II. Harald Hovland, (2007), "Optimisation of the tomographic scanning (TOSCA) imager," SPIE Proceedings Vol. 6569, Acquisition, Tracking, Pointing, and Laser Systems Technologies XXI, paper 65690I, SPIE 2007.

III. Harald Hovland, (2008), "Tomographic scanning imager", Optics Express, Volume 17, Number 4, pp. 11371-11387, (2008).

IV. Harald Hovland, (2013), "Construction and demonstration of a multi-spectral tomographic scanning imager (TOSCA)", Optics Express, Volume 21, Number 4, pp. 4688-4702, (2013).

V. Harald Hovland, (2014), "Experimental tomographic scanning (TOSCA) imagers," SPIE Proceedings Vol. 9070, Infrared Technology and Applications XL, paper 90700H, SPIE 2014.

VI. Harald Hovland, (2014), "Spin scan tomographic array-based imager", Optics Express, Volume 22, Number 6, pp. 31999-32015, (2014).

# Contents

## Publications

# Chapter 1 – Introduction

This chapter provides an overview of the thesis, explains the motivation of the work and the methodology used herein, and outlines the structure of the thesis.

## 1.1 Thesis Context and Motivation

The starting point of this work was a detailed and fundamental study of a class of hot spot trackers called conical scan reticle trackers, schematically depicted in figure 1.1. A simple scenario consists of a stationary point source on a homogeneous background. The image of the point source (often called a hot spot) will move with a constant speed in a circular movement because of the rotating, tilted secondary mirror. A fixed reticle, a mask with alternating transparent and non-transparent fields, is positioned in the centre of the focal plane. Behind the reticle is a detector that detects the light that passes through the transparent fields on the mask, creating an electric signal. If the point source is centred, its image will move in a centred, regular circular movement, creating a fixed frequency signal, as shown with the green curve. This occurs because the point source image crosses the sector limits at regular intervals. The image of an off-axis point source, on the other hand, crosses the sector limits at irregular intervals, as seen with the blue curve. The sensor generates a frequency modulated signal, where the modulation determines both the azimuth and off-axis angles of the point source relative to the optical axis.

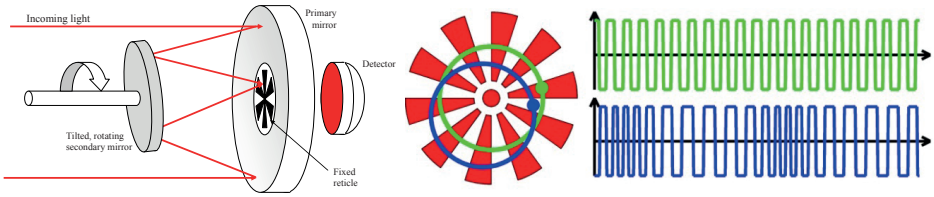


Figure 1.1. Sketch of a conical scan reticle tracker (left), and the corresponding scan pattern (middle) and resulting detector signals (right). Incoming light (red lines) is focused and scanned (nutated) in a circular movement on a fixed reticle consisting of transparent and non-transparent sectors. The image orientation remains fixed. Light passing the transparent sectors hits the detector, creating a modulated signal. The signal from a centred (green circle and curve) hot spot produces a regular, fixed-frequency signal. The de-centred (blue circle and curve) hot spot produces a modulated frequency signal. Position is given by modulation depth and phase.

These hot spot trackers can therefore localize a single stationary hot spot on a homogeneous background. But what information can the system convey when facing a more complex scenario than just a single point source?

Figure 1.2. Image from the first experimental TOSCA video recording, showing the author's face.

The investigation of this question revealed that the system did in fact have inherent imaging properties. This motivated the investigations presented in this thesis. The nature of these imaging properties has been studied, and it has been demonstrated that useful images can be produced with a realistic setup. An image from the first experimental TOSCA video made is shown in figure 1.2. As it became clear during the investigations that imaging is indeed possible, the scope broadened further to optimize system performance and to find alternative tomographic scanning (TOSCA) imager solutions and concepts.

Although the departure point had an academic military aspect, TOSCA imaging systems have a potential in many civilian applications, especially as low cost imagers. Figure 1.3 shows a low cost infrared TOSCA imager produced during this work, with mainly low cost components and parts produced using a three-dimensional (3D) printer. This kind of imager is well suited for educational purposes. Another potential application is low cost, airborne drones designed to fly into dangerous or hard to reach areas.

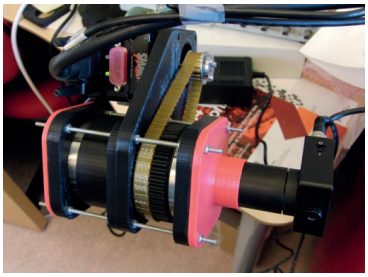

Figure 1.3. Low cost infrared TOSCA imager with many 3D-printed components.

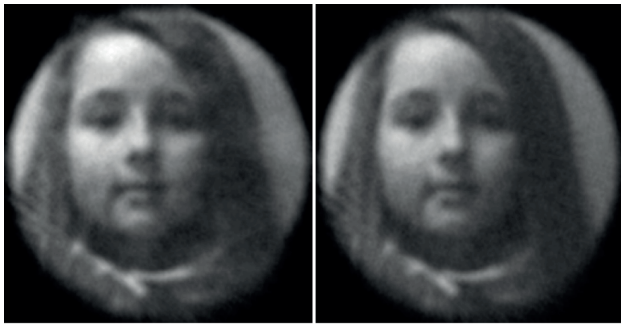

(a) (b)

Figure 1.4. “Victoria” recording made with indoors illumination. The indoors illumination features 100 Hz modulation, the recording is made with a 12 Hz frame rate. Image (a) was reconstructed without, and (b) was reconstructed with automatic compensation of the illumination modulation. Note the correction of the apparently wavy hair.

The TOSCA imager concept also has the ability to handle scenes with strongly and rapidly varying illumination conditions, even with modulation rates significantly faster than the frame rate. This can be challenging for both scanning and staring imagers, both when the whole scene illumination varies and when the scene contains blinking point sources. It has been demonstrated that the TOSCA imagers can detect, characterize and compensate for such variations. Figure 1.4 shows a recording where modulation frequencies an order of magnitude higher than the frame rate has been compensated for automatically.

Multispectral imaging has the advantage of being able to identify objects using its spectral signature. This can be achieved even at ranges where a clear geometrical shape is not yet discernible, including the extreme case of subpixel object detection. This is particularly useful in search and rescue missions, where a single airborne platform can monitor a wide swath to cover large areas per unit time. The TOSCA imager is shown to have characteristics particularly well suited for multispectral imaging.

In this work, demonstrators have been made in the visible as well as the short and mid-wave infrared spectral domain, where two-dimensional (2D) focal plane arrays are available. It is clear, however, that in some cases, useful staring focal plane array configurations may not be available. This includes cases where the radiation, or some of its constituents, may disable electronics embedded in the focal plane. It also includes cases when the material does not allow for photovoltaic operation, and photoconductive mode of small pixel element configurations is impractical or in any other way inappropriate. Notably, large focal plane arrays with photoconductive detectors often have thermal issues.

## 1.2 Research Objectives and Method

The primary objectives of this thesis are the following:

- Examine the properties of different imaging concepts based on the reconstruction of signals from reticle or line detector based scanning sensors.
- Demonstrate that proper imaging can be extracted from realistic sensor configurations.

The methodologies pursued have been the following:

- Developing missing theory where necessary to fuse (reticle based) hot spot tracker technology with tomographic reconstruction.
- Developing detailed digital models to be able to isolate the effect of specific error mechanisms, both to quantify these and to enable recognition of these errors in experimental demonstrators.
- Determine theoretical performance in terms of resolution, artefacts and noise through both analytical methods and simulations, using performance figures of real components.
- Perform simulations to examine distortion due to various mechanical and electromechanical errors, such as optical misalignment and scan speed variability.
- Characterize performance of actual systems by developing experimental setups and performing controlled measurements. This can be used to validate simulations and evaluate system performance of real sensors, discover effects not revealed through simulations and highlight the balance of various trade-offs in such systems.

## 1.3 Thesis Organization

This thesis is a collection of publications. The six research publications, three of which are conference proceedings, are included in their original format at the end (with minor formatting adjustments to improve readability), and constitutes the research part of the thesis.

After the introduction in chapter 1, chapter 2 in the first part of the thesis starts with a general background with a selection of topics to put this work in context, namely hot spot trackers, semi-imaging and imaging systems, tomography, and multi- and hyperspectral imaging. Chapter 3 starts with a brief overview of the publications and explains how they are related. The subsequent subchapters summarize and explain what have been achieved in the work with the main features and results of each of the publications. Finally,

conclusions are drawn in chapter 4 as to the advances this work has resulted in, and possible future work is described.

# Chapter 2 – Background

This chapter covers scientific or engineering fields relevant to the development or assessment of the TOSCA imagers both from a historical, theoretical and practical point of view, or alternative technologies that can put these imagers in perspective.

## 2.1 Hot Spot Trackers

Hot spot trackers represent a family of devices designed to locate and track a single bright point target in an otherwise (relatively) simple scene, possibly with a prior manual or automatic cueing. Such trackers are used to locate and track intense light sources such as the sun or more distant stars, or reflected laser light.

The infrared part of the light spectrum was discovered by Herschel in 1800 [1], and the potential of detecting and tracking aircraft based on their heat signature was proposed by Lindemann already during World War I [2]. Infrared hot spot trackers have proven to be well suited for detecting, locating and tracking airborne targets in the sky. The reason for this is that the apparent temperature of the sky is generally very low compared to the relatively hot aircraft parts. Depending on the weather conditions and the spectral band considered, the sky can appear as a homogeneous background for the aircraft. The scenario can thus be very simple.

Hot spot trackers also have uses beyond tracking aircraft. The ability to follow other point sources (or reflections) in uncluttered or slightly cluttered scenes is used in industrial alignment and positioning, particle accelerators [3] and satellite and star trackers [4].

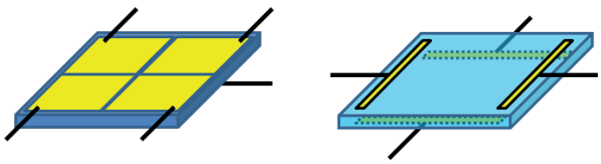

Figure 2.1. Quadrant detector (left) and lateral effect photodiode (right), two simple hot spot positioning sensors.

The most common industrial hot spot trackers are the quadrant detector and the lateral effect photodiode [5], shown in figure 2.1. The quadrant detector consists of 4 detectors. The detector array normally has a square or circular overall shape, split in 4

similar detectors. The quadrant detector is normally combined with focusing optics (or sometimes only a simple aperture). The system is actively steered in such a way that the focal spot (or beam) is moved in order to balance the signals from the four detectors. The lateral effect photodiode consists of a single photodiode with two anodes and two cathodes, in which the current distribution in each electrode pair gives a measure of the x- and y-coordinates of the spot image on the detector. Both systems commonly use modulation schemes to reduce noise, and are widely used for alignment and positioning purposes in the industry.

There are mainly two types of problems associated with such trackers when used to localize non-modulated hot spots. The first one is mainly due to bias and drift (and generally so-called 1/f-noise), as direct current (DC) offset will directly contribute to the system positioning signal. This can potentially make it impossible to track of low-signal targets, a common problem in the infrared spectral domain. The problem of handling bias was solved by introducing optical modulators, including reticles and choppers to form an optical alternating signal in a well-defined frequency band. The reticle, a transparent substrate with a non-transparent mask pattern, was first reported used as a modulator by Pfund [6] in 1929. The use of reticles for tracking was first conceived by the Germans during World War II (in the conical scan Kepka "Madrid" seeker planned for the Messerschmitt Enzian missile prototype developed by Wurster [7], and the spin scan "Karussell" sensor on the Wasserfall missile prototype developed by von Braun [8]), although the Germans stopped short of fielding such systems [2]. In the US, hot spot reticle trackers became popular in air target homing devices from the first successful laboratory demonstrator of the seeker in 1948 and the later successful launch of a complete missile system in 1953 [9, 10], picking up and refining the German concepts. Clark presented the first use of a reticle for tracking in the open literature [11]. Biberman made the first comprehensive overview of reticles used in electrooptics [12].

The second issue is that the background signal can be many orders of magnitude higher than that of the target. The shape of the reticle, and the relative movement of the projected scene relative to the reticle, followed by adapted filtering, can achieve the required level of filtering. Notably, the signal from a small point source can be extracted from a scene through the use of fine patterns that average out larger features, but create strong modulation with a relatively narrow bandwidth for a point source.

Two types of scan mechanisms have been popular in use with reticle trackers. The first one is the spin scan, in which the reticle is rotating respective to the projected scene, as seen in figure 2.2.

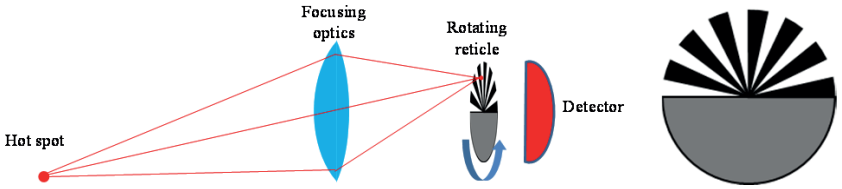


Figure 2.2. Spin scan system (left), and details of the "rising sun" reticle (right), featuring non-transparent (white) and transparent (black) sectors, and a semi-transparent (grey) "phase mask". The reticle is rotated. Decentred hot spots produce pulse trains. The phase of the pulse train determines the azimuth angle towards the hot spot.

One of the most popular versions of the spin scan reticle design is the "rising sun" reticle, invented by Biberman and Estey [13]. This reticle, shown in figure 2.2, consists of a semi-circle with alternating transparent and non-transparent sectors, the other semi-circle being covered by a homogeneous, semi-transparent (~50% transmission) pattern, known as the phase mask. A radially offset point source on an otherwise homogeneous background will then create an "error signal" in the form of a repeating pulse train, whereas a centred point source will produce a constant signal, in other words a zero error signal. Determining the phase of the pulse train envelope will determine the direction towards the point source compared to the optical axis. Reorienting the optical axis in the correct direction can then reduce the off-axis angle to an acceptable angle. The rising sun reticle has been termed an amplitude modulation (AM) tracker, as the phase is determined by the amplitude of the pulse train.

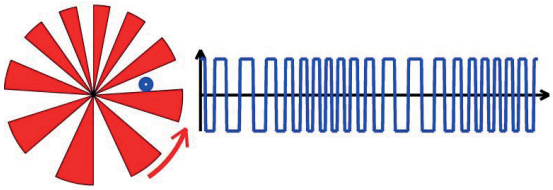

Figure 2.3. Frequency modulated (FM) spin scan reticle, and the resulting frequency modulated signal from a decentred hot spot (blue). The phase of the frequency modulation determines the azimuth angle towards the hot spot.

An alternative is to let the whole circle consist of only transparent and non-transparent sectors, and let the angle between the sector limits vary around the circle, as seen in figure 2.3. An off-axis source will then create a frequency modulated (FM) signal.

The phase information of the frequency modulation can be found by measuring the instantaneous signal frequency. This type of reticle is therefore called a frequency modulated reticle. Carpenter [14] determined that a low-bandwidth FM reticle would provide lower thresholds than the AM reticle, but that requirements for high frequency modulation (for example if the hot spot intensity is not stable, or if special background suppression is required), the AM reticle could offer superior performance if the carrier is sufficiently well separated from the amplitude modulation frequency (or spin frequency).

A disadvantage with the spin scan reticle system is that the error signal only indicates in which *direction* the hot spot is located relative to the optical axis, not the off-axis *angle*. This has been solved for the amplitude modulated spinning reticle by letting the number of transitions around the circle vary with the radius [15, 16], either in steps, or continuously as in the Lovell reticle [17]. These two versions are shown in figure 2.4.

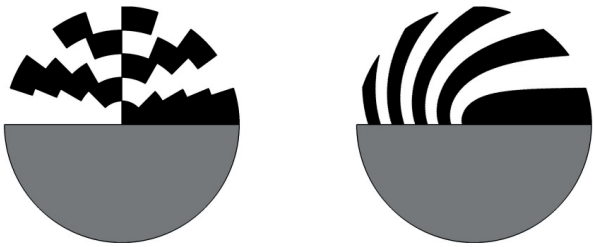

Figure 2.4. Spin scan reticle, with radially dependent frequency, either in discrete steps (left) or continuously variable (right). The latter is a version of the Lovell type reticle [17].

Another disadvantage with spin scan based reticle systems is that a centred hot spot will create a zero signal, and therefore be indistinguishable from not having a source present at all. This results in a low signal to noise ratio when the hot spot is close to, or aligned with, the optical axis. Thus noise or background clutter will make the tracker unstable.

This issue is not present in the conical scan reticle system seen in figure 1.1, where an image of the scene is projected onto a static reticle using nutating off-axis optics. In this system, the image of the scene is moved in a translational, circular movement. The conical scan reticle will normally have regularly distributed transparent and non-transparent sectors. All projected sources in the scene will then move in circles on the static reticle, with a characteristic scan circle radius. A centred hot spot will move around the centre of the reticle, creating a regular frequency pattern, possibly with higher harmonics if the projected hot spot size on the reticle is significantly smaller than the sector separation at

the scan circle radius. Off-axis sources will move in an eccentric scan circle, passing some sector edges closer to the reticle centre than others, hence creating a frequency modulated signal. Thus, different from the spin-scan system, a centred hot spot will create a non-zero signal, and the frequency modulation determines both the off-axis direction and angle simultaneously.

By default, a hot spot tracker assumes there is only one dominant source in the field of view. If several comparable objects are visible at the same time, the model fails, typically leading to either aiming towards some weighted middle of the objects, at the strongest source, or even at a completely different location. Ways to handle such scenarios will be discussed in the next section.

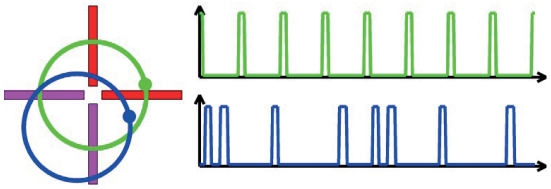

Figure 2.5. Crossbar (or crossed array) tracker signal from a centred (green circle and curve) and de-centred (blue circle and curve) hot spot. Position is determined by the pulse timing. An alternative "L-bar" sensor only uses two of the four detectors (indicated in red). Normally, the signals from the horizontal and vertical detectors are separated in two channels.

Hudson gives a comprehensive overview over the various aspects of reticles and their early use in trackers [18]. Hudson also covers a conical scan system that is not based on a reticle system: the crossbar or crossed array tracker, where four thin line detectors are forming a cross, as depicted in figure 2.5. The detectors are connected in pairs, in such a way that they consist of one "x" and one "y" channel. The crossbar tracker represents a class of sensors that use pulse modulation, in the sense that a hot spot produces a single pulse each time its projected image crosses one of the detectors. When the optics scans the image across one of the "x" bars, the x-coordinate can be read out from the timing of the pulse, and likewise, the y-coordinate is given by the timing of the pulse from the y-channel detectors. The crossbar can use the time difference between the signal from the two detectors of the same channel to avoid using a spin reference timing, but in principle, no new information is extracted from the second pulse, and an equivalent detector system could be formed by using only two detectors mounted orthogonally, forming an L-shape.

The Encyclopedia of Optical Engineering devotes two chapters to spin scan reticle systems and conical scan (nutating) systems, also including the crossbar tracker and the semi-imaging rosette scan tracker [19]. The latter will be treated in the next section.

# 2.2 Multispot Tracking, Semi-Imaging and Imaging Technology

## 2.2.1 Traditional Imaging Technology

Classical imaging is normally done with a single element detector, a linear or a 2D detector array, as seen in figure 2.6. The scan mechanism of a single detector normally consists of 2 rotating mirrors, one scanning fast along a line that is repeated, and a second scanning more slowly to shift the first linear scan sideways, thus creating 2D image. If a linear array is used, a mirror rotates around an axis parallel to the linear array. A 2D detector array normally does not need a scanning mechanism, and is therefore sometimes called a staring array. Some 2D arrays also have a step scan mechanism to increase the field of view sequentially, and are then often called a step-stare system.

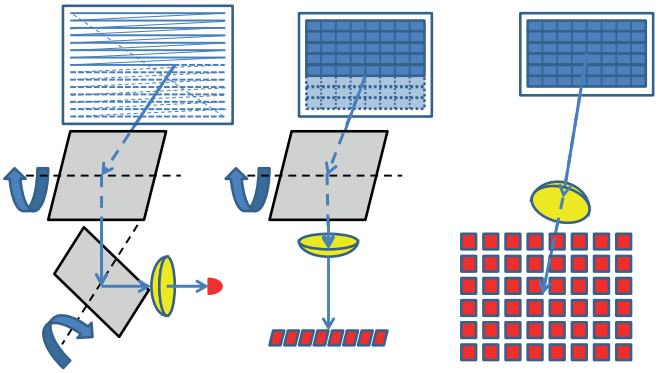

Figure 2.6. Classical imaging techniques: Raster scan with a single pixel detector (left), linear scan with a linear array (middle) and staring focal plane array (right). Focusing optics are depicted in yellow, detectors in red.

Historically, electronic imagers in the visible spectral range began with the iconoscope, consisting of a thin charge collecting granule layer (necessary for localizing the charges) that was read out electronically raster scanned cathode ray inside a vacuum tube [20, 21]. Developed in the decades of 1920-1940, the system was later replaced by similar cathode ray tube based devices, including the orthicon and the vidicon, before being replaced by the CCD sensor in the 1980's, the latter gradually seeing increased competition from the

CMOS sensor [22]. The CCD and CMOS sensors are offspring from the hugely successful and rapid integrated digital circuit development. The achievable performance is quite impressive, for example extremely low readout noise levels, down to below one photoelectron per pixel per frame.

Infrared imagers did not follow the same development path, primarily for two reasons. In part, it was difficult to find photocathodes with useful work functions to give sensitivity in the infrared range, but secondly, thermal noise levels in infrared cathode ray readout based systems would be several orders of magnitude higher than acceptable. Therefore, early thermal imaging would typically take place using single detectors with dual mirror raster scan systems, or spinning prism systems.

Due to the technological gap between Si and other semiconductor material development, it took a long time before detector arrays in other materials became available, mainly due to the small wafer sizes available with good material quality, and the possibility to make low noise electronics. The possibility for large 2-dimensional (2D) imaging devices at lower photon energy levels than the Si band gap levels have become possible due to the combination of low noise silicon readout integrated circuits (ROIC) combined with indium bump technology, enabling large scale 2D connection between Si ROICs and large scale detector arrays in various arrays, such as indium gallium arsenide (InGaAs), mercury cadmium telluride (MCT) and indium antimonide (InSb). A recent example is the 2048×2048 pixel MCT array of the James Webb telescope, featuring a ROIC with 6 $e^-$ (rms) readout noise for a more than 1000 s exposure time [23]. MCT has proven to be of high value for infrared imaging, partly due to the noiseless amplification in avalanche photodiode operation [24, 25], but most importantly due to the tuneability of the band gap.

Focal plane array (FPA) sensors now come in several sizes, with multi-megapixel devices being commonplace in the visible spectral range in cell phones, toys and other household items. In the scientific domain, the imagers in the visible domain now features such high quantum efficiency levels, together with low noise figures, that they are on the verge of being able to replace night vision systems in some applications. They can also be "stitched" together to form diffraction limited cameras with 1-100 gigapixels, or beyond 1 petapixel/s [26]. Infrared cameras are also now accessible in multi-megapixel formats (open literature currently presents 4k × 4k infrared imagers in different bands [27]), with background limited performance noise levels, and some cameras features frame rates that are in the multiple kHz range. Uncooled FPA sensors have noise performances enabling

cameras equipped with them useful ranges up to several kilometres. New sensors are available at a high volume sensor price down below USD 50 [28]. These sensors have sensitivities below 50 mK, making them attractive for cell phones and other consumer electronics. The FPA sensors now span the ultraviolet, visible, and various spectral bands in the infrared domain. Lately, FPA sensors have also become available in the THz domain [29], but they are either relatively slow, or their cost is still significant.

Raster scan single pixel imaging using various scanning devices has now been limited to niche applications, mainly in devices making use of active scanning, such as confocal microscopy [30, 31, 32] and 3D laser radar imaging, where long range measurements are limited by the laser output.

### 2.2.2 Multispot Tracking, Semi-Imaging or Less Conventional Imaging Technologies

The hot spot reticle tracker is characterized by high sensitivity, low cost, simplicity in implementation, high frame rates and low latency. For this reason, it has remained popular in air target homing devices since the first systems were fielded after World War II. For more complex scenarios than a single point target, however, the hot spot tracker is unreliable. Observed behaviour includes choosing some form of averaging of the point sources in the scene, or tracking the dominant source. This called for approaches to handle multiple simultaneous point sources. Systems based on the reticle scanner used for imaging have been proposed [18]. In [33], Sanders *et al.* present a system using an extra scanning mirror to enable imaging. Another method proposed by Bae includes an additional slowly rotating reticle [34]. Solutions using a combination of a reticle with various detector arrays, including dual semi-circular detector pairs, quadrant detectors, annular arrays and more exotic versions where the circle is split both radially and into sectors have also been demonstrated [35, 36, 37]. The motivation is that the likelihood of several point sources being covered by the same detector is relatively small. Conceptually, the system is considered as multiple regular hot spot trackers. There is obviously still the risk that two point sources occasionally interfere. This case therefore needs to be solved by the system. A real world tracking device typically drifts somewhat, thus interference occurs occasionally for a shorter or longer duration of time.

A different and novel approach presented in several publications by Kopriva *et al*. involves modifying a conical scan reticle system by replacing the single pixel detector by a beam splitter and two detectors on the beam splitter output. The beam splitter/detector

combination should be spectral by nature, and the sources must also be spectrally different in the respective channels, so that the two detector signals are different by more than a scaling factor. By using the blind separation of sources (BSS) technique developed by Jutten and Herault [38], they demonstrated both theoretically and experimentally that it is feasible to separate multiple simultaneous point sources [39, 40, 41].

The crossbar tracker introduced in chapter 2.1 [18, 19] also has a certain multisource tracking capability. By using thin detectors, the probability of two hot spots being aligned is reduced, decreasing interference. However, assigning correct x- and y-pulses to each other might pose a challenge, especially as the number of hot spots increases.

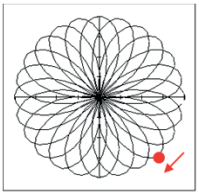

Figure 2.7. Rosette scan pattern.

In the rosette scan tracker a single point detector is scanned in a 2D rosette pattern, as seen in figure 2.7. The system is in some applications superior for tracking compared to a 2D raster scan in that the most likely location of the target (i.e. the centre of the field of view) is scanned more often than the peripheral parts of the field of view.

A linear array can be scanned, either directly or using a scan mirror, to create a 2D image. One advantage is that the scan can cross one or several controlled light sources outside the regular field of view, such as blackbodies, to compensate for sensor drift and non-uniformity. Other scan possibilities represent the broom scan, where the platform (typically a satellite or aircraft) containing the sensor moves over an area, or object self-scan, where the movement of the inspected object itself provides the scanning [42], for example a car driving in front of a linear array. Self-scanning can have problems with deformable objects. Pedestrians walking past such a sensor will give images where the legs and potentially arms are not being properly reproduced.

In 2011, a series of publications from the group of Randy A. Bartels at the University of Colorado has presented an imaging technique termed spatial frequency modulation for imaging, or SPIFI. Here, they use a rotating Lovell reticle with a radius dependent frequency pattern to create 2D illumination modulation that, after illuminating the target, can subsequently be detected by a single element detector [43]. The experimental setup has

been used in both absorption and fluorescence imaging [44]. A 2013 publication from the group has also presented 2D imaging through the use of a line scan camera combined with a Lovell type reticle modulated light source [45].

## 2.3 Tomography

Tomography, from the Greek terms *tomos,* meaning slice, and *grapho* meaning to write, represents imaging through sections or sectioning. Although it is typically referred to in the context of imaging using penetrating radiation, including electro-optical (especially X-ray), various particle (and anti-particle) radiation and acoustics, it can also be used with line-based or knife-edge based detection of non-penetrating radiation.

Johann Radon's publication in 1917 [46], described in mathematical terms what was to become known as the Radon transform. In medicine, prior to 1974, the term tomography was used interchangeably with planography [47, 48]. Planography is an X-ray imaging technique developed in 1920 by Bocage in which the X-ray (point) source and plates of photographic film on the other side of the subject imaged move in opposite directions. The technique is depicted in figure 2.8. The movement remains parallel to the photographic film plane at all times. In this way, one plane in the body remains static with respect to the image created, and therefore maintains focus, whereas out-of-focus objects will be blurred by the movement.

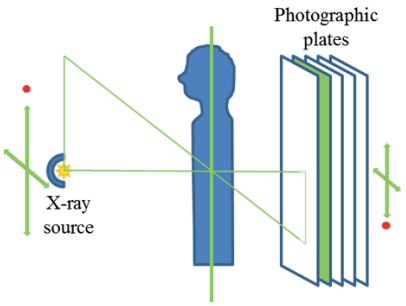


Figure 2.8. Principle of planography. The source and the photographic plates are moved in opposite directions during exposure, leaving only one plane per photographic plate in "focus".

The aforementioned Radon transform was rediscovered by several scientists and engineers in different fields: Cramer and Wold [49] in statistical problems in 1936, Cormack [50, 51] and independently Hounsfield [52] in computer tomography (CT) scanning, and Bracewell and Riddle [53] in radio astronomy images using long thin radio antennas, which had a high resolution in one direction only. Rowley [54], and Berry and

Gibbs [55] also produced theoretical publications in 1969 and 1970 describing the process of finding internal structures using a series of X-ray projections. Most of the work was apparently undertaken without previous knowledge of the Radon publication (which was published in German).

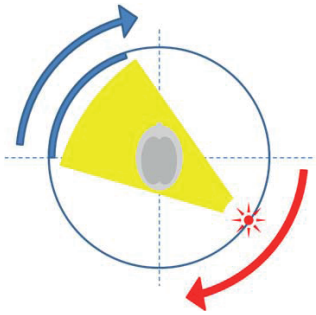

Figure 2.9. Principle of CT scanner. An X-ray source (red) emits X-rays (yellow) penetrating the subject (grey). Transmitted radiation is detected at the detector array (blue). Scans at different angles are measured by rotating the source and detectors in angular increments.

The big boost for tomography came with the invention of the CT scanner by Hounsfield, for which he earned the 1979 Nobel Prize together with Cormack. Of the two Hounsfield is the most famous. He is credited with bringing the device into actual medical applications (with the first clinical image taken in 1972), although other scientists undertook both theoretical and experimental work. The principle of the CT scanner is depicted in figure 2.9.

2D X-ray tomographic images now typically recreate high resolution (for example 512×512 pixel) images [56]. In modern imaging, focus has been on producing 3D images, using helical scan. These imagers are characterized by low noise and extremely fast detector arrays. Along with inductive electrical rotating coupling of both signals and power, and high performance signal processing, this enables fast imaging, low radiation doses and accurate imaging of soft tissue [57, 58]. Figure 2.10 shows 2D and 3D reconstructions from a state-of-the-art CT imager.

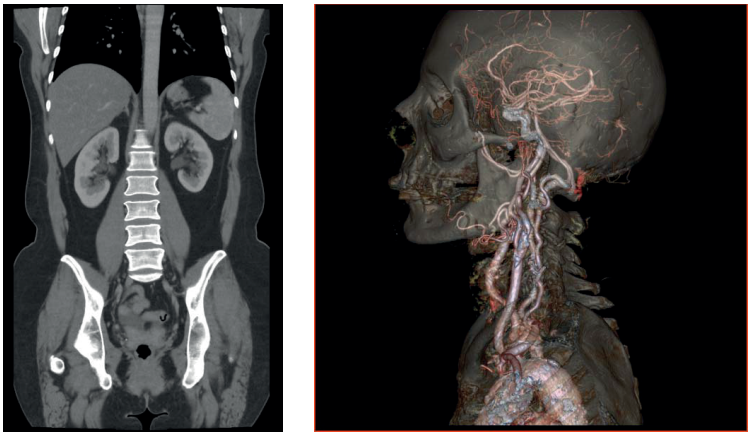

Figure 2.10. State-of-the-art reconstructions from X-ray tomographic imagers. “Revolution CT” image, courtesy of GE Healthcare.

Extreme 3D resolution (16 nm) has been achieved by Holler *et al*. [59], using the PILATUS 2M X-ray detector with a 1475×1679 pixel array [60] in a ptychographic tomography setup, with 720 angular scans (a ptychographic setup is peculiar in that the source can be moved sideways in two dimensions, in addition to the regular rotation of the specimen, to increase resolution). The illumination source had a 2 Å wavelength.

The medical market has been a significant driver for the tomography development, with over 20000 X-ray CT scanners installed in the USA only by 2009 [61], representing a 3.6 billion USD by the end of 2009. In addition to the regular X-ray CT scanners, there are also scanners based on other tomography techniques, such as the positron-electron tomography (PET) scanner, optical coherence scanners and tomographic scanners using ultrasound. The latter two extend to propagation along nonlinear paths and propagation through strongly scattering media.

Another important set of applications are the synthetic aperture radar (SAR) and synthetic aperture sonar (SAS) [62, 63]. Here, a collection of radar or sonar images, each with relatively poor angular resolution, but with good temporal (equivalent to range) resolution are recorded while the instrument is moved around the region of interest. A reconstruction using the Radon transform is then made to increase the resolution of a final image based on multiple lower resolution images. The reconstructions are characterized by using a region of the Fourier space offset from the origin.

Figure 2.11 depicts a SAR image taken in the Lillestrøm, Norway, area, and includes buildings and other man-made structures, and natural features like grass, trees and water.

Figure 2.11. SAR image taken with a PicoSAR made by Selex Galileo Ltd. The 30 cm resolution image, taken from a helicopter, features both urban and more rural areas, as well as water. Image courtesy of Nina Ødegaard, Norwegian Defence Research Establishment.

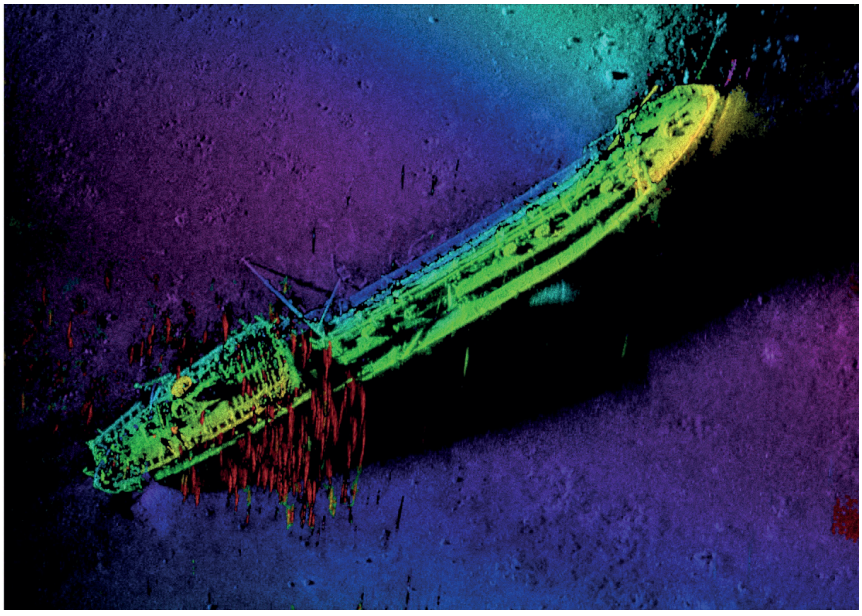

Figure 2.12. Interferometric synthetic aperture sonar (SAS) image of an oil tanker that was sunk during WW II. The size of the wreck is 68 × 9 m. The range to the centre of the image is 95 m, and the image size is 60 x 78 m. The theoretical resolution in the image is around 3 x 3 cm, and the resolution in the bathymetry is 18 x 18 cm. The sonar image is a fusion of interferometric SAS image, bathymetry, and coherence. The red lines on top of the bridge of the ship in the lower left corner of the image are a school of fish. Data collected using a Kongsberg Maritime HISAS 1030 interferometric SAS on a HUGIN 1000 autonomous underwater vehicle. Image courtesy of Norwegian Defence Research Establishment and Kongsberg Maritime.

Figure 2.12 depicts a wideband interferometric SAS image. The SAS image reconstruction is performed with the back projection algorithm in combination with data driven navigation correction [62]. The seabed depth is estimated using the complex cross correlation technique for wideband interferometry [64].

Literature in the field of tomography and the Radon transform [65-70] and cover several types of tomography. In addition, more complex types of scan such as helical scan and scans along nonlinear paths, either due to strongly inhomogeneous media, or strongly scattering turbid media are covered.

Knife edge or narrow slit scans followed by tomographic reconstruction have been used to characterize light sources [71] and, supported by the work presented here, point spread functions of (multispectral) cameras [72]. An example of the latter is depicted in figure 2.13.

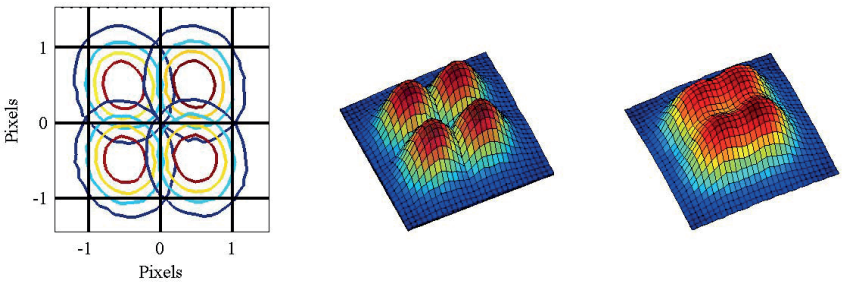


Figure 2.13. Tomographic reconstructions of the point spread functions of camera pixels. Narrow slit recordings were made with 48 angular directions. Contour lines at 20, 40, 60 and 80% for four neighboring pixels (left), 3D plots of the same pixels (middle), and a summation of the point spread functions (right). From Torkildsen *et al*. [72].

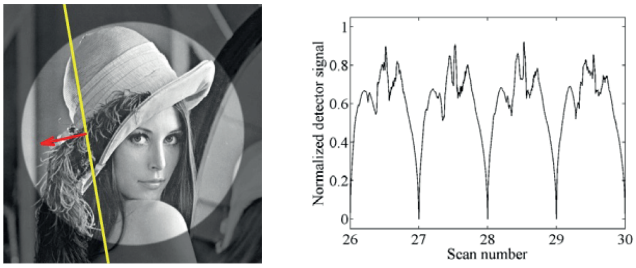


Figure 2.14. Parallel line scan. Left: line detector (yellow) is scanned (red arrow) across the image plane while its orientation remains constant relative to the image. The orientation is then shifted, and a new line scan is made. A circular aperture is used to limit the field of view. Right: Sequence of scans at 4 different angular orientations. Coarse features keeps their shape relatively well from one scan to the next, but fine details are changed more rapidly.

In parallel scan tomography, the scene is typically scanned along regularly distributed angular scan lines using line detectors, as seen in figure 2.14. Each line scan can then be Fourier transformed. Such a scan line represents a mapping of the image in Fourier space along a line going through the origin. If an infinity of angular scans is measured, it is theoretically possible to fill up Fourier space, enabling a complete knowledge of the image. To perfectly reconstruct the image, an inverse 2D Fourier transform could then be performed.

The fact that a finite number of angular scans and a finite number of samples per angular scan are measured leads to the following limitations on the reconstruction:

- Only images with limited frequency content can be (relatively) faithfully represented, in line with Nyquist theory. Aliasing can be avoided if the physical measurement system features a frequency cut-off.
- The Fourier space mapping is done on a discrete polar grid. This poses some issues for the (discrete) inverse transform, which would normally be done on a Cartesian (square) grid.
    - The grid has a limited number of samples across, which implies an (incorrect) assumption of continuous boundaries when using the Fast Fourier Transform (FFT). This effect is reduced by zero-padding the measurements along each angular scan prior to the FFT. The problem of continuous boundaries and the zero-padding is illustrated in figure 2.15.
    - The polar grid points do not overlap the Cartesian grid points. Notably, the polar grid point density decreases radially, whereas the Cartesian grid point density remains constant. If a transition is done using interpolation, it is found that the accumulated interpolation can normally lead to significant errors in regular (“non-Fourier”) space.

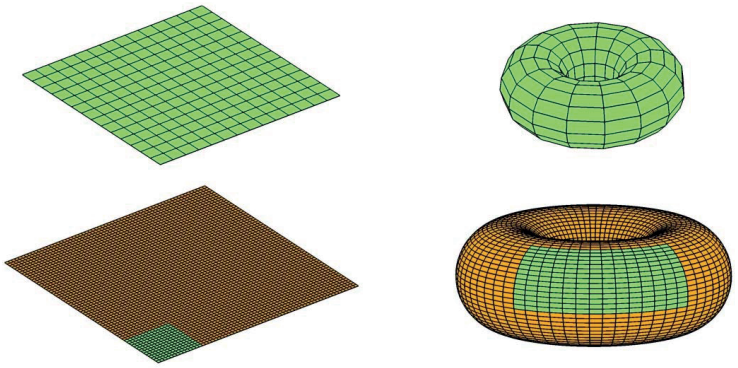

Figure 2.15. Continuous boundaries effect in the FFT transform. If a matrix (top left) is operated on using the FFT transform, there is an assumption of continuous boundaries, as if the matrix "sheet" was folded into a torus (top right). Frequency filtering will typically be affected by (unphysical) spillover effects. By zero-padding the original (green) matrix, the resulting (green + brown) matrix (bottom left) will be less affected by spillover effects, as the distance between adjacent edges in the corresponding torus has been increased in all directions (bottom right).

An improved method was found in 1971 by Ramachandran and Lakshminarayanan [73], in which they never transitioned from the polar to the Cartesian coordinate system in Fourier space, but weighted the Fourier components by multiplying by the absolute value of the frequency, to compensate for the radial density of the samples in the polar grid, as shown in figure 2.16. The filtered samples were then back projected to regular space, and

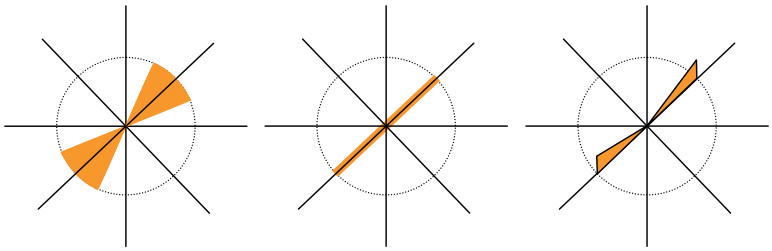

Figure 2.16. Filtered back projection approximation. The sector in the Fourier domain shown (left) is represented by a line, corresponding to the transformed samples of the line scan from one angular orientation. To compensate for the decreased density away from the origin, the components are weighted by a factor proportional to the distance from the Fourier plane origin (right).

these filtered back projections were then summed up. In practice, the Fourier transform – filtering – inverse Fourier transform was replaced by an equivalent convolution. This process was found to be superior to the previous method, both in terms of accuracy, computational load and storage requirements. The *filtered back projection* has become the normal procedure for parallel scan imaging. In a normal system, the samples in each line

scan are oversampled, typically using cubic interpolation, and then zero-padded significantly. The back projection is done using linear interpolation onto a rectangular grid. Some artefacts called “ghosts” can be encountered, especially if Nyquist criteria are not fulfilled [67]. These artefacts limit dynamic range and subsequent feature extraction.

Multiple methods reduce the previously mentioned artefacts. A popular group of techniques goes under the term algebraic reconstruction techniques [74]. These are iterative techniques where the obtained image is rescanned. Ideally the signal obtained should be identical to the measured signal. The difference, often termed the error signal is processed, and a correction based on the difference is applied iteratively until the rescanned signal is close enough to the original scanned signal.

For some signals, certain constraints can be applied. An example is the many applications where the signal cannot be negative. Computation of the signal can be constrained to improve performance at each iteration.

It should be noted that the explosive development in computing power since Hounsfield’s first practical scanner has enabled vast improvements of the potential for reconstruction enhancements.

Recently, the optical realization of the radon transform has been achieved without mechanically moving parts, instead using a combination of two lenses, an amplitude slide (a mask with a radially varying transmission), and a spatial light modulator (SLM) [75]. As the whole transform was achieved instantly, the SLM could be replaced by a fixed phase mask. It would, however, only be valid with spectrally narrowband scene illumination.

## 2.4 Multi- and hyperspectral imaging

The possibility to superimpose images of the same scene made in different spectral bands and/or polarizations simplifies or enables detection of characteristic object features in many applications. This is useful to detect objects in the scene even without enough spatial information (or enough processing power). Applications include detection of high temperature objects, the presence or absence of characteristic chemical substances or a combination of substances that give evidence of specific processes or activities. In a remote sensing environment, this can allow monitoring of volcanic activities, hydrocarbon reservoir indicators, industrial toxic spills, or illicit drug manufacture. Figure 2.17 depicts some examples of hyperspectral imaging results.

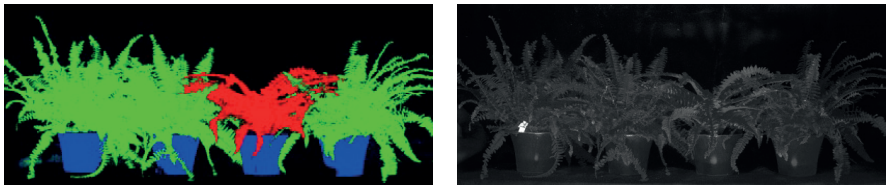

Figure 2.17. Multi- or hyperspectral imaging can be used to discern similar objects (left, one fake plant present), or to find small objects with unusual or specific signatures (right, LEGO man). Images courtesy of Torbjørn Skauli, Norwegian Defence Research Establishment.

There are many ways to design multi- or hyperspectral imaging devices. The most well-known include:

- One or multiple cascaded beam splitters to split the beam into spectral channels, with one 2D FPA on each spectral channel. This implementation has high photon throughput and allows temporal synchronization of the different spectral channels. A dichroic RGB prism (i. e., a Philips prism) is commonly used in high end RGB ("3CCD") video cameras. The more compact trichroic X cube beamsplitter has been used in projectors.
- A single FPA with a mosaicking filter, for example the RGBG Bayer filter. This system enables temporal synchronization, but not geometric co-registration.
- A similar solution consists of spatial line or band filters that cover linear segments of a 2D FPA. This system scans the scene, and typically uses spatial features and/or data from an inertial measurement unit to co-register different spectral bands, but without temporal synchronization [76].
- An imager with a rotating filter wheel. The frame rate is normally synchronized to the filter wheel rotational speed to take one image per filter position. The imager consists of focusing optics and either a 2D FPA, a linear array with a linear scan, or a single pixel 2D raster scan. The spectral channels are then recorded sequentially.
- Linear scan of a slit, followed by dispersing optics and one or several 2D FPAs [77].
- A 2D raster scan of an aperture in front of a dispersing prism and a linear array. Alternatively, the aperture and dispersing optics could be replaced by a fibre coupled spectrometer.
- 2D array of fibre coupled spectrometers, in fact just a rearrangement of the linear array version.

The latter three setups have the potential to enable perfect spatial co-registration of different spectral bands. Some newer and more advanced systems include:

- The hyperspectral chromotomosyntetic imager, presented theoretically by Levin and Vishnyakov [78], and developed into functioning devices by Mooney [79] and Descour and Dereniak [80] in the 1990's, consists of a field stop unit, followed by a rotating dispersive element, and finally focusing optics that projects the image onto a 2D FPA. The resulting images are superpositions of the spectral components of the scene that have a translational circular movement, the radius of the scanning circle depending on the wavelength.
- Imaging Michelson Fourier transform interferometer [81].

Sanders and Wellfare [88] presented a multispectral version of the reticle based imager by Sanders *et al*. [33] mentioned earlier.

A very good and comprehensive text book on hyperspectral imaging has recently been published by Eismann [83].

The efficiency of collecting signals in each pixel in the different spectral channels is essential in multi- and hyperspectral imaging. This puts requirements on scene coverage and efficient collection in all spectral channels. Filter wheels and band pass filters generally lose all information outside the filter band pass, and are therefore relatively inefficient. Beam splitters and dispersive optics are more efficient, provided the spectral content is collected by a corresponding detector array. In a similar way, the higher the number of detector pixels exposed to the scene simultaneously the better, as is also the case in monochrome imaging.

Another aspect is the temporal and geometrical co-registration/overlap of the spectral channels from a given direction onto matching detector elements. This is especially critical for detection of sub-pixel targets in the image. Here, it is feasible to perform the search of a point target with a known spectrum on a known background could be done in low-dimensional (and small volume) multi spectral vector hyperspace. A bad co-registration, on the other hand, means that the target could be anywhere in a very significant hyperspace volume. This could make the search for the target very long and error-prone [84, 85].

# Chapter 3 – Research Summary

This chapter presents motivation, results and summaries of each of the publications included in the thesis, and put the results into context of the overall work. An overview of the research is given in section 3.1, together with a presentation of how the publications relates to the research objectives presented in chapter 1.

## 3.1 Overview

This dissertation is a collection of publications. This section presents the publications and the relationship between them, as depicted in figure 3.1. The recurring theme is the development of the tomographic scanning imager, including refinement of the theoretical model, verification through simulation, and validation through experimental demonstrators. The first two publications focus on what is feasible with existing knife-edge reticle scanners. The third publication introduces the thin slit reticle configuration, as well as the conical scan thin slit reticle imager. The three first publications thus represent a stepwise evolution of the concept of the conical scan tracker as an imager from inception to the full mathematical theory of the TOSCA imager.

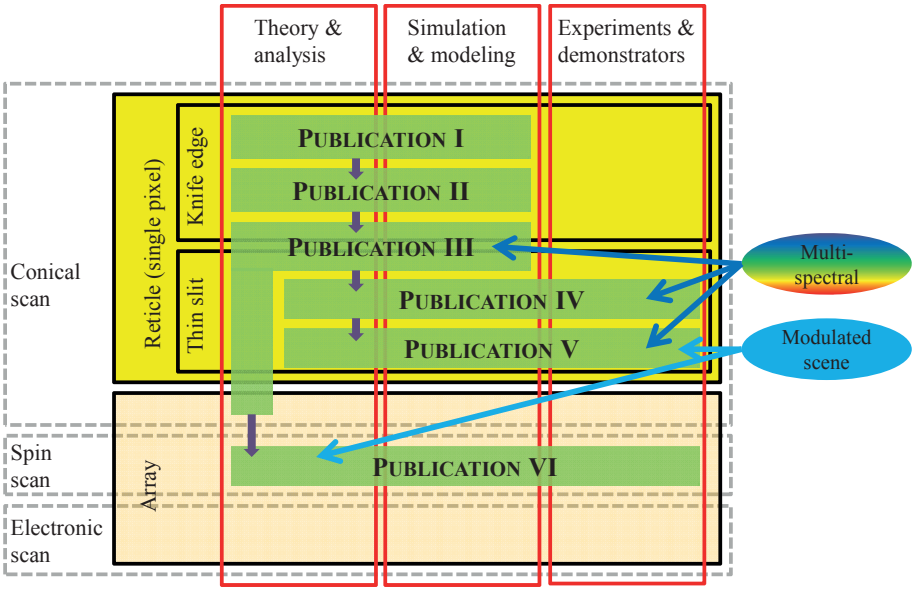


Figure 3.1. Coverage of, and relation between the publications included in this thesis.

Publication IV and V are experimental publications, where the theory is applied to demonstrators of the thin slit reticle based TOSCA imager. This validates the previously developed theory and simulations, and shows that the imagers can be implemented using realistic components, and produce useful results.

In publication VI, a spin scan mechanism is demonstrated instead of the previously used conical scan. Both conical scan and spin scan reticle hot spot trackers are widely deployed in the same applications. In this work, both concepts use tomographic reconstruction of thin line slits/detectors.

The spin scan array-based imager concept in publication VI arose as an effort to improve the conical scan array-based imager concept. The array concept may be extendable to an electronic scan TOSCA imager concept, introduced as suggestion for future research in section 4.2.5.

## 3.2 Publication I

The first publication launched this research, through the realization that a specific type of hot spot tracker, the conical scan (or con-scan) reticle tracker does, in fact, possess imaging properties, and that it is feasible to extract these properties through the use of tomographic reconstruction techniques.

Because the target image retains its orientation while it has a circular movement across transparent and non-transparent sectors, the scan can be considered a succession of knife-edge scans, as seen in figure 3.2. The time derivative of the knife-edge scan corresponds to a line scan, plus a term describing temporal variation in the visible part of the scene. Assuming the latter to be negligible, tomographic reconstruction techniques can be used to reproduce an image of the scene. A circular aperture moving with the scene can be used to avoid aliasing arising from several simultaneous knife edge scans.

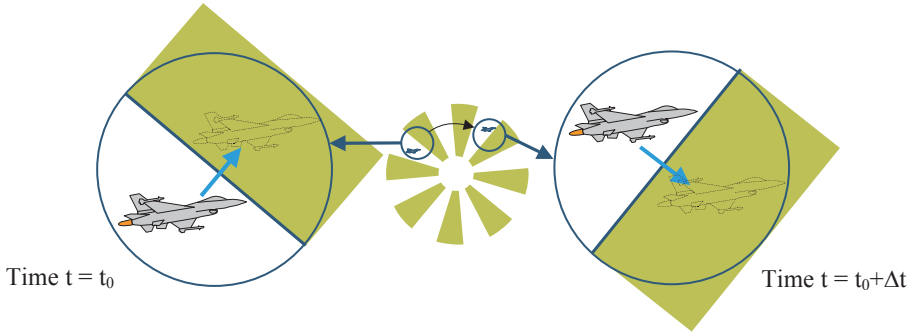


Figure 3.2. Detail of conical scan reticle scanner. The scan can be considered as a succession of knife edge scans at regularly distributed angular orientations.

A first simulation model was built up to simulate a basic TOSCA seeker without a moving aperture. The calculations used the spatial convolution of the reticle and the scene to create a 1-dimensional signal, and the reproduction was made as the dot product of the spatial reticle gradient (vector field, in the scene co-ordinate system) and the scan direction, multiplied by the detector signal as a function of time. The result is a spatially low-pass filtered image.

The implemented model is able to distinguish and locate closely separated objects in a relatively simple scene. It is, however, unable to reproduce shape, and furthermore shows significant aliasing for scenes that extends upon more than one knife edge.

## 3.3 Publication II

The second publication demonstrates the effect of modifying the TOSCA seeker with the moving aperture and multiplying the frequency components with the absolute value of the frequencies, enabling true imaging properties to the system. This is also demonstrated through simulations, and shows the first simulated images of such a system, proving that the TOSCA imager should work, also on very complex scenarios.

Two classes of reticle shapes have been investigated for optimization, one traditional regular sector version with a common sector apex, and a novel version with separate, eccentric apices. The latter is demonstrated to almost double the angular resolution while maintaining the same number of knife edges and the same field of view by reducing redundancy due to parallel knife edges.

Estimations of processing complexity and the potential for parallelization are made. For a well-balanced image, the processing requirements per frame scale as $O(n^3)$, where $n$ is the pixel size of the reconstructed image. The computations are shown to be highly suited for parallel processing. It is also demonstrated that much of the processing can be performed once and stored in look-up tables. This is efficient both in terms of computing resources and latency reduction.

## 3.4 Publication III

The third publication presents the mathematical foundation of the TOSCA imager, only invoked in the conference publications. The narrow slit reticle is introduced as a significant improvement, compared to the knife edge reticle configuration. The narrow slits eliminate

a significant portion of background noise and increase the dynamic range of the sensor significantly.

An array-based con-scan configuration is also presented in this publication, featuring multiple novel improvements to the state of the art. The use of independent detector channels enables multiple line detectors to be in the field of view simultaneously. This allows for a significant reduction of scanner dimensions, reduces bandwidth requirements, and improves photon harvesting efficiency. It also simplifies the optics and enables the use of shorter focal lengths and higher *f/#* in the focussing optics, with the potential of significant signal to noise enhancements compared to a single pixel detector system.

The mathematical description of the system has enabled accurate modelling and simulation, including modelling of noise. The publication also presents a comparison of several types of sensors.

It is demonstrated that the reticle based system is suitable for multispectral operation. This is due to an intrinsic co-registration of different spectral channels, if the signal is spectrally separated after the reticle, meaning an exact geometric overlap between spectral bands can occur, combined with an exact concurrent sampling. This is important in multispectral signature recognition, as it facilitates target detection and reduces false alarms.

## 3.5 Publication IV

In this publication an experimental demonstration of the TOSCA concept is presented for the first time. The experimental demonstrator presented operates in the visible spectral range. Both the principle and a detailed description of the main components used to create the imager are presented. The scanning mechanism of the TOSCA demonstrator consists of a single rotating optical unit, combined with a static reticle.

Imaging results are found to be in good agreement with theoretical predictions based on information from the component characteristics from the manufacturers and detailed modelling and simulation. An extension to multispectral imaging is presented and demonstrated with a two band imager. Good co-registration of bands is observed, as expected.

This publication includes detailed simulations of the effects of imperfections, with particular emphasis on misalignment, temporal jitter and offset. The analysis stresses the importance of precise control of the angular scan timing. This prompted the development of a new signal tracking/resampling technique to enable high resolution imaging. This

technique enables the use inexpensive mechanics, as large variations in the motor steering can be tolerated.

## 3.6 Publication V

This second experimental publication presents more research based on the first demonstrator in the visible domain, as well as a new imager operating in the short wave infrared spectral region (1.8-2.5 μm). This uncooled infrared imager is based on a simplified version of the first imager with lower resolution and frame rate.

Many of the parts in this simplified imager are 3D-printed. This demonstrated that it is possible to create an inexpensive infrared imager using readily available components, in addition to components produced with a consumer grade 3D-printer. One of the approaches to reduce imaging cost is the use of BK-7, a low cost glass normally used in optics in the visible domain. Here, however, it has been used for short wave infrared imaging, as it has acceptable transmission up to around 2.5 μm. The effects of spectral aberrations are compensated for by designing the optical setup with large spot size tolerance. Another approach used to cut cost is by using low cost reflective optics. Using this approach, it was demonstrated that it is feasible to implement an infrared imaging camera for less than 400 USD (not including the PC). Furthermore, the demonstrator was developed in less than one week, making this approach of interest for educational purposes.

Low cost allows implementation of the new imager in new applications. An example is in operation in hazardous environment where the lifetime expectancy is short, or on disposable platforms. Such environments include areas of both volcanic activities and radiological hazard.

The publication demonstrates the compensation of the scene illumination when the modulation frequency is higher than the frame rate. By measuring the total scene intensity at each angular scan, an overall intensity profile can be used to scale the signal to compensate for the modulation encountered. The effect of this modulation and the compensation is shown in a pair of images.

## 3.7 Publication VI

The final publication is a report on theoretical and experimental work with a new TOSCA-type imager, this time using a spin scan mechanism rather than the con-scan used in the previous publications. The sensor is a densely packed linear array so that, in principle, it is

possible to have a 100% fill factor of the scene, enabling the detection (and at least a one-dimensional location) of transient signals much shorter than the frame rate. The sensor array can then be produced as a monolithic unit that is significantly more compact and precise. This allows reduced manufacturing cost, lower bandwidth requirements and less noise compared to detectors used or proposed in earlier publications.

Several scan mechanisms are proposed. The mechanism implemented in the demonstrator presented in this publication consists of a simple rotating unit with 3 plane mirrors in front of the focusing optics. A novel and very compact alternative solution was also proposed. This optical system has a toroidal primary mirror facing a cylindrical or toroidal secondary mirror mounted in a rotating unit. A third solution is even simpler: if the camera is mounted in a rotating vessel or projectile it may be self-scanning, simplifying the optics and scan mechanism down to a simple lens in front of the linear array.

The concept is compared analytically to other imaging concepts in terms of noise, and the sensitivity to imperfections in terms of alignment, non-uniformity and scan-related errors is investigated. The system is found to have less noise than alternative conical scan TOSCA systems, by a factor of 4 or more. It is better than the traditional linear array detector with one-dimensional scanning, but not as good as the 2D focal plane array. Non-uniformity was shown to be a potential issue.

An uncooled mid-wave infrared spin scan TOSCA demonstrator is presented. A 2D array was used in a software binning mode to emulate a linear sensor since arrays of long detectors are not readily available. This choice of detector reduced the frame rate by approximately 2 orders of magnitude for the same noise level, but enabled diagnostic and illustrative imaging of the field of view as seen with the 2D array.

A technique to double the resolution was proposed. The approach shows promise and warrants further research. However, because of non-uniformities of the specific detector array used, the results are so far inconclusive.

Finally, the imaging properties as a function of angular resolution were investigated. The results show that basic imaging properties become available with a number of angular positions in the order of 10, even in the presence of significant noise.

# Chapter 4 – Conclusions and Future Work

This chapter presents the conclusions and contributions of the research undertaken. Concepts and tasks deemed worthy of additional investigation are presented in section 4.2.

## 4.1 Conclusions

This work has bridged the gap between the conical scan hot spot tracker and imagers, and presented the discovery of a new class of imagers that are based on narrow slit reticles and line detectors using tomographic image reconstruction techniques. Thorough theoretical analysis is found to be in good agreement with simulations and experimental results, demonstrating an understanding of the inner workings of the system. Imaging has been demonstrated in the visible, short wave infrared and mid wave infrared spectral domain, showing the versatility of the concept.

The noise levels are found to be significantly higher than those of staring focal plane arrays, as would be expected, but lower than corresponding broom scan or raster scan systems. Due to the signal superposition from multiple sources combined with artefacts in the reconstruction, dynamic range is reduced. In addition, scenes with moving objects may cause interference.

However, this work demonstrated the potential for low cost and easy manufacturing. The demonstrated systems handle rapid illumination transients and modulation frequencies that are significantly faster than the frame rate. Detection of this modulation or transient can be of importance in itself, but characterisation and compensation of the process can also be of significant value. Arguments have been forwarded that not only general illumination, but also single or multiple sources could be detected, characterized and compensated for, but this has not been demonstrated, and the investigation of this claim remains inconclusive so far. Such a capacity could clearly be useful in several applications.

The TOSCA configurations can also be useful in cases where the material or the environment is not compatible with electronics embedded in the focal plane, including use of detectors operating in photoconductive mode. The inherently perfect co-registration of

multiple spectral channels demonstrated in the experimental TOSCA multispectral imager makes the system attractive for low cost multi- or hyperspectral imaging applications.

The spin-scan linear array-based TOSCA imager is found to be the most efficient of the concepts tested so far. It presents particularly interesting characteristics for imaging while monitoring modulated or burst-mode noise sources in the image, with potential for doing corrections during exposure. Low cost and simplicity, on the other hand, might make the reticle based, conical scan TOSCA imager a popular alternative for educational purposes.

## 4.2 Further work

This work is by no means exhaustive in scope, and has only started an examination of the properties of some TOSCA configurations. The following is a brief summary of avenues of research that have not been covered.

### 4.2.1 Handling temporally varying sources

A spin scan TOSCA imager continuously monitoring the signal of all the detectors will in principle collect all photons and could detect significant variations in the total scan signal for each angular orientation. Characterization of rapidly modulated sources in the scene was mentioned in publication VI in this work, but experimental testing of such a capability was hindered by the nature of the readout configuration of the detector array available.

If a significant temporal variation is encountered, the image reconstruction is an underdetermined problem, since TOSCA reconstruction assumes a stationary scene. However if the application permits assumptions about the nature of temporally varying scenes then it is possible to extract information not accessible by normal TOSCA reconstruction. In practical cases, the most important such assumptions may be

- variation in global illumination
- a single or a few, temporally varying point sources on a constant background
- a transient flash on a constant background
- a point source entering or leaving the field of view

For these and other practical cases, an application-specific reconstruction process could extract, to varying degree, information about the stationary parts of the scene, the temporal variation and the position of point sources. More generally, the imager could be considered a compressive sensing system, with reconstruction applying methods similar to those employed by Candès *et al.* [86]. Thus a spin scan TOSCA system should have some

capability to not only detect, but also locate, characterize and compensate for a limited number of high frequency modulated point sources in an otherwise complex scene. Detection of such sources can be challenging, in particular if the duty cycle of both the source and the imager is small. The challenge can be met in certain cases if a single pixel detector is added to a classical 2D imager, but localization of the source(s) normally might require some other *a priori* knowledge about the source, particularly if the scene is cluttered. It is quite possible that the more intertwined connection between temporal and spatial behaviour in the TOSCA configuration is better suited to handle modulated sources.

If the rate of change in the scene is rapid compared to the frame rate, the change can generate significant artefacts. The process of reconstructing time-varying images is comparable to making helical (or spiral) scan 3D tomographic images, invented by Kalender [87]. In Kalender's approach, the helix spirals around the z-axis. To see changes as a function of time, time can replace the z-axis, while the tools are maintained in all other respects. It is therefore of interest to integrate the results from this research into the TOSCA imaging techniques to enhance behaviour in dynamic scenes.

### 4.2.2 Thin line array in MCT

It is feasible to fabricate an optimized infrared spin scan array-based imager using MCT. MCT is found to be particularly well suited for the thin line array, both in terms of the high mobility and suitable resistivity for the given geometry. In this respect, it is interesting to investigate the potential for a high speed, MCT-based spin scan TOSCA implementation. The material data used in the calculations below are given by Steen [88].

As an example, consider a square array of 64 thin line n-type photoconductive detectors designed for the mid-wave infrared range, each of length $L$ = 0.25 cm, and a width of approximately 40 μm. If we now supply a $V_0$ = 10V tension across each detector, the electrons would experience an electric field of $\xi_0$ = 40 V/cm. Assuming an electron mobility of $\mu_e = 5\times10^4$ cm$^2$/(V s), the average electron transit time across the entire line detector would be $t = L/(\mu_e\xi_0) = 0.125$ μs, which is well below the 0.3-1 μs electron carrier lifetime one might hope to achieve in such a geometry (in which the surface effects would likely dominate the bulk effects). The detector resistance would typically be $R_d \sim 5$ kΩ, leading to a thermal dissipation per detector of $P = V_0^2/R_d \sim 20$ mW, or a total array dissipation of ~1.2 W, easily manageable by current Stirling or Joule-Thomson cooler systems.

### 4.2.3 THz imaging

Terahertz imaging is a domain where array detector technology is immature. Single pixel based detectors exist, but the systems are still relatively slow, partly because of the lack of high power illuminators. As seen in this work, single pixel raster scan is found to be less efficient than the single pixel TOSCA scan, and a linear broom scan sensor is found to be theoretically less efficient for imaging than an array-based TOSCA imager if the light source illuminates the whole scene. It is therefore of interest to investigate the potential of a TOSCA implementation for THz imaging.

### 4.2.4 Fan-beam TOSCA imaging

Fan-beam TOSCA imaging is a concept in development, as a co-operation between Sebastian Möller at the Swedish Defence Research Establishment and the author. The concept is presented in figure 4.1.

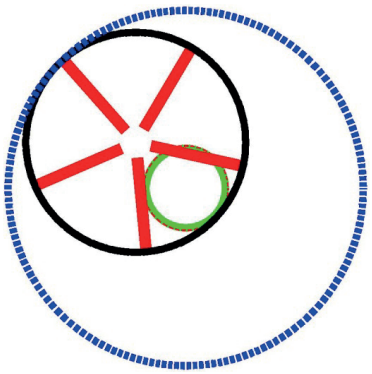

Figure 4.1. Fan-beam scan TOSCA concept. Incoming light from the scene is focused onto a circular mask (black circle) with thin slits (red) that rolls on the inside of a fixed perimeter (blue). When the thin slits crosses the circular aperture (green), passing through both hits a single pixel detector, creating a signal. If the ratio between the diameters of the blue and the black circle is well chosen (in this case 21:13), the number of independent fan beam scans can be high (105 in this case).

The general concept is that a reticle with a limited amount of slits rotates eccentrically in front of a stationary circular aperture. In this way, the signal generated by the slits as the reticle rotates creates several fan beams. This means the subsequent lines in a scan will no longer be parallel, but by recombining samples from several fan beam scans, it is possible to make a series of parallel samples (with a non-uniform spacing), as is done in regular X-ray CT imaging. By shaping the reticle as an external gear and letting it rotate eccentrically in a static internal gear, a good mechanical reference of the orientation is

maintained. As an example, using 5 regularly distributed slits, and an internal to external gear diameter ratio of 21:13, it is possible to create 105 different fan beam scans before the process is repeated.

### 4.2.5 TOSCA imaging without moving parts

It is interesting to consider options for TOSCA imaging where the scanning is implemented in microelectronics, without moving parts. One approach is sketched below. The main idea here is to do imaging with modulated sources in the field of view. By creating a honeycomb cell structure as in figure 4.2(a), where each cell is connected to neighbouring cells through switchable electronic barriers similar to the ones used in charge coupled device (CCD) structures, synthetically generated "lines" could be generated. Figure 4.2(b) shows one out of three electronic gating structures. One such gating structure provides a ±30° scan. The next gating structure is connected in a similar way, but rotated 60°, and a third gating structure is rotated 120°, compared to the first gating structure. Readout is done at the edge of the cell array.

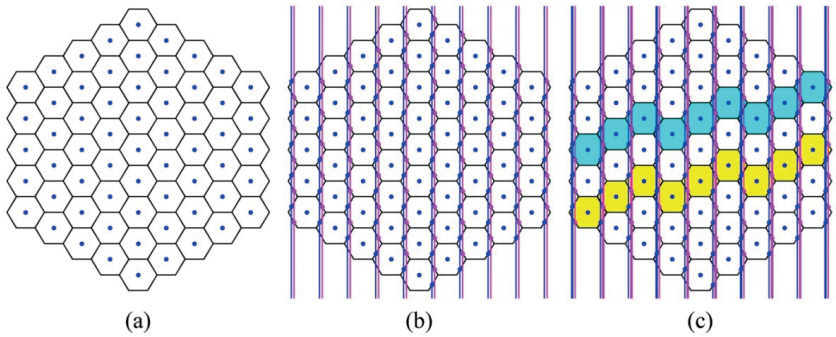


Figure 4.2. (a) Grid type of potential TOSCA sensor without moving parts. Each cell is by default isolated, but can be connected to its 6 neighbours by dynamically lowering the walls, as is done in CCD structures. (b) One of three gating structures to connect neighbouring cells. Each gating line is acting on a set of cell walls, as marked by dots. A blue/magenta gating pair values would not open at the same time (but could be closed simultaneously). The two other gating structures (not shown) would be 60° and 120° rotated with respect to the one shown, respectively. (c) Example of connected cells when selected gating lines open (indicated with bold lines).

When only the blue gates are "ON", a -30° scan orientation is generated, and with only the magenta lines in the "ON" state, a +30° scan orientation is generated. Figure 4.2(c) shows an example of how an intermediate scan line orientation could be generated, by selectively switching the blue or magenta lines "ON", as indicated with bold lines.

It can be proven that a scan pattern exists that could create orthogonality in the ideal situation, along the lines in [89], hence in principle enabling artifact free reconstruction. Using one of the three gating structures, any two cells can be connected together, most pairs in multiple ways.

An approximately circular scan with arbitrarily adjustable angular resolution could hence be performed. Handling of modulated sources, such as the lamps from an emergency vehicle, can also be handled during the generation of the frames. If a transient occurs during the scan, this can be detected by accumulating line values and comparing the total energy with previous accumulated values. If the energy is beyond an estimated threshold value, the scan can be repeated at a later time. As the scanning is electronic and not mechanical, it is possible to measure an arbitrary scan angle at any time. This has potential to produce images without these artefacts, and also to enable a characterization of the modulated source. If the modulation is higher than the frame rate, this will then merely increase the frame rate slightly.

The implementation of the electronic scan is of course challenging, and may turn out to be infeasible in practice. For example, a high mobility would be required to swipe the charges out through the lines before the gate switches changes the scan line configuration. Generally, this hexagonal structure, being uncommon in the industry, might require substantial investments and research related to manufacturing.

# Bibliography


[1] W. Herschel, “Experiments on the Refrangibility of the invisible Rays of the Sun”, Phil. Trans. Pt. II, 90, pp. 284-292 (1800).

[2] R. V. Jones, “Infrared detection in British air defence, 1935-1938”, Infrared Phys., 1, pp. 153-162 (1961).

[3] M. Lindroos, Ö. Skeppstedt, “A position sensitive photon detector used as a charged particle detector,” Nucl. Instr. And Meth. A, **306**, 1, pp. 225-228, (1991).

[4] V. E. Carbonara et al., “Star tracking system,” US Patent 2972812, (1961).

[5] A. Mäkynen, “Position-sensitive devices and sensor systems for optical tracking and displacement sensing applications”, PhD thesis, ISBN 951-42-5780-4, University of Oulu (2000). http://herkules.oulu.fi/issn03553213/

[6] A. H. Pfund, “Resonance Radiometry,” Science, **69**, 1777, pp. 71-72 (1929).

[7] C. Kopp, “Genesis of the surface-to-air missile,” Defence Today (Sep/Oct 2006). Available on Air Power Australia web site: http://www.ausairpower.net/SP/DT-MS-1006, (downloaded 31.10.2014).

[8] C. Reuter, “The V2 and the German, Russian and American rocket program,” S. R. Research & Publishing, 2. Ed. (2000). ISBN 978-1894643054.

[9] D.G. Blanchard, “A brief history of the air-intercept missile 9 (Sidewinder), 32nd Joint propulsion conference and exhibit, AIAA paper 96-3154, (1996).

[10] E. W. Kutzscher, Proc. IRIS, **1**, 5 (1956).

[11] H. L. Clark, “Sun follower for V-2 Rockets,” Electronics, **23**, 71, (1950).

[12] L. M. Biberman, *Reticles in electrooptical devices*, Pergamon, New York, (1966).

[13] L. Biberman, R. Estey, “Multislit scanner,” US Patent 3034405, (1962).

[14] R. O’B. Carpenter, “Comparison of AM and FM Reticle Systems”, Appl. Opt., **2**, 3, pp. 229-236 (1963).

[15] R. A. Driggers, “Discrete frequency-versus-radius reticle trackers,” Proc. SPIE, **1478**, pp. 24-32, (1991).

[16] J. S. Taylor, K. A. Krapels, “FM reticle trackers in the pupil plane,” Proc. SPIE, **1478**, pp. 41-49, (1991).

[17] D. J. Lovell, “Electro-optical position indicator system,” US Patent 2997699, (1961).

[18] R D Hudson, *Infrared Systems Engineering,* 235-263, John Wiley & Sons Inc, Hoboken, NJ, USA (1969, reprinted 2006).

[19] R. Driggers (ed.), *Encyclopedia of Optical Engineering*, vol. 3, pp. 2417-2444, CRC, (2003). ISBN 978-0824742522.

[20] K. Tihanyi, “Television apparatus,” US patent 2158259, (1939).

[21] V. K. Zworykin, “Method and apparatus for producing images of objects,” US patent 2021907, (1935).

[22] M. El-Desouki et al., “CMOS image sensors for high speed applications,” Sensors **2009**, 1, pp. 430-444, (2009).

[23] B. W. Mott et al., “Large format HgCdTe arrays for the James Webb space telescope,” LEOS Summer Topical Meetings, pp. 38-39, (2006).

[24] J. Rothmann et al., “History-dependent impact ionization theory applied to HgCdTe e-APDs,” J. Elec. Mat. **40**, 8, pp. 1757-1768, (2011).
[25] M.A. Kinch, I. M. Baker, *HgCdTe electron avalanche photodiodes*, ch. 21, Mercury Cadmium Telluride – Growth, Properties and Applications, Wiley, (2011).
[26] D. J. Brady, “Petapixel photography and the limits on camera information capacity,” Proc. SPIE **8657**, 86570B (2013).
[27] Cincinatti Electronics (L3) sales brochure downloaded 2014.
[28] FLIR sales representative, personal communications at SPIE DSS symposium, (2014).
[29] NEC internet page,http://www.nec.com/en/global/prod/terahertz/ Downloaded 12.11.2014.
[30] M. Minsky, “Microscopy apparatus,” US patent 3013467, (1961).
[31] H. Goldman, “Spaltlampenphotographie und –photometrie,” Opthalmologica **98**, 5/6, 257-270, (1939).
[32] R. Wolleschensky et al., “High-speed confocal fluorescence imaging with a novel line scanning microscope,” J. Biomed. Opt. **11**, 6, 064011, (2006).
[33] J. S. Sanders, R. G. Driggers, C. E. Halford, S. T. Griffin, "Imaging with Frequency-Modulated Reticles," Opt. Eng. **30**, 11, pp. 1720-1724, (1991).
[34] J. K. Bae, Y. H. Doh, D. S. Noh, S. J. Kim, "Imaging system using frequency modulation/time division multiplexing hybrid reticle," Opt. Eng. 37, pp. 2119-2123, (1998).
[35] R. G. Driggers, C. E. Halford, G. D. Boreman, “Marriage of frequency modulation reticles to focal plane arrays”, Opt. Eng., **30**, 10, pp. 1516-1521, (1991).
[36] H. K. Hong, S. H. Han, J. S. Choi, "Improved reticle seeker using the segmented focal plane array," Proc. SPIE **2744**, pp. 433-440, (1996).
[37] S. Shapiro, “Infrared search and tracking system comprising a plurality of detectors,” US patent 3106642, (1963).
[38] C. Jutten, J. Herault, “Blind Separation of Sources,” Signal Process. **24**, 1, pp. 1-10, (1991).
[39] I. Kopriva, A. Persin, "Discrimination of optical sources by use of adaptive blind source separation theory," App. Opt. **38**, 7, pp. 1115-1126, (1999).
[40] I. Kopriva, H. Szu, A Peršin, “Optical reticle trackers with the multi-source discrimination capability by using independent component analysis”, Opt. Comm. **203**, pp. 197-211, (2002).
[41] H. Szu, I. Kopriva, A Peršin, “Independent component analysis approach to resolve the multi-source limitation of the nutating rising-sun reticle based optical trackers”, Opt. Comm. **176**, pp. 77-89, (2000).
[42] P. A. Manning et al. “A reconfigurable low-cost thermal imager for unattended ground sensors,” Proc. SPIE **6394**, 63940S, (2006).
[43] P. Schlup et al., “Lateral Tomographic spatial frequency modulated imaging,” Appl. Phys. Lett. **98**, 211115, (2011).
[44] G. Futia et al., “Spatially-chirped modulation imaging of absorption and fluorescent objects on single-element detector,” Opt. Express **19**, 2, pp. 1626-1640, (2011).
[45] D. J. Higley et al., “Two-dimensional spatial-frequency-modulated imaging through parallel acquisition of line images,” Opt. Lett. **38**, 11, pp. 1763-1765, (2013).

[46] J. Radon, “Über die bestimmung von Funktionen durch ihre Integralwerte langsgewisser Mannigfaltigkeiten (On the Determination of Functions From Their Integrals Along Certain Manifolds)”, Berichte Sachsische Akademie Wissenschaften, **29**, 262-277 (1917), or same title, Math. Phys. Klass., **69**, (1917). (Both texts in German).
[47] E. M. Bocage, “Technique and Mechanism of a moving X-ray film,” French patent 536464, (1921).
[48] B. Pollak, “Experiences with Planography,” Chest **24**, 6, (1953).
[49] H. Cramer, H. Wold, “Some theorems on distribution functions”, J. London Math. Soc. **11**, pp. 290-294, (1936).
[50] A. M. Cormack, “Representation of a function by its line integrals, with some radiological applications,” J. Appl. Phys. **34**, pp. 2722-2727, (1963).
[51] A. M. Cormack, “Representation of a function by its line integrals, with some radiological applications. II,” J. Appl. Phys. **35**, pp. 2908-2913, (1963).
[52] G. N. Hounsfield, “A method of and apparatus for examination of a body by radiation such as X- or gamma-radiation.” UK Patent 1283915, (1972).
[53] R. N. Bracewell, A. C. Riddle, “Inversion of fan-beam scans in radio astronomy,” Astrophys. Journal, **150**, pp. 427 - 434, (1967).
[54] P. D. Rowley, “Quantitative interpretation of three-dimensional weakly refractive phase objects using holographic interferometry,” JOSA **59**, 11, pp. 1496-1498, (1969).
[55] M. V. Berry, D. F. Gibbs, “The interpretation of optical projections,” Proc. Roy. Soc. Lond. A **314**, pp. 143-152, (1970).
[56] M. Sandborg, “Computed Tomography: Physical principles and biohazards”, Report 81 ISSN 1102-1799, September 1995. See also http://huweb.hu.liu.se/inst/imv/radiofysik/pdfs/Rap81.pdf.
[57] www.gehealthcare.com.
[58] http://www.healthcare.siemens.com/computed-tomography.
[59] M. Holler et al., “X-ray ptychographic computed tomography at 16 nm isotropic 3D resolution,” Scientific Reports **4**, 3857 (2014). See also http://www.nature.com/srep/2014/140124/srep03857/full/srep03857.html.
[60] P. Kraft, “PILATUS 2M – A detector for small angle X-ray scattering,” Doctoral thesis, ETH Zurich (2010), Diss. ETH No. 18466.
[61] Marketstrat, “Computed Tomography (CT) systems market worldwide,” www.marketstrat.com (2009).
[62] R. E. Hansen, *Introduction to synthetic aperture sonar, Sonar systems*, N. Z. Kolev (Ed), InTech (2011). ISBN 978-9533073453.
[63] M. P. Hayes, P. T. Gough, “Synthetic aperture sonar: A review of current status”, IEEE J. Ocean Eng., **34**, 3, 207-224 (2009).
[64] T. O. Sæbø et al., “Wideband interferometry in synthetic aperture sonar,” IEEE Trans. Geosci. Remote Sens., **51**, 8, pp. 4450-4459, (2013).
[65] A. C. Kak, M. Slaney, *Principles of Computerized Tomographic Imaging*, IEEE Press (1988). Also available online at http://www.slaney.org/pct/pct-toc.html.
[66] F. Natterer, *The Mathematics of Computerized Tomography*, Wiley-Teubner 2001. ISBN 0898714931.
[67] J. Hsieh, *Computed tomography principles, design, artefacts, and recent advances*, (SPIE Optical Engineering Press, Bellingham, WA, 2003).
[68] G. T. Herman, *Fundamentals of computerized tomography*, Academic Press (1980, 2nd ed. 2010). ISBN 978-1-84628-723-7.

[69] G. T. Herman, *Image Reconstructions from Projections*, (Academic Press, New York, 1980).
[70] S. R. Deans, *The Radon transform and some of its applications*, Wiley (1983). Republished as paperback in 2007 by Dover Publications. ISBN 978-0486462417.
[71] S. Quabis et al., "The focus of light - theoretical calculation and experimental tomographic reconstruction," App. Phys. B-Lasers and Optics **72**, 1, pp. 109-113, (2001).
[72] H. E. Torkildsen et al., "Characterization of a compact 6-band multifunctional camera based on patterned spectral filters in the focal plane," Proc. SPIE **9088**, 908819 (2014).
[73] G. N. Ramachandran, A. V. Lakshminarayanan, "3-Dimensional Reconstruction from Radiographs and Electron Micrographs - Application of Convolutions Instead of Fourier Transforms," Proc. Natl. Acad. Sci. U. S. A. **68**, 9, pp. 2236-2240, (1971).
[74] A. H. Andersen, A. C. Kak, "Simultaneous algebraic reconstruction technique (SART): A superior implementation of the art algorithm," Ultrason. Imaging **6**, pp. 81-94, (1984).
[75] T. Ilovitsh et al., "Optical realization of the radon transform," Opt. Express **22,** 6, pp. 32509-32519, (2014).
[76] https://eoportal.org/web/eoportal/satellite-missions/l/landsat-4-5
[77] J. Pearlman et al., "Development and operations of the EO-1 Hyperion imaging spectrometer," Proc. SPIE **4135**, pp. 243-253, (2000).
[78] G. G. Levin, G. N. Vishnyakov, "On the possibilities of chromotomography of high speed processes," Opt. Comm. **56**, 4, pp. 231-234, (1985).
[79] J. M. Mooney, "Angularly multiplexed spectral imager," Proc. SPIE **2480**, pp. 65-77, (1995)
[80] M. Descour, E. Dereniak, "Computed tomography imaging spectrometer: experimental calibration and reconstruction results," Appl. Opt. **34**, 22, pp. 4817-4826, (1995).
[81] R. D. Alcock, J. M. Coupland, "A compact, high numerical aperture imaging Fourier transform spectrometer and its application," Meas. Sci. Tech. **17**, 11, pp. 2861-2868, (2006).
[82] J. S. Sanders, C. E. Halford, "Multispectral imaging with frequency-modulated reticles," Proc. SPIE **1478**, pp 52-63, (1991).
[83] M. T. Eismann, *Hyperspectral remote sensing*, SPIE Press Monograph PM210, (2012). ISBN 978-0819487872.
[84] P. Mourolis et al., "Design of pushbroom imaging spectrometers for optimum recovery of spectroscopic and spatial information," Appl. Opt. **39**, pp. 2210-2220, (2000).
[85] T. Skauli, "Quantifying coregistration errors in spectral imaging," Proc. SPIE **8158**, 81580A, (2011).
[86] E. J. Candès, J. Romberg, T. Tao, "Robust uncertainty principles: exact signal reconstruction from highly incomplete frequency information," IEEE Trans. Inform. Theory, **52** (2), pp. 489-509, (2006).
[87] W. A. Kalender, "Technical foundations of spiral CT," Seminars in Ultrasound, CT and MRI, **15**, 2, pp. 81-89, (1994).
[88] Helge Steen, Norwegian Defence Research Establishment, private communications, January 2015.

[89] W. H. Press, “Discrete Radon transform has an exact, fast inverse and generalizes to operations other than sums along lines,” PNAS, **103** (51), pp. 19249-19254 (2006).

# Publications

# Publication I

# TOMOGRAPHIC SCANNING IMAGING SEEKER

**Harald Hovland**

**Proc. SPIE 5430, Acquisition, Tracking and Pointing XVIII, pp. 58-64, (2004)**

# Tomographic scanning imaging seeker

Harald Hovland
Norwegian Defence Research Establishment (FFI),
Information Management Division
P O box 25, NO-2027 Kjeller, NORWAY
harald.hovland@ffi.no

## ABSTRACT

A new imaging technique is introduced, based on tomographic imaging principles applied to the output from a conical scan reticle system. The concept allows for a simple, low cost system consisting of simple scanning optics, a single element detector and a signal-processing unit to act as an imaging sensor. Potential applications of the tomographic scanning imaging (TOSCA) seeker include missile seekers, smart munitions, and other devices using low-cost imagers.

**Keywords**: Tomography, conical scan, imaging, reticle, seeker, missile

## 1. INTRODUCTION

### 1.1 Reticle seekers

Reticle seekers have been in use in missiles for half a century now, and were fitted on the first practical "fire and forget"-type infrared (IR) guided weapons to become operational. Infrared radiation was discovered by Herschel[1], and was proposed as means of detecting aircraft in 1916 by Lindemann[2]. The use of infrared detection in missile guidance was explored by the Germans during World War II[3]. Practical systems, however, were not available until the 1950's, when the AIM-9 "Sidewinder" became operational[4]. The sidewinder employed a spin-scan reticle seeker with amplitude modulation (AM).

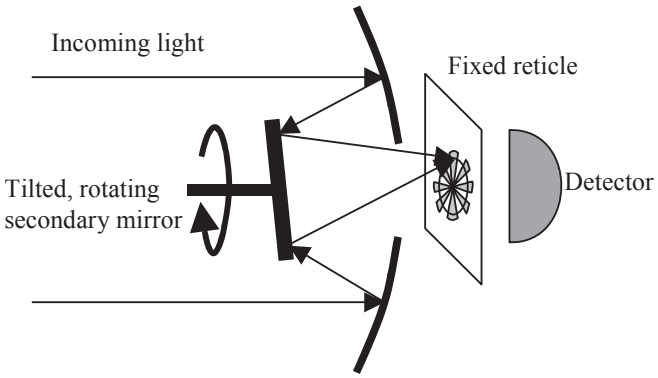


Figure 1. Principle of the conical scan reticle FM seeker. A spinning, tilted mirror projects the target image onto the fixed reticle in a circular movement. The reticle contains several fields with different transparency. The light passing through the transparent sectors of the reticle are collected onto a detector, producing a signal. With a suitable spot size, a centred target image will produce a sinusoidal signal with a constant frequency. A decentred target will produce a sinusoidal signal with a varying frequency.

Later, the use of conical scanning frequency-modulated (FM) missile seekers largely replaced the spin-scan technology, primarily due to improved detector materials and

increased signal-to-noise ratio of the FM seeker[5]. Other seeker principles have appeared later on, such as the circular line scan, cross-bar conical scan and the rosette scan detectors. The simplicity and low cost of the con-scan FM reticle seeker technology has made it popular and long-lived. The principle of the con-scan reticle seeker is shown in figure 1.

### 1.2 Imaging systems

Imaging systems have distinct advantages in tracking processes if several targets (true and false) are present. Several imaging or pseudo-imaging systems have therefore been proposed and even deployed. Among the most common are the rosette scan system, linear sweep system using a linear array, and staring or step-stare systems using focal plane arrays. A combination of simple low-pixel-count focal plane arrays and a spin-scan FM-reticle system have been proposed by Driggers et al. [6] and Hong et al.[7]

Kopriva et al. have used independent component analysis in spin-scan[8] and con-scan[9] system using a spectral beamsplitter and two detectors to be able to separate several point sources.

Generally speaking, these systems either use somewhat complex scanning, multiple detectors or restricts themselves to locating point sources. It will in the following be seen that a low-cost imaging system can be obtained by applying tomography reconstruction on the output from a high-resolution con-scan seeker.

### 1.3 Tomographic imaging

The basic theory of tomography goes back to work by Johann Radon in 1917[10]. Computer tomography imaging was invented by Godfrey Hounsfield of EMI Laboratories, in 1972 as a non-invasive means to produce cross section images of the human body by the use of X-rays. This invention earned him the 1979 Nobel Prize in medicine together with Allan Cormack of Tufts University, Massachusetts. The principle behind the tomographic reconstruction process is based on the creation of several lower dimensional projections of the object that are then used to reconstruct a higher dimensional image. In the simplest process, a 2-dimensional object is measured N times from different angles with a process that creates N 1-dimensional projections. These projections are then processed to create N 2-dimensional partial images that are superposed to create the final image. The higher N is, the better is the final image, ideally leading to a perfect image when N becomes infinite.

In one of the simplest examples, an x-ray with initial intensity $I_0$ transverses a two-dimensional non-scattering object by that absorbs the x-rays in a non-refractive, inhomogeneous way, and the remaining intensity $I_d$ is detected on the other side of the object. The absorption along a short length *dz* through the object where the optical density $\sigma(z)$ can be expressed by:

$$dI = I(z) - I(z+dz) = I(z)\exp\left[-\sigma(z)dz\right]. \qquad \text{Eq. 1}$$

Integrated over the full length *d* of the line segment through the body, one gets:

$$\frac{I_d}{I_0} = \frac{I(z_0+d)}{I(z_0)} = \exp\left[-\int_{z_0}^{z_0+d}\sigma(z)dz\right]. \qquad \text{Eq. 2}$$

The average optical density $\hat{\sigma}$ along the line segment of length *d* can then be expressed by:

$$\hat{\sigma} = \frac{1}{d}\int_{z_0}^{z_0+d} \sigma(z)\,dz = \ln\left(\frac{I_0}{I_d}\right), \qquad \text{Eq. 3}$$

The ray can be scanned across the whole object, with the optical axis and the scan direction always being kept orthogonal to each other, thus creating a 1-dimensional distribution of the average optical density of the object. The scan process is repeated many times, but each time with a different scan direction (the ray still being orthogonal to the scan direction), the orientation being changed by a fixed angle increment. In this way, a large number of 1-dimensional (averaged) optical density distributions are recorded. A perfect reconstruction can in principle be made with an infinite number of scans are made with infinitely small angular increments.

There are several techniques available to do the reconstruction. There are also other ways to do computer tomography, the mathematics reflecting the differences in geometry and physical measurement processes involved in solving the particular imaging problem[11]. As an example of the big variety, it can be seen that the rays need not be parallel (in commercial CAT-scanners they generally are not), and they do not even have to be straight lines, for example if refraction is included in the model, like in ultrasound or microwave tomography. Currently computer tomography can even be used to resolve objects in strongly scattering media, as is done in optical tomography, where near infrared lasers illuminate the body, and where transport equations account for the movement of scattered light in the body. It should be noted that the TOSCA process differs significantly from what is known as optical tomography.

In practical medical x-ray CAT scan machines, an x-ray point source produces a fan beam of radiation that is detected by some 700 detectors that are placed on the opposite side of the object to be imaged. About 1000 projections are made at different angles, producing a 512×512 image matrix[12].

## 2. The basic TOSCA seeker

### 2.1 The TOSCA concept

Normally, a reticle seeker is operated as a point tracker, and does not exploit the shape of the target. In the TOSCA approach, the single pixel detector output is found to deliver shape information that can be extracted using tomographic techniques.

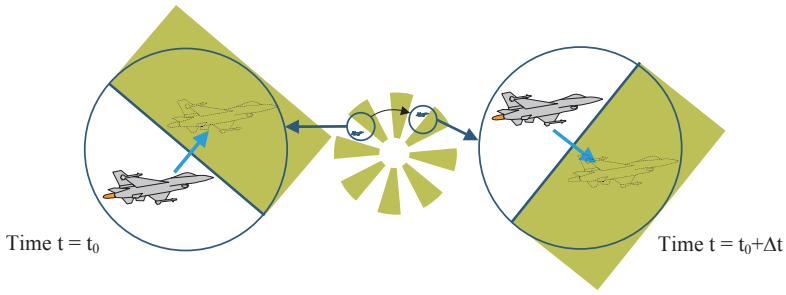


Figure 2. In the con-scan reticle seeker, the scanning of a target across a reticle transmission step can be thought of as a knife-edge detection process. The time derivative of the resulting signal is a 1-dimensional projection of the 2-dimensional target normal to the transmission step line. Both positive and negative transmission steps produce a signal.

The tomographic scanning seeker concept was incepted by realizing that when an object is scanned across a reticle in a con-scan reticle seeker, it is scanned across several knife-edges with a translation movement, as shown in figure 2.

If the resolution is sufficiently high, the derivative of the signal thus obtained gives the 1-dimensional projection of the target intensity distribution along the direction normal to the knife-edge. This is shown in the following:

We assume that the image is given as an intensity distribution *I(x,y)*, with the coordinate system moving with a circular movement around the reticle in such a way that the image can be considered static with respect to it. In the perfect case, an infinite number of infinite knife-edges are scanned across the image sequentially. If the scan angle is $\theta$, the signal obtained across an idealized knife-edge becomes:

$$S_\theta(t) = \int_{-\infty}^{+\infty} dx'_\theta \int_{-\infty}^{vt+y'_{\theta,0}} dy'_\theta I_\theta\left(x'_\theta, y'_\theta\right), \qquad \text{Eq. 4}$$

where *t* denotes time, $v_\theta$ the scan speed, $y'_{\theta,0}$ a value determined by the position of the knife edge at time *t=0*. The use of $x'_\theta$ and $y'_\theta$ indicates that we by convenience are using a coordinate system aligned with the scan direction. The time derivative of this signal is found to be:

$$S'_\theta(t) = \frac{d}{dt} S_\theta(t) = \int_{-\infty}^{+\infty} dx'_\theta \, I_\theta\left(x'_\theta, v_\theta t + y'_{\theta,0}\right), \qquad \text{Eq. 5}$$

If in addition a circularly scanning aperture is used to limit the field of view, undesirable edge effects (where for example a bright spot on the edge of the total scanning field of view is only partially inside the instantaneous reticle field-of view) are eliminated. The angular difference between the knife-edges is constant, and the problem is reduced to solving the classical tomography equations for the parallel scanning problem, a problem that has an exact solution[11].

### 2.2 The generalized TOSCA seeker

In the previous sections, it has been assumed that only one knife-edge is visible at a time. This can be achieved by using a rotating eccentric aperture that passes right in front of, or behind the reticle. However, it is found that the TOSCA method can be extended to also cover the application where there is no rotating aperture in front of the reticle. In this way, it is possible to produce enhanced functionality to reticle seekers. As an example one might use classical reticle target tracking for acquisition, and then benefit from the imaging properties of the TOSCA technique to recognize or identify the target, possibly also to separate a flare from the aircraft at an early stage in the flare deployment. Two generalizations of the TOSCA method are:

1. The gradient at the knife edge can be smooth, and
2. The gradient does not need to be parallel with the scan direction.

The first point is equally valid both with and without the rotating eccentric aperture. The second point allows for the use of more general reticle shapes. As will be seen in the next section, a more complex reticle can yield several hot spots due to the coincidence of signals that originates from several nonparallel gradients. This leads to aliasing.

In the generalized version, the somewhat rigid concept of a rectilinear knife-edge is replaced by the more general gradient concept. We will now look at the requirements of such a system.

Ideally we want a total signal generation - reconstruction process that leads to an identity transform:

$$I(x,y) \xrightarrow{\text{signal generation}} S'(t) \xrightarrow{\text{regeneration}} I_R(x,y) = I(x,y) \qquad \text{Eq. 6}$$

This will be the case if the transform is linear and if any point source is reconstructed to a point source with the same location as the original point source. As the signal generation process is linear (not accounting for noise), the regeneration process must also be linear.

**2.3 One solution in an ideal case**

We saw in section 1 that an exact solution exists in the ideal knife-edge case. We now consider the case where the scan radius *r* is very (infinitely) large and a circular moving aperture with diameter *L* is following the image of the target. The resulting spatially filtered image scans in a circular movement across a regular reticle with n evenly distributed sectors, where $n = \frac{2\pi r}{L}$. The image, filtered by the aperture, will then scan across each sector interface separately, and the signal becomes that of a knife-edge, giving rise to the expression in equation 5 and to an exact reconstruction.

**2.4 Restrictions in the non-ideal case, using a moving circular aperture**

If a moving circular aperture is used in the non-ideal case, each knife-edge can act individually on the field-of-view, and their sizes surpass the aperture, and as such, appear infinite. With a limited scan radius r and a finite field of view, the number of different knife-edges is limited, and there will also be a limit due to system bandwidth.

The Fourier domain is seen to have an incomplete set of (discrete) values. From an information theory point of view, the limited amount of sample points can lead to aliasing and artefacts. If, however, the size and the resolution of the Fourier domain are limited, the artefacts can be minimized. It should be noted, however, that artefacts might be acceptable to a certain degree, depending on the specific application requirements and the following image processing. The limitations will equally well apply to the reconstructed signal in the spatial domain, leading to a low-pass filtered image.

One interesting thing to note is the fact that the sampling is not equidistant in the spatial domain, as the main limitation typically will be angular in nature. For objects that are close to each other, the angular uncertainty leads to only small position uncertainties, and it is therefore possible to identify very closely separated objects.

It should also be mentioned that as the knife-edge scan is not done with a linear scan, but rather with a circular movement, the effective result is a modification of the scan speed.

**2.5 Effect of not using an aperture**

If a finite reticle size is used in a system that does not comprise a circular aperture system, the following effects apply:

- Artefacts due to the fact that the knife-edges are not infinite
- The superposition of several knife-edges with an angular difference. This leads to aliasing.

It can be seen that if only a small cluster of targets is present in the image centre within a circle of diameter $L = \frac{2\pi r}{n}$ on an otherwise homogeneous background, using an aperture would have no apparent effect in the recreation of this central part. It should be noted, though, that the surrounding area would contain aliasing artefacts. In the same manner, aliasing artefacts from sources outside the inner circle but inside an outer circle with diameter *2r+K*, where *K* is the reticle diameter, will be visible inside the circle.

## 3. Practical limitations of the TOSCA seeker

There are of course several limits to the process for a practical system. Some of these are:

- Limited number of different reticle knife edge transition
- Limitations in the image processing array
- Limited optical resolution
- Limited field of view
- Limited detector bandwidth
- Inhomogeneous background
- Limited detector dynamics
- Aliasing problems
- Detector noise
- Mechanical limitations and noise
- Temporal and spatial background and target noise

We will now look at some of the properties of the system, and suggest some typical parameters of a system.

### 3.1 Number of knife-edge transitions

In a practical system, there will be a trade-off between the field of view and the number of knife-edge transitions, and it is of interest to have a rough idea about a practical upper number of transitions possible. Consider a system with a fixed reticle. Important design parameters will be:

- Optical aperture *D*
- Focal length *f*
- Field of view $\varphi$
- Scan radius *r* (distance from reticle centre to the image centre)

The image size *L* on the reticle is given by:

$$L = f\varphi . \qquad \text{Eq. 7}$$

The upper number *n* of knife-edges that can be placed on the reticle is given by the ratio of the circumference of the circle defined by the scan radius, and the image size on the reticle:

$$n = \frac{2\pi r}{L} = \frac{2\pi r}{f\varphi}. \qquad \text{Eq. 8}$$

It should be noticed that the knife edge oriented along a given line can have two directions compared with the scan, either hiding more and more of the target, or revealing more and more of the target. A high value of $n$ is in general preferable, but an upper limit for a system would be given by $r \leq D$ and $D \leq f$, so that $r$ should not be any larger than $f$. We therefore set $r = f$ as an upper limit for $n$. The value of $\varphi$ is more difficult to specify as it depends on the application, but one might take a field of view of $\varphi = 4° \approx 0.07$ rad as a tentative value. This gives $n \approx 90$. It is important to notice that unless transitions other than from ~0% transmission to ~100% transmission are allowed, the number n of knife-edge transitions would always be pair. Furthermore, if a symmetrical spokes reticle is used, the effective number of different transitions would only be $n/2$, as diametrally opposed knife-edges have a 180° angular shift, and would be equivalent. It is possible to avoid this problem in at least two ways: either to allow for intermediate reticle transmissions to make n an odd value, or to let one or several sectors be larger than the others. This would lead to some angular artefacts, but the advantages in terms of increased resolution are likely to counter these disadvantages, especially if $n$ is large.

The intent of the system was to produce a low-cost system, and the assumption of $r = f$ is therefore probably somewhat optimistic. With the 4° field of view, a value of $n = 50$ is probably more likely.

### 3.2 Optical and temporal resolution

Two important limitations to the resolution is the optical resolution, whereby the image of a point source has a finite extent on the reticle. Together with the field of view, this can determine what size one might hope to have on an imaging matrix. The diffraction limit gives a spot size $s$ of:

$$s \approx \frac{1.2\lambda f}{D}. \qquad \text{Eq. 9}$$

Assuming $f = 2D$, and $\lambda = 4$ µm, one gets $s \approx 10$ µm.

The ratio between the field of view and the spot size is given by:

$$\frac{L}{s} \approx \frac{D\varphi f}{1.2\lambda f} = \frac{D\varphi}{1.2\lambda}. \qquad \text{Eq. 10}$$

In a missile application, one might have $D = 5$ cm, $f = 10$ cm and the 4° field of view, giving a ratio between the field of view and the spot size of $L / s \approx 730$. A practical low-cost system is likely to have a lower ratio than this. A tentative value of 200 is used further on in the calculations.

The way of taking samples in the rising sun reticle case with a moving aperture lead to an even point distribution along several lines with a common centre in Fourier space. The maximum possible number of individual sample points to make up an image is therefore seen to be approximately the scan circle circumference divided by the spot size, or lower if the sampling process is too slow. Of these, half are redundant, as diametrically opposed knife-edges have the same direction, and thus do not add to the spatial resolution. This

limits the information value in terms of the number of image pixels that might be retrieved in each frame to:

$$\Omega \approx \frac{\pi r}{s} \approx \frac{nL}{2s}. \qquad \text{Eq. 11}$$

This would have corresponded roughly to a matrix with side $\sqrt{\Omega}$, had the spatial sampling been evenly spaced. Assuming a required frame rate $F$ of 100 Hz, $n$ = 50 and $L/s$ = 200, an approximate detection bandwidth of 100 kHz would be required if full advantage could be taken of the small spot size. We then roughly have $\sqrt{\Omega} \approx 70$.

### 3.3 Noise and background variations

Several noise sources can be identified that would affect the system. They include:

- Intrinsic detector noise.
- Changing the field of view. This would affect the signal, as the background is generally not homogeneous.
- Temporal variation in the background or target radiation. As this is a spatially integrating system, variations in the field of view already seen by the detector create anomalies positioned near the knife-edge.
- Limited field of view. The field of view will ultimately have a specific shape. A square shape (or truncated sector) will facilitate processing, but this shape would then rotate with the scan angle and cover different areas of the field of view, especially close to the vertices. Alternatively, a circular field of view could be used, but this would require more processing, as the knife-edge would have a varying length throughout the scan.

Combined with a limited dynamic range of the detector, this reduces the amount of information that can be exploited in the system.

### 3.4 Spot size broadening due to sampling

In addition, there are resolution limitations due to sampling. If a point target is situated in a pixel, each of the eight surrounding pixels will have approximately ¼ of the signal in the centre pixel. Each scan line will pass by at least two of these neighbouring pixels. This will broaden the spot size. It is important to notice that this result does not depend on the number of knife-edges in use.

Another effect that will broaden the spot size is vibrations as well as offset and noise in the timing. It is expected that improvements could be made by comparing the signal profile with the expected profile, and adjust the timing accordingly.

### 3.5 Aliasing

Aliasing can be a problem whenever the number of knife-edge scans is limited. Typically, if the number of point sources approaches or exceeds the number of knife-edge scans, and groups of these point sources have particular geometric relations, special artefacts will occur. As an example, if a group of points are aligned, a continuous line will appear in the image along these points. If two lines formed by such points intersect, a point is formed at the intersection of these points.

## 4. SIMULATION EXAMPLES OF TOSCA SEEKER WITHOUT APERTURE

The following examples were produced using Matlab and a hybrid image, consisting of an aircraft with simulated flares (an ellipsoid with a Gaussian intensity profile), as seen in figures 3, 8 and 12. In both cases, the backgrounds are reasonably smooth, but not homogeneous. Figure 4 shows the reticle used in the simulations, with correct scaling compared to figures 3, 5, 8, 9, 12 and 13. The scanning radius is set to 2/3 of the reticle diameter. The scanning was done with 12 000 steps, but roundoff was used instead of interpolation in the matrix calculation, so the effective bandwidth was lower than the number of sample points would indicate. An estimate of the theoretical spatial information value $\Omega$ can be given as half the scan circle perimeter, measured in pixels. The reticle diameter is 176 pixels, giving a value of $\Omega \approx 184$, corresponding roughly to a matrix with side 13 or 14. This clearly is a fairly crude imaging system.

Figure 3 shows a situation where the separation is reasonably small, and figure 5 shows the reconstructed image.

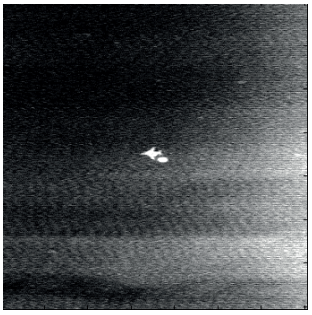

Figure 3. Original image, close separation.

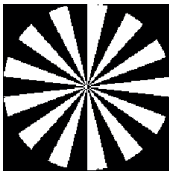

Figure 4. Reticle shape used.

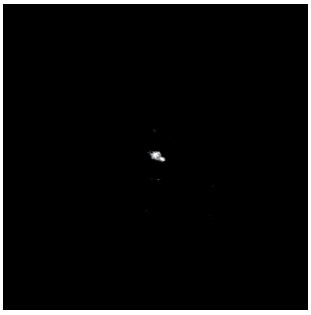

Figure 5. Reconstruction of image in figure 3.

Figure 6 and 7 show a close-up view of the corresponding central portions of the original and the reconstructed image. It can be seen that the aircraft image is blurred, but the two objects are clearly discernible, and their positions are reasonably well maintained.

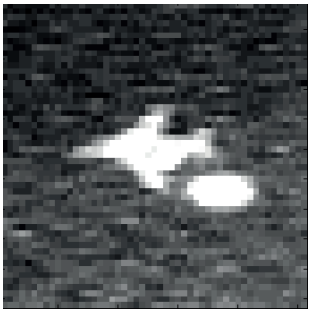

Figure 6. Close-up view of central portion of figure 3.

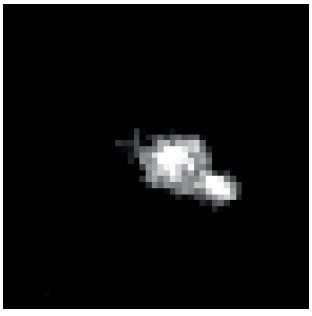

Figure 7. Close-up view of central portion of figure 5.

Peak values of the aircraft and the flare are 173 and 206 in the original image, compared to a background signal of 103. In the reconstructed image, the peak signals of the targets in the reconstructed image were 21967 for the aircraft and 22170 for the flare. The strongest

artefact signal is at a level of 12499, but is located on a ring structure that should easily be rejected. Surrounding the targets are areas with negative values.

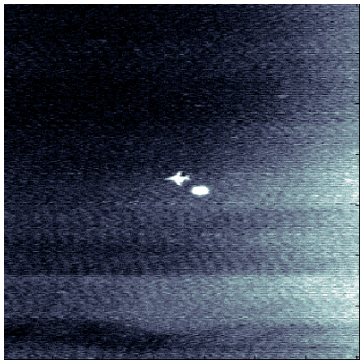

Figure 8. Original image, large separation.

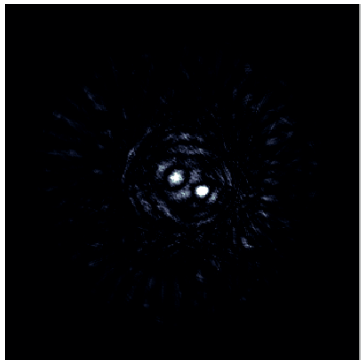

Figure 9. Reconstruction of image in figure 8. Some aliasing artefacts are present.

In figure 8, the two targets are separated sufficiently to cause aliasing, as the two objects will occasionally cross different knife-edges at the same time. In the case shown, however, the resulting aliasing shown in figure 9, is probably not severe enough to cause general problems in the image processing.

Also, the close-up views of the central portions of figures 8 and 9 seen in figures 10 and 11 show that the target positions are reasonably well maintained.

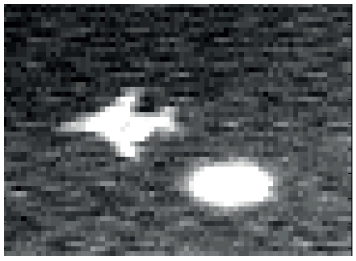

Figure 10 Close-up view of central portion of figure 8.

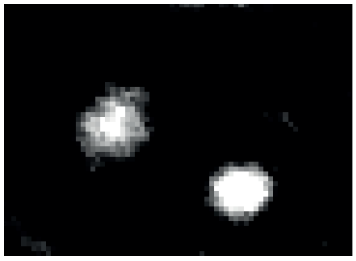

Figure 11. Close-up view of central portion of figure 9.

Figure 12 and 13 show a scenario with one aircraft and three flares, and the corresponding reconstruction. This is close to the limit of this specific system's imaging performance capability.

Figure 12. Scenario with 3 small flares.

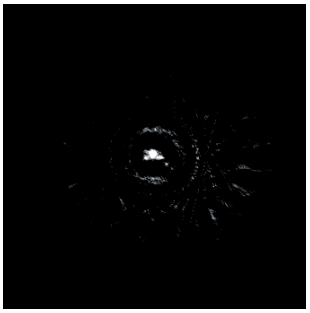

Figure 13. Reconstruction of the scenario in figure 12.

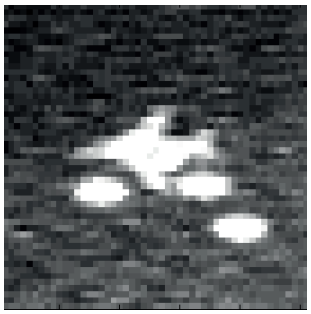

Figure 14. Close-up view of the scenario with 3 small flares.

Figure 15. Close-up view of the reconstruction of the 3 flare scenario. One flare is barely visible.

In figure 14 and 15, close-ups of the central portions of figures 12 and 13 are shown. It can be seen that the reconstruction of the rightmost flare has led to a reduction of its intensity compared to the other flares and the aircraft, although its position is still kept intact. Furthermore, an aliasing artefact can be found next to it along a line from the aircraft.

## 4. Conclusion

It has been shown that conical scan reticle systems can provide sufficient information to create an image of the field of view. Using tomographic principles, a perfect imager has been found to be theoretically feasible based on the output of a con-scan system with a single pixel detector. Simulations including several realistic aspects and limitations have shown performance in good agreement with theory. The TOSCA system can be used for imaging purposes where low cost or availability of focal plane arrays are issues.

## ACKNOWLEDGEMENTS

The author is grateful to Jonas Moen at FFI for helpful discussions, inputs and suggestions.

## REFERENCES

1. W. Herschel, “Experiments on the Refrangibility of the invisible Rays of the Sun”, *Phil. Trans. Pt. II*, **90**, 284-292 (1800).
2. R. V. Jones, “Infrared detection in British air defence, 1935-1938”, *Infrared Phys*., **1**, 153-162 (1961).
3. E. W. Kutzscher, *Proc. IRIS*, **1**, 5 (1956).

4. Federation of American Scientists web page, http://www.fas.org.
5. R. O'B. Carpenter, "Comparison of AM and FM Reticle Systems", *Appl. Opt*., **2** (3), 229-236 (1963).
6. R. G. Driggers, C. E. Halford, G. D. Boreman, "Marriage of frequency modulation reticles to focal plane arrays", *Opt. Eng*., **30**, 10 (1991) 1516-1521.
7. H. K. Hong, S. H. Han, J. S. Choi, "An improved reticle seeker using the segmented focal plane array", *Proc. SPIE* **2744** (Apr. 1996).
8. I. Kopriva, H. Szu, A Peršin, "Optical reticle trackers with the multi-source discrimination capability by using independent component analysis", *Opt. Comm*. **203** (2002) 197-211.
9. H. Szu, I. Kopriva, A Peršin, "Independent component analysis approach to resolve the multi-source limitation of the nutating rising-sun reticle based optical trackers", *Opt. Comm*. **176** (2000) 77-89.
10. J. Radon, "Über der bestimmung von Funktionen durch ihre Integralwerte langsgewisser Mannigfaltigkeiten (On the Determination of Functions From Their Integrals Along Certain Manifolds)", *Berichte Sachsische Akademie Wissenschaften*, **29**, 262-277 (1917), or same title, *Math Phys Klass*, 69, 1917 (Both texts in German).
11. F. Natterer, *The Mathematics of Computerized Tomography*, Wiley-Teubner 2001. ISBN 0898714931.
12. M. Sandborg, "Computed Tomography: Physical principles and biohazards", Report 81 ISSN 1102-1799, September 1995. See also http://huweb.hu.liu.se/inst/imv/radiofysik/pdfs/Rap81.pdf
13. A. C. Kak, M. Slaney, *Principles of Computerized Tomographic Imaging*, IEEE Press (1988) 56-57.

# Publication II

# Optimization of the Tomographic Scanning (TOSCA) Imager

**Harald Hovland**

**Proc. SPIE 6569, Acquisition, Tracking, Pointing and Laser Systems Technologies XXI , 65690I (2007)**

# Optimization of the tomographic scanning (TOSCA) imager

Harald Hovland
Norwegian Defence Research Institute (FFI), Postboks 25, N-2027 Kjeller, NORWAY.
harald.hovland@ffi.no

## ABSTRACT

The tomographic scanning (TOSCA) imager was invented by the author in 2003. Initially, the system was based on reconstructing an image from the signal of a simple single pixel, conical scan FM-reticle sensor using tomographic techniques. Although the system has been used for several decades for real-time tracking purposes, the imaging properties of the single pixel conical scan reticle system was left undiscovered until recently, although multi-target discrimination was demonstrated with multi-spectral versions of the system. The initial system presented by the author demonstrated the ability to discriminate between multiple spots in the field of view in a fairly simple scenario. Advances have been made in both theory and technology, mainly with the introduction of the nutating circular aperture in the scanning optics, and the use of Fourier transform ramp filters during reconstruction, and TOSCA is in principle found to be a perfect imaging system, only limited by practical aspects such as the number of angular scans, the spatial sampling, noise and vibration. The simplicity of the hardware, together with the rapid advances in high performance, low cost computing means the system has a potential for low-cost applications such as in expendable multi-spectral thermal imagers.

This paper will present the current state of the technology, including improvements in algorithms and reticle shapes, and look at artefacts found in various images due to different geometries, as well as ways to handle these artefacts. Several noise generating processes and their effects will be presented and illustrated with results from digital simulations. Requirements for image processing in terms of computing power are investigated, together with the potential for parallelization.

**Keywords:** Tomography, imaging system, conical scan, reticle, tracking.

## 1. INTRODUCTION

Infrared (IR) radiation has been known to man for more than two centuries, due to the discoveries of Herschel[1]. The first known suggestion for the use of this radiation in military applications is almost a century old with the proposals by Lindemann during World War I[2]. The actual application was not put in place for several decades, mainly because materials with sufficient sensitivity or speed were not available, and were not in place until well after World War II despite both Allied and German efforts[2,3]. In 1953, the first successful test of an IR seeker was made with the AIM-9 "Sidewinder" missile[4]. Simplicity was a success factor in missile design for several decades, but more complex and hostile scenarios as well as efficiency requirements have pushed the requirements for seeker performance to a point where imaging of the scene has been found advantageous, and several missile systems are now being fielded with imaging sensors, notably the new AIM-9X Sidewinder, IRIS-T, ASRAAM and Python-5. The highly sophisticated seekers in these missiles contribute to a significant portion of the total system cost, and the Tomographic Scan (TOSCA) concept is looked upon as a low-cost alternative to traditional

imaging sensors. Although the TOSCA principle is an imaging concept based on a (non-imaging) seeker design, it is not limited to missile seeker applications. As an example, expendable UAVs may be an interesting platform for hosting low cost imaging IR sensors for search and rescue, or for research purposes in various fields, such as geosciences.

Reticles in use for tracking and guidance was conceived by the Germans during World War II and almost made ready for production [5]. The first open literature description of the use of reticles for tracking was made by Clark[6], and a lot of activity in this area followed in the two following decades[5]. The use of reticle trackers enabled tracking with surprisingly simple electronics. Later, with the revolution in electronics and computing, imaging systems using either scanning or staring systems enables weapons to cope with severe jamming and complex scenarios.

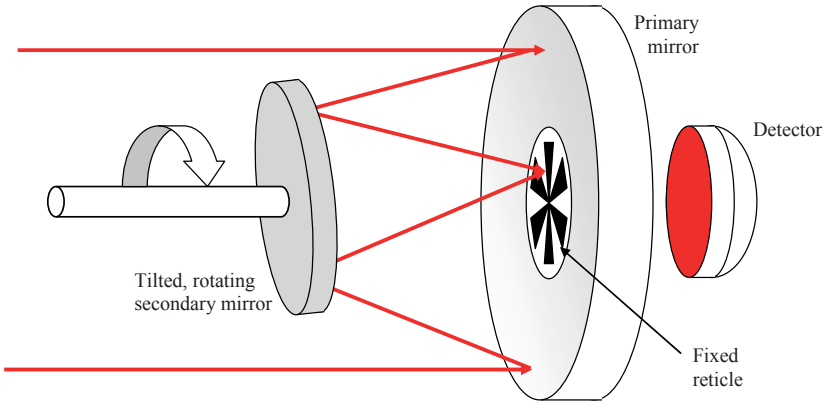


Figure 1. Sketch of the con scan reticle tracker.

The TOSCA imager uses reticle based hardware similar to that of the conical scan reticle tracker, the optics of which is shown in figure 1. Focusing optics projects the target image onto a fixed reticle consisting of transparent and non-transparent sectors. The optics is tilted and rotating, scanning the image with a circular translational movement onto the reticle. A detector placed behind the reticle detects the light that passes through the transparent reticle fields. In the basic configuration, the transparent fields of the reticle are evenly distributed around a central point, as seen in figure 2. If the target is aligned with the optical axis, a fixed frequency signal is produced, and if the target is off-axis, the resulting signal is frequency modulated according to the off-axis angle. This frequency modulation contains information about the phase and off-axis angle, and can be used to determine the target direction.

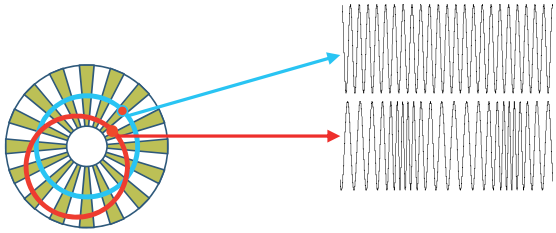

Figure 2. Illustration of the frequency modulation obtained in con-scan reticle trackers with on-axis (blue curve) and off-axis (red curve) targets.

The use of such “hot spot” tracking has been successful in air target scenarios, as the relatively homogeneous short- and mid-wave IR background contrasts with the typically high contrast aircraft targets. On the other side, simple hot spot trackers struggle with more complex and/or cluttered environments. Several proposals have been made to counter these issues. In addition to pure counter-countermeasures techniques used in missile applications, multi-pixel reticle sensors have been proposed[7,8], and independent component analysis , a sophisticated statistical method, has been applied to the output of a two-colour reticle seeker[9,10]. The drawbacks of these are, for the first proposal, a fairly complex setup, and for the second method the capability of resolving only a fairly limited number of point sources.

## 2. DEVELOPMENT OF THE TOSCA CONCEPT

### 2.1 Basic TOSCA

The TOSCA concept, invented by the author in 2003 and refined since then[11, 12] is based on the concept of multiple knife-edge scans at various angles of the target image. In a con-scan system, the target image, although moving with a circular motion, does not rotate itself, but maintains a fixed orientation. The reticle can be thought of as a set of several knife-edges across which the target image moves. This is shown in figure 3.

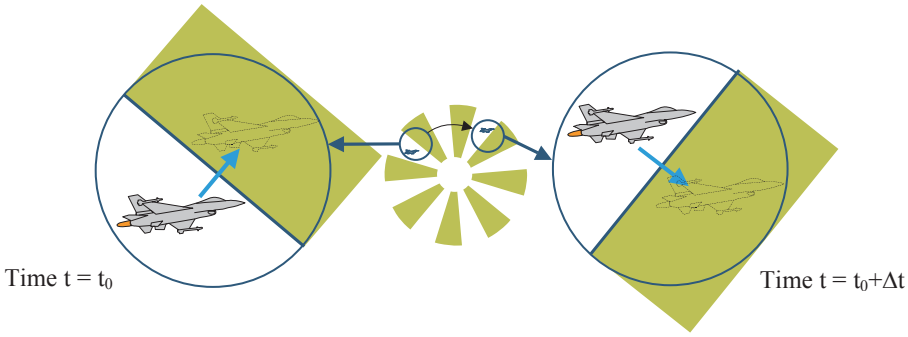


Figure 3. Knife scan of the target image in a con-scan system

If the target signature remains essentially constant during a scan, the time derivative of the signal is equivalent to the signal obtained with a corresponding line scan of the target image. Assuming the extent of the target is smaller than the knife edge, the Fourier slice theorem[13] can be used to determine that the components of the Fourier transform of this derivative signal is proportional to the components of the Fourier transform of the target along a line normal to the knife edge line direction and passing through the Fourier plane origin. With the target remaining at a constant orientation and the knife-edges appearing at regularly spaced angular orientations, the Fourier plane can be filled up with lines crossing the origin. Having filled up the Fourier space with data, an inverse transform of the data thus obtained should lead to the reconstruction of the image. Figure 4 shows an original target image, the reticle used and the first image reconstructed through simulations using this technique. Figure 5 shows a close-up of the original and the reconstruction.

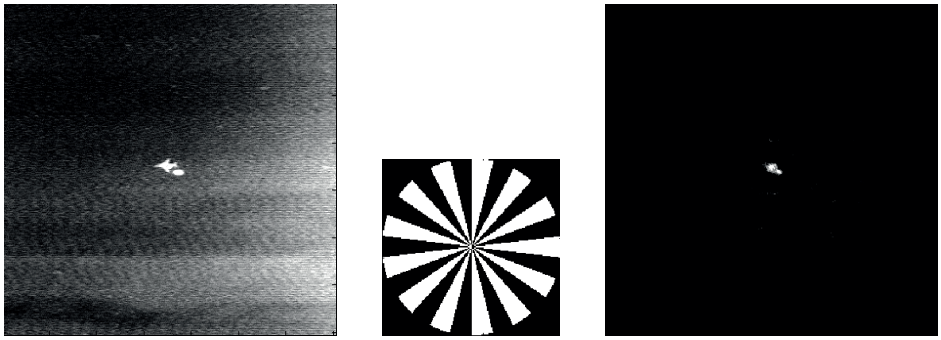

Figure 4. Original (left), reticle and first reconstructed image (right) obtained using the basic TOSCA technique.

Here, the simulated detector signal was obtained by multiplying the reticle mask point-by-point and summing up for each reticle location. The signal was then differentiated, and the reconstruction was obtained by multiplying the differentiated signal with the spatial gradient of the reticle image, located at the current reticle location. This is in tomography known as back-projection.

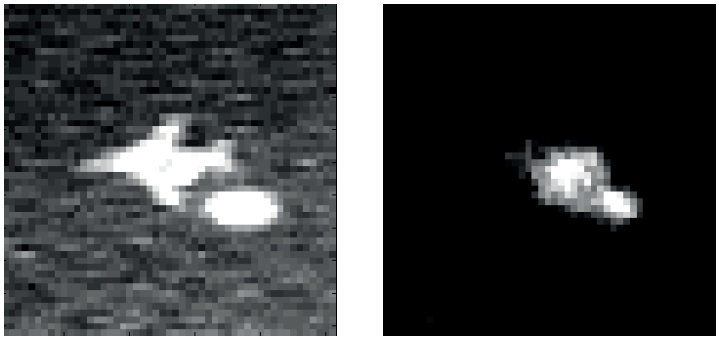

Figure 5. Close-up of the original target image (left), and the reconstructed image (right) in figure 4. The two spots are distinct and correctly located, but severely blurred

The resulting image is blurred, but it is possible to locate and distinguish the two objects. Figure 6 and 7 shows the equivalent of figure 4 and 5, but now with a slightly more complex image.

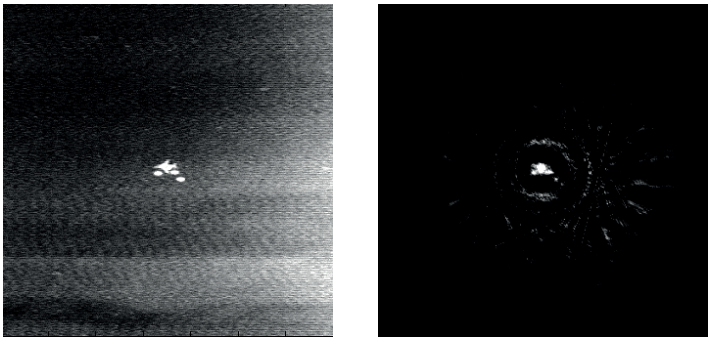

Figure 6. Slightly more complex image (left) and its reconstruction (right) obtained using the basic TOSCA technique.

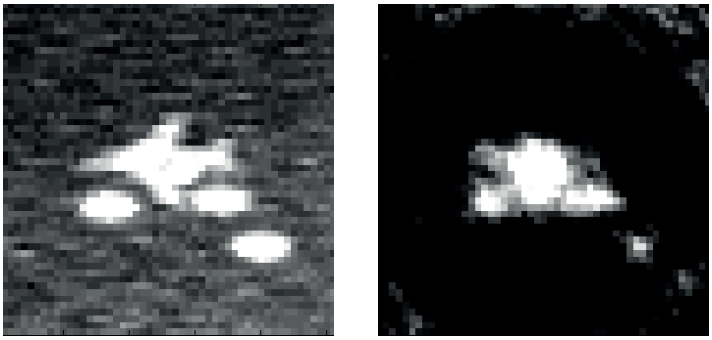

Figure 7. Close-ups of the images in figure 6.

Here, concurrent signals from different knife-edges create aliasing. The limited diameter of the reticle sector was also found to create artefacts, and the outer diameter of the reticle also creates rim artefacts.

### 2.2 Specialised TOSCA: Moving circular aperture

The next hurdle in the process was to avoid the aliasing and avoid the rim effects. This issue was solved by introducing a rotating circular aperture[12], shown in figure 8. This aperture follows the movement of the image. The apertured image now only "see" one knife-edge at a time, and the knife edge limits is not "seen" by the apertured image, the knife-edges thus appearing perfect. The resulting images are significantly better, as seen by comparing figure 6 and 9.

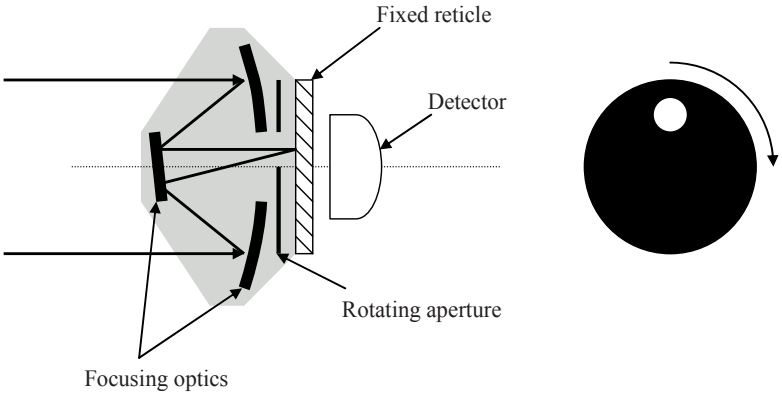


Figure 8. Schematic setup of the rotating aperture to avoid aliasing and rim effects.

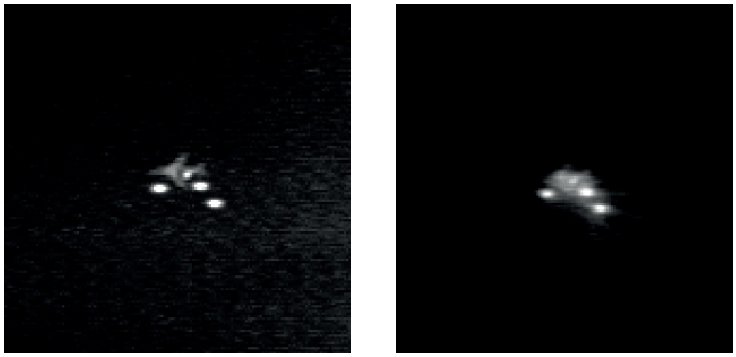

Figure 9. Original image and reconstructed image obtained by simulating TOSCA with a moving aperture.

### 2.3 Filtered back conversion

The images still appear blurred, though. The reason for this is that when making a limited number of knife-edge scans, the resulting data in Fourier space represents lines that all crosses the origin. If the rest of the Fourier plane contains zeros, we have effectively represented sectors in the Fourier space by single lines, as shown in figure 10. As the frequencies increase with the distance from the origin, and the density of lines is higher the closer one gets to the origin, this translates to a low-pass filtering effect, thus creating this blur. One way to compensate for this is to weigh the Fourier components by their distance from the origin, see figure 10 (right).

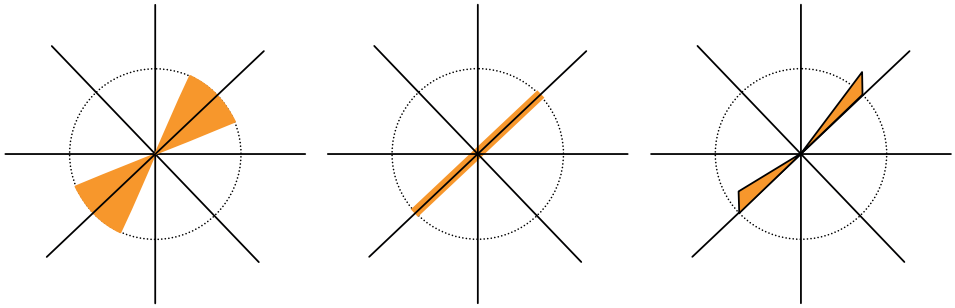

Figure 10. Filtered back projection approximation. If the number of knife-edge scans is not infinite, the ideal sampling of sectors in the Fourier plane is replaced by sampling of single lines. In order to compensate for the increased significance of the low-frequency components, the components are weighted by a factor proportional to the distance from the Fourier plane origin, a technique called filtered back-projection.

This technique, called filtered back-projection was invented by Bracewell and Riddle in 1967[12], and recreates more of the details of the image, but also produces ripple artefacts, as seen in figure 11.

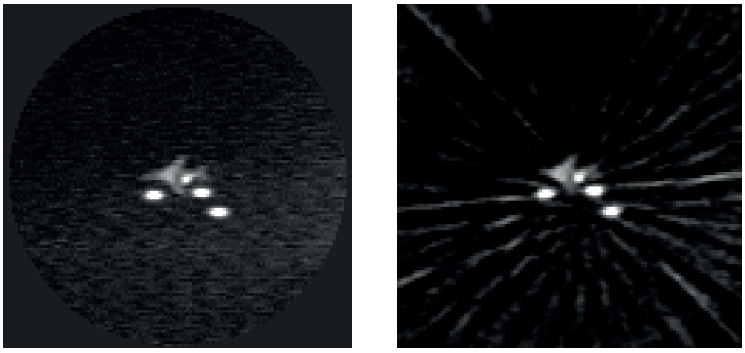

Figure 11. Original (left) reconstruction using filtered back projection TOSCA reconstruction. Fine-grained target details are now visible, at the cost of peripheral artefacts.

These ripples are peripheral to the target, and if only one small target is in the field of view, this may be acceptable. One can observe some kind of beat patterns in the reconstructed image because the different hot spots each produces ripple patterns that interfere. The main feature of these ripples is caused by the angular approximations made. Increasing the number of angle scans reduces the magnitude of these artefacts, and if the angular resolution is high enough, the artefacts disappear. The effect of this is shown in figure 12, where the reconstruction in figure 11 is repeated, but now with 60 independent knife-edges instead of 13 as in figure 11. The ripple artefacts are here removed. It can be shown that with a sufficiently high angular resolution, an exact replica of an image with discrete pixels can be reproduced.

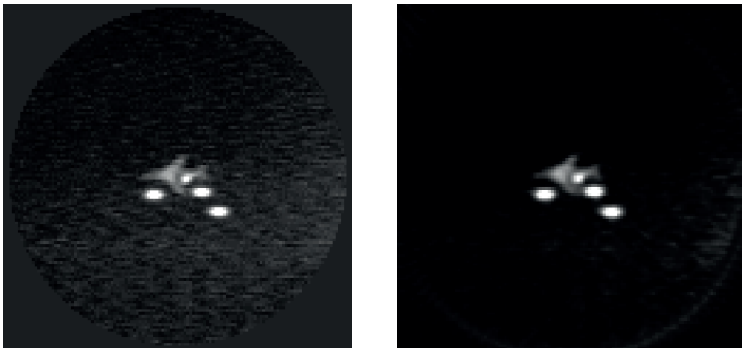

Figure 12. Original (left) reconstruction using filtered back projection TOSCA reconstruction. This reconstruction is similar to the one in figure 11, but the number of independent knife-edge scans has now been increased from 13 to 60.

Figure 13. Original “Lena” image (left) and the TOSCA reconstruction, using 60 independent knife-edge scans.

To demonstrate the more general-purpose imaging properties of the TOSCA system, figure 13 shows the 440×440 pixel original image (“Lena”) and reconstruction of the image using 60 knife-edge scans, each with 440 samples. This corresponds to a data reduction to less than 1/7 of the original. Typical for the remaining artefacts are the “losenge”-shaped noise pattern caused by a high spatial resolution and moderate angular resolution. Increasing the number of angular scans can remove these artefacts.

### 2.4 Reticle shape

The shaping of the reticle is one of the factors defining the quality of the image reconstruction. As seen earlier, aliasing can be removed if the knife-edges are located such that only one knife-edge is visible in the aperture at a time. Ideally, the knife-edges should therefore have an interspacing corresponding to the rotating circular aperture, and have a regular angular distribution. It can be noted that positive ($0 \rightarrow 100$ % transmission) and negative ($100 \rightarrow 0$ % transmission) knife-edges have equivalent functions, only resulting in a sign change of the resulting derivative signal if the target signature remains constant.

There are several main limitations for the possible system resolution. First, the resolution capability of the optics will be limited by the system spot size. The nutation circle diameter divided by the spot size diameter will give an approximate upper limit on the number of independent samples that can be acquired, and this number of samples sets an information theoretical limit to the amount of information that can be stored. For the TOSCA system, it is important to notice that this information does not have to be spread homogeneously across the entire field of view, as it is possible to trade in spatial resolution for angular resolution. A general rule for the TOSCA system is that the diameter of the nutation circle should be as large as possible, and the spot size should be as small as possible. There seems to be an apparent conflict in these two requirements, due to the fact that for a given primary diameter optics, a small spot size corresponds to a short focal length, limiting the size of the nutation circle diameter. A practical way to avoid these problems is to make use of several optical elements, possibly including multiple focal points along the optical path. This should be limited, though, due to the increased complexity and the distortions caused by imperfections in each element.

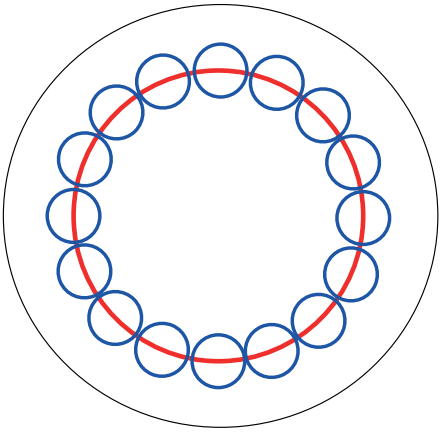

Figure 14. The maximum number of non-concurrent knife-edges is approximated by the number of circles the size of the aperture that can be put next to each other along the nutation circle circumference.

The maximum number of non-concurrent knife-edges possible can be approximated by the ratio of the circumference of the nutation circle and the aperture diameter:

$$N_{Max} \approx \frac{2\pi R_{Nutation}}{2R_{Aperture}}$$

Additionally, knife edges with angular orientations that differ by an integer multiple of 180° will produce equivalent scan signals. Using this information, it can be seen that with regular "spoked wheel" reticles such as the one in figure 15a), only half of the knife edges will produce new image information. This is a fundamental limitation for such reticles, as the number of positive knife-edges will always equal the number of negative knife-edges, thus leading to a pair number of knife-edges, and a pair number of such evenly distributed angles will always have a 180° correspondence. The maximum effective number of independent knife-edge scans we can have with this configuration is therefore:

$$N_{Eff,a} = \frac{N_{Max}}{2} \approx \frac{\pi R_{Nutation}}{2R_{Aperture}}$$

One solution is to let one pair of knife edges have parallel edges, and let the all the other have a regular angular distribution, as seen in figure 15b). This configuration optimizes the number of independent angles. The maximum effective number of independent knife-edge scans we can have with this configuration is therefore:

$$N_{Eff,a} = N_{Max} - 1 \approx \frac{\pi R_{Nutation} - R_{Aperture}}{R_{Aperture}}$$

One disadvantage is that the variation in knife edge speed is worse for the latter kind of reticle than for the regular "spoked wheel" reticle. The knife edge scan speed is approximately parabolic due to the circular scan motion. For regular "spoked wheel" reticles, the speed variations are symmetrical and similar for all the knife-edges, whereas for the reticle in figure 15 b), the variations are non-symmetrical and varies for the

different knife-edges. This can, however, be compensated for by variations in the sampling, and the variations decreases as the number of knife-edges increases.

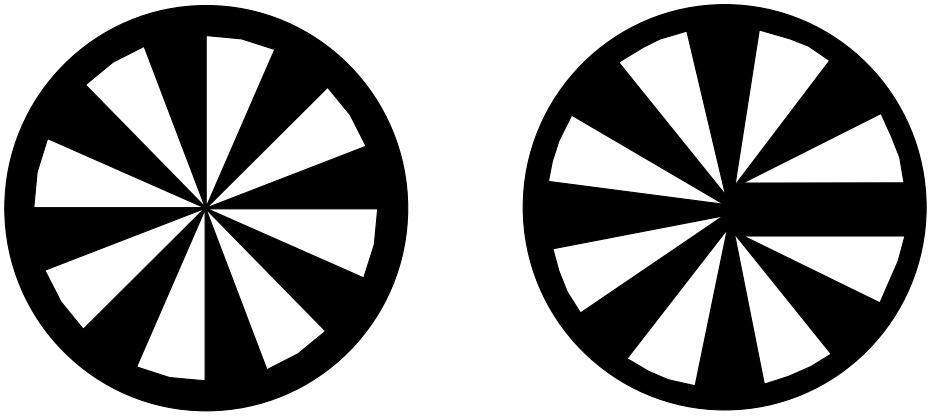

Figure 15. a) Regular "spoked wheel" reticle (left) will always have pairs of knife-edges with the parallel orientation. b) By letting two adjacent knife-edges remain parallel and the rest have evenly distributed angles (right), only one pair of knife-edges produce equivalent signals.

### 2.5 Processing requirements

With a single knife-edge present in the scene at a time, the processing is simplified. The current system takes the signal from each scan, differentiates it and takes the Fourier transform of the resulting signal for each scan. The signal thus obtained is then multiplied with the ramp filter. This process is repeated for each knife-edge scan. We now have the ramp filtered components of each line scan.

In principle, we should then only map these components into the reconstruction Fourier plane and then take the inverse Fourier transform to obtain the reconstructed image in the spatial domain. Unfortunately, things are not that simple. The problem arises as the positions of the frequency components along a line through the origin generally do not map directly onto the discrete matrix points, but somewhere in-between. Rounding off the indices in the Fourier domain gives significant errors in the spatial domain, and it is found that distributing the value of the components to nearby positions also induces artifacts, the reason being that energy representing intermediate frequency components are generally spread to all the discrete frequency components present (due to non-orthogonality), and the mapping is complex. The most promising way found until now is to take the inverse Fourier transform of each ramp filtered scan signal. For each scan signal, a matrix is then calculated where the all the matrix elements along a line normal to the scan direction have the values corresponding to the ramp-filtered spatial scan-line signal corresponding to that position. The matrix points will generally not correspond to exact points, but interpolation within the spatial domain can then be used.

Finally, all the matrices thus obtained are then added together.

We will in the analysis use *O( )*-notation to determine the processing requirements of each of the steps, summed up for the processing of an entire image reconstruction. We use the following symbols:

*n*: Number of samples per scan-line, for simplicity also assumed to be the matrix side.

*s*: Number of scan lines (independent angle scans)

The processes are the following:

1. (Potential) resampling to account for non-uniformity in the scan speed: $O(s \times n)$
2. One-dimensional Fourier transform of the scan line signals: $O(s \times n \times \log n)$
3. Ramp filtering in the Fourier domain: $O(s \times n)$
4. One-dimensional inverse Fourier transform of the ramp filtered scan line signals: $O(s \times n \times \log n)$
5. Mapping all the *s* ramp filtered scan line signal onto n × n matrices using interpolation: $O(s \times n \times n)$
6. Adding together all the scan-line matrices: $O(s \times n \times n)$

Assuming there is a good balance between the angular and the spatial resolution, we will have $s \approx n$, and the general computational load will be $O(n^3)$. Clearly, the main computational load is concentrated to the last part of the processing, but it can be noted that the processing steps are fairly simple and straightforward.

### 2.5.1 Pipelining of the signal processing

In order to reduce the latency caused by signal processing, it is interesting to find out how much can be computed as soon as possible. We will now look at the processing steps in detail, according to the list in the previous section.

- The resampling (1) can be achieved on a sample-by-sample-basis
- The Fourier transform (2), ramp multiplication (3) and inverse Fourier transform (4) can all be applied to all the samples in each scan line
- Matrix mapping of each scan line (5) will normally be done once the scan line has been processed, although it is possible to update as each data from the previous transformation (4) is calculated.
- The addition of the scan-line matrices (6) can be done as soon as each data point from the previous transformation (5) is calculated

The mathematical computation of process 1, 2, 3 and 4 is so quick and require so little storage capacity that one is not likely to do any processing for each sample, but rather do the processing once the entire scan line has been measured. This will also enable temporal calibration of the signal (using external sensors).

It can be noted that if memory use is limited, the scan line signal mappings for each angle can be stored. If the difference between the old and the new mapping for the current scan line angle is added to the reconstructed matrix, the reconstructed matrix will be updated after each scan line, in principle enabling a quicker response to events taking place.

### 2.5.2 Parallelization of the processing

There are several processes that can be parallelized. Due to the current state of processing, any parallelization, although possible, of the steps 1, 2, 3 or 4 will hardly add benefit to the system, and is therefore unlikely. There might be an interest in parallelizing the mapping and addition of steps 5 and 6, probably at a line-by-line level, although a pixel-by-pixel parallelization is also possible. It can be noted that the amount of calculations required for processing each line is constant, facilitating the parallelization. It can equally be noted that

the mapping indices and coefficients remain constant for a given angle and location, a fact that can speed up the required calculations significantly.

## 3. CONCLUSION

The tomographic scanning imager has developed from a theory of a rudimentary multi-hot-spot tracker with very limited capability to a theory of a fully capable imager, as demonstrated through simulations. The system is found to be readily scalable, with a good possibility for distributing the computing workload and reduce the latency induced by signal processing. Although promising in theory, there are still a lot of practical hurdles ahead. Future work will focus on the practical implementation of the system.

## REFERENCES


1. W Herschel, “Experiments on the Refrangibility of the invisible Rays of the Sun”, Phil. Trans. Pt. II, 90, 284-292 (1800).
2. R V Jones, “Infrared detection in British air defence, 1935-1938”, Infrared Phys., 1, 153-162 (1961).
3. E W Kutzscher, Proc. IRIS, 1, 5 (1956).
4. Federation of American Scientists web page, http://www.fas.org.
5. R D Hudson, “Infrared Systems Engineering”, p. 235, John Wiley & Sons Inc, Hoboken, NJ, USA (1969, reprinted 2006)
6. H L Clark “Sun follower for V-2 Rockets”, Electronics, 23, 71 (October 1950).
7. R. G. Driggers, C. E. Halford, G. D. Boreman, “Marriage of frequency modulation reticles to focal plane arrays”, Opt. Eng., 30, 10 (1991) 1516-1521.
8. H. K. Hong, S. H. Han, J. S. Choi, “An improved reticle seeker using the segmented focal plane array”, Proc. SPIE 2744 (Apr. 1996).
9. Kopriva, H. Szu, A Peršin, “Optical reticle trackers with the multi-source discrimination capability by using independent component analysis”, Opt. Comm. 203 (2002) 197-211.
10. H. Szu, I. Kopriva, A Peršin, “Independent component analysis approach to resolve the multi-source limitation of the nutating rising-sun reticle based optical trackers”, Opt. Comm. 176 (2000) 77-89.
11. H. Hovland, “Tomographic scanning imaging seeker”, Proc. SPIE 5430, 76-85 (2004).
12. H. Hovland, “Specialized tomographic scanning imaging seeker”, Proc. SPIE 5778, 725-731 (2005).
13. C. Kak, M. Slaney, Principles of Computerized Tomographic Imaging, IEEE Press (1988) 56-57.
14. R.H. Bracewell and A.C. Riddle, "Inversion of fan beam scans in radio astronomy," Astrophysics Journal, vol. 150, pp. 427 - 434, 1967.

# Publication III

## TOMOGRAPHIC SCANNING IMAGER

**Harald Hovland**

**Optics Express, Vol. 17 No. 4, 11371-11387 (2008)**

# Tomographic scanning imager

**Harald Hovland**

*Norwegian Defence Research Establishment (FFI), Postboks 25, NO-2027 Kjeller, Norway*
harald.hovland@ffi.no

**Abstract:** In tomographic scanning (TOSCA) imaging, light from a scene is focused onto a reticle mask using conical scan optics, and collected on a single element detector. Alternatively, one or several detectors replace the reticle. Tomographic processing techniques are then applied to the one-dimensional signal to reproduce a two-dimensional image. The TOSCA technique is presented in detail, including its mathematical foundations and some of its limitations. It is shown how TOSCA imaging can be used in a multispectral configuration, and compares well with more conventional alternatives both in simplicity and performance. Examples of image reconstruction using TOSCA techniques are shown.



**OCIS codes:** (100.3020) Image reconstruction techniques; (100.6950) Tomographic image processing; (110.0110) Imaging systems; (110.3010) Image reconstruction techniques; (110.4234) Multispectral and hyperspectral imaging; (110.6960) Tomography

## References and links

1. Federation of American Scientists web page, http://www.fas.org.
2. R. G. Driggers, C. E. Halford, G. D. Boreman, "Marriage of Frequency-Modulation Reticles to Focal Plane Arrays," Opt. Eng. **30**, 1516-1521 (1991).
3. H. K. Hong, S. H. Han, J. S. Choi, "Improved reticle seeker using the segmented focal plane array," Proc. SPIE **2744**, 433-440 (1996).
4. J. S. Sanders, R. G. Driggers, C. E. Halford, S. T. Griffin, "Imaging with Frequency-Modulated Reticles," Opt. Eng. **30**, 1720-1724 (1991).
5. M. R. Wellfare, "Two-dimensional encoding of images using discrete reticles," Proc. SPIE **1478**, 33-40 (1991).
6. J. S. Sanders, C. E. Halford, "Multispectral imaging with frequency-modulated reticles," Proc. SPIE **1478**, 52-63 (1991).
7. J. K. Bae, Y. H. Doh, D. S. Noh, S. J. Kim, "Imaging system using frequency modulation time division multiplexing hybrid reticle," Opt. Eng. **37**, 2119-2123 (1998).
8. H. H. Szu, I. Kopriva, A. Persin, "Independent component analysis approach to resolve the multi-source limitation of the nutating rising-sun reticle based optical trackers," Opt. Commun. **176**, 77-89 (2000).
9. I. Kopriva, H. Szu, A. Persin, "Optical reticle trackers with the multi-source discrimination capability by using independent component analysis," Opt. Commun. **203**, 197-211 (2002).
10. I. Kopriva, A. Persin, "Discrimination of optical sources by use of adaptive blind source separation theory," App. Opt. **38**, 1115-1126 (1999).
11. C. Jutten, J. Herault, "Blind Separation of Sources," Signal Process. **24**, 1, 1-10 (1991).
12. H. Hovland, "Tomographic scanning imaging seeker," Proc. SPIE **5430**, 76-85 (2004).
13. H. Hovland, "Specialized tomographic scanning imaging seeker," Proc. SPIE **5778**, 725-731 (2005).
14. H. Hovland, "Optimization of the tomographic scanning (TOSCA) imager," Proc. SPIE **1478**, 65690I-656910 (2007).
15. J. Radon, "Über die Bestimmung von Funktionen durch ihre Integralwerte längs gewisser Mannigfaltigkeiten" Ber. Verh. S/ichs. Akad. Wiss. Leipzig, Math.-Nat. KI. **69** (1917), 262-277
16. Hounsfield, G. N. "A method of and apparatus for examination of a body by radiation such as X- or gamma-radiation." UK Patent 1283915 (1972).
17. A. C. Kak, M. Slaney, *Principles of computerized tomographic imaging*, (IEEE Press, New York, 1988). http://www.slaney.org/pct/pct-toc.html
18. S. R. Deans, *The Radon Transform and Some of Its Application*, (Dover Publications Co., 1983)
19. F. Natterer, *The Mathematics of Computerized Tomography*, (Wiley, New York, 1986).

20. S. Quabis, R. Dorn, M. Eberler, O. Glockl, G. Leuchs, "The focus of light - theoretical calculation and experimental tomographic reconstruction," App. Phys. B-Lasers and Optics **72**, 109-113 (2001).
21. G. N. Ramachandran, A. V. Lakshminarayanan, "3-Dimensional Reconstruction from Radiographs and Electron Micrographs - Application of Convolutions Instead of Fourier Transforms," Proc. Natl. Acad. Sci. U. S. A. **68**, 2236-2240 (1971).
22. R. N. Bracewell, A. C. Riddle, "Inversion of Fan-Beam Scans in Radio Astronomy," Astrophys. J. **150**, 427-434 (1967).
23. J. Hsieh, Computed tomography principles, design, artefacts, and recent advances, (SPIE Optical Engineering Press, Bellingham, WA, 2003).
24. P. Mourolis, R. O. Green, T. G. Chrien, "Design of pushbroom imaging spectrometers for optimum recovery of spectroscopic and spatial information," Appl. Opt. **39**, 2210-2220 (2000).
25. J. B. Pendry, "Negative refraction makes a perfect lens". Phys. Rev. Lett. **85**, 3966-3969 (2000)
26. D. O. S. Melville, R. J. Blaikie, "Super-resolution imaging through a planar silver layer," Opt. Express **13**, 2127-2134 (2005)
27. N. Fang, H. Lee, C. Sun, X. Zhang "Sub–Diffraction-Limited Optical Imaging with a Silver Superlens," Science **308**, 534-537 (2005).

## 1. Introduction

Visible and infrared (IR) radiation emitted from, or reflected off objects can be used to detect, track, classify and identify these. This is done using sensors ranging from simple hot-spot trackers giving object location, to multispectral imagers that provide information about the object itself, the surrounding environment or even the climate through structural, textural, shape, radiometric, polarization and spectral information. This, together with a priori information can be used to infer indirect information such as surface temperature, emissivity or reflectivity, and even object fabrics, plant health and if or how an object is used or handled.

Unfortunately, both imaging IR sensors and multispectral imaging sensors can be costly, making their inclusion in low-cost solutions difficult. This work presents a potentially low-cost imager, bridging the gap between simple hot-spot trackers and full-fledged multispectral imagers. With a simple rotational scan, the single pixel TOSCA imager has better noise performance than a conventional single pixel scanning system, and a circular array TOSCA imager performs better than a linear array imager. The potential for remote sensing makes this a useful tool for unmanned aerial vehicles (UAV) capable of surveying wide areas. Other possibilities include sensors operating at wavelengths where focal plane arrays may be difficult or expensive to obtain, such as sensors for detecting THz or ionizing radiation.

### *1.1 Background*

Detection, tracking and identification, and later imaging have to a large extent been driven by military needs. A practical solution for autonomous tracking for missile seekers first appeared with the first successful deployment of the Air Intercept Missile (AIM-9 "Sidewinder") in 1953 [1]. For missiles, a low-cost solution is desirable. The earliest models employed spin-scan or conical-scan (con-scan) reticle seekers that are simple hot spot trackers, found suitable in relatively simple air target scenarios. Later models employing spin-scan and con-scan optics, such as the circular line scan and crossbar seekers, have addressed certain shortfalls of the former seeker models and also improved their signal to noise ratio. Nevertheless, the elegancy, simplicity and effectiveness of the reticle seeker keep the technology widespread. Figure 1 shows the con-scan reticle seeker principle together with a possible realization.

Although hot spot sensors are suitable for simple air target tracking, imagers are much more versatile, due to the capability of spatially characterizing a target or an environment

through shape, texture, orientation and/or structure. Imagers therefore have a wider application range, but their relatively high cost has restricted their use in some wavebands.

Several types of imaging or quasi-imaging systems have been proposed and deployed, including the single pixel rosette scan sensor, the linearly swept linear array sensor, and staring or step-stare focal plane array systems. Several proposals have also been made where spin-scan and con-scan reticle systems are combined with multi-element detectors to provide imaging capability. Driggers et al. [2] and Hong et al. [3] proposed spin-scan FM-reticle systems with relatively simple multi-element focal plane detectors. Several authors have proposed imaging sensors using reticles [4-7], but using an additional scanning mirror or spinning reticle. Hzu, Kopriva and Peršin proposed a detection scheme where a spectral beam-splitter and two detectors received the transmitted signal through the reticle in spin-scan [8, 9] and con-scan [10] optics. Using independent component analysis techniques [11] as well as blind source separation analysis, they were able to discriminate between several point sources.

These solutions have drawbacks requiring multiple pixel arrays, complex scanning or a limitation to very simple scenes. In previous work [12-14] however, I showed that the output signal from a con-scan reticle system with a single-element detector contain imaging information that can be extracted using tomography techniques, and gave an overview of how to reconstruct the image. This paper describes the mathematical details of this procedure, discusses problems that can occur in traditional con-scan reticle systems and shows how to avoid them. Starting with a short introduction to tomography, a mathematical description is then made of the signal extraction from an original image with a con-scan detection system, as well as the tomographic reconstruction process, illustrated by simulations. System limitations and optimization are addressed, and a comparison with conventional systems is presented.

## 2. Theory

### *2.1 Tomography*

Tomographic imaging starts with the creation of several lower dimensional projections of a scene, which are then processed and combined to reconstruct the scene. In the simplest form, a 2-dimensional scene or object is projected orthogonally onto N different 1-dimensional lines. The image can then be reconstructed using the Radon transform, named after Johann Radon who laid the theoretical foundation of tomography with his 1917 paper [15]. Work on tomography was given a boost after Hounsfield invented the CAT scanner [16]. Tomography is now used in a broad range of applications and fields, including synthetic aperture radars and sonars, astronomy, seismology, medical imaging and imaging through scattering media. Highly readable introductory books on tomography have been written by Kak and Slaney [17], and Deans [18]. The latter contains a translation from German of Radon's original paper. Natterer's book has a more stringent mathematical approach [19].

### *2.2 The con-scan reticle sensor*

The classical con-scan reticle sensor in Fig. 1(a) (schematics) and 1(c) (possible realization) mainly consists of three elements: Scanning focusing optics, a fixed reticle and a detector. The optics focuses the target scene image onto and scans it across the fixed reticle in a circular movement. The fixed reticle is a patterned mask with transmitting fields, through which the incoming light passes onto the detector to produce a signal. In the basic con-scan seeker, the target image, generally reduced to a "hot spot", is scanned across radially distributed reticle sectors. Assuming a constant scene, the signal produced from a central target is a fixed-frequency pulse train, with a stationary fundamental

(carrier) frequency. Offset targets leads to carrier frequency modulation, the modulation depth and phase giving the target position.

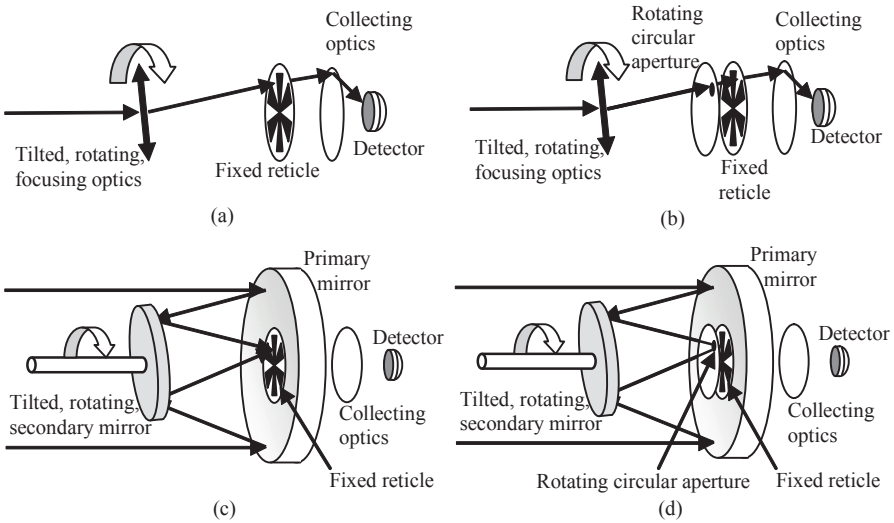


Fig. 1. Schematics and possible realization of con-scan based sensors. (a) Schematics of classical con-scan sensor. (b) Schematics of TOSCA reticle based sensor. (c) Possible realization of classical con-scan sensor. (d) Possible realization of TOSCA reticle based sensor.

## *2.3 The TOSCA principle*

The con-scan reticle system's imaging properties arises as follows: The target image movement across the reticle follows a circular yet translational path, as the target image orientation remains fixed. The knife edge transitions between reticle regions occur at well-defined orientations, as shown in Fig.2. The con-scan then becomes a sequence of knife-edge scans of the scene with a well-defined angular distribution. Tomographic reconstruction of knife-edge scans was demonstrated by Quabis et al. in another imaging application [20].

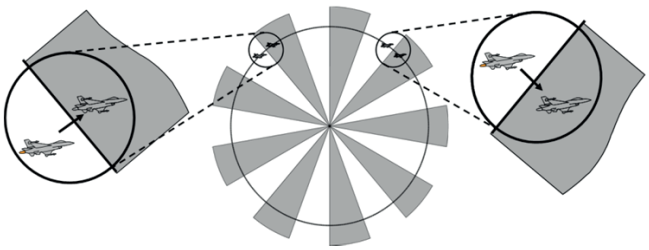

Fig. 2. TOSCA scan principle. The target orientation remains constant, whereas the knife edges have a regular angular distribution. The scan follows a circular path.

A circular aperture is added to the con-scan sensor [13]. The aperture overlaps the static reticle, but rotates with the optical axis and has an eccentricity given by it, making the reticle appear static relative to the scene image. It also limits the field of view such that only one knife edge is seen at a time, hiding the knife edge ends. The resulting system is shown in Fig. 1(b) (schematics) and 1(d) (potential realization).

## *2.4 Reconstruction in the continuous case*

We now assume a con-scan reticle system with a circular scanning aperture. We furthermore assume ideal conditions with negligible noise, ideal optics and detector, and both the aperture and the reticle to be in the image plane. We choose a coordinate system moving with the image. If the focusing optics produces an image $I(\mathbf{r},t)$, the "apertured" image becomes:

$$I_A(\mathbf{r},t) = I(\mathbf{r},t)\,A(\mathbf{r}),\; A(\mathbf{r}) = \begin{cases} 1, & \|\mathbf{r}\| \le r_0 \\ 0, & \|\mathbf{r}\| > r_0 \end{cases} \tag{1}$$

Here $\mathbf{r}$ is a image plane vector and $A(\mathbf{r})$ is the transmission of the aperture with radius $r_0$. Due to the aperture, the reticle transmission can be modeled as a sequence of unit step functions:

$$K(\mathbf{r},t,i) = \mathrm{u}\left(\mathbf{k}_i \bullet \left(\mathbf{r} - \mathbf{r}_i(t)\right)\right),\; \mathrm{u}(x) = \begin{cases} 1, & x > 0 \\ 0, & x < 0 \end{cases} \tag{2}$$

Here, $i$ denotes the knife-edge index, $\mathbf{k}_i = (\cos\theta_i, \sin\theta_i)$ denotes a unit vector normal to the knife-edge and oriented towards the transmitting region, $\mathbf{r}_i(t)$ is a point on the knife-edge, and $\mathrm{u}(x)$ is a unit step function. The signal as the scene is scanned across the knife-edges becomes:

$$S(t,i) = \iint_{\mathbf{r}\in P} I_A(\mathbf{r},t)\,K(\mathbf{r},t,i)\,d\mathbf{r} = \iint_{\mathbf{r}\in P} I_A(\mathbf{r},t)\,\mathrm{u}\left(\mathbf{k}_i \bullet \left(\mathbf{r} - \mathbf{r}_i(t)\right)\right) d\mathbf{r} \tag{3}$$

Here, $P$ is the image plane. The first order time derivative of this signal is given by:

$$\begin{aligned} \tfrac{d}{dt} S(t,i) = {} & \iint_{\mathbf{r}\in P} \left(\tfrac{d}{dt} I_A(\mathbf{r},t)\right) u\left(\mathbf{k}_i \bullet \left(\mathbf{r} - \mathbf{r}_i(t)\right)\right) d\mathbf{r} \\ & + \left[\mathbf{k}_i \bullet \left(-\tfrac{d}{dt}\mathbf{r}_i(t)\right)\right] \iint_{\mathbf{r}\in P} I_A(\mathbf{r},t)\,\delta\left(\mathbf{k}_i \bullet \left(\mathbf{r} - \mathbf{r}_i(t)\right)\right) d\mathbf{r} \end{aligned} \tag{4}$$

The first term of equation (4) is due to a scene variation, and the second part results from the knife-edge movement, as indicated in Fig. 3(a). We will here assume the scene to be time invariant and return to this assumption in the discussion. We then get:

$$\tfrac{d}{dt} S(t,i) = \left[\mathbf{k}_i \bullet \left(-\tfrac{d}{dt}\mathbf{r}_i(t)\right)\right] \iint_{\mathbf{r}\in P} I_A(\mathbf{r},t)\,\delta\left(\mathbf{k}_i \bullet \left(\mathbf{r} - \mathbf{r}_i(t)\right)\right) d\mathbf{r} \tag{5}$$

Introducing Cartesian coordinates, we define the knife-edge line $L_i$ as:

$$L_i = \left\{ \mathbf{r}_i = (x_i, y_i),\quad x_i \cos\theta_i + y_i \sin\theta_i = \int_{\tau_i}^{t} V_{C,i}(t)\,dt \right\} \tag{6}$$

Here, time is denoted by $t$, $\theta_i$ is the angle of the $i^{\text{th}}$ knife-edge normal, and $\tau_i$ is the time at which the knife-edge crosses the origin. $V_{C,i}$ is defined as the instantaneous scan speed:

$$V_{C,i}(t) = \mathbf{k}_i \bullet \left(-\tfrac{d}{dt}\mathbf{r}_i(t)\right) \tag{7}$$

Combining equations (5-7), we get:

$$\tfrac{d}{dt} S(t,i) = V_{C,i}(t) \int_{-\infty}^{\infty}\int_{-\infty}^{\infty} I_A(x,y)\,\delta\left(x\cos\theta_i + y\sin\theta_i - \int_{\tau_i}^{t} V_{C,i}(\tau)\,d\tau\right) dxdy \tag{8}$$

This corresponds to the expression of a line scan. If the scan speed component $V_{C,i}(t)$ does not change its sign during the knife-edge scan, we can define an effective scan distance $T_i$:

$$T_i(t) = \int_{\tau_i}^{t} V_{C,i}(\tau)\, d\tau \tag{9}$$

Here, $\tau_i$ is the time at which the knife edge crosses the origin. The time derivative of $T_i$ is:

$$\frac{dT_i}{dt} = V_{C,i}(t) \tag{10}$$

We now define the Radon transform of $I_A(x,y)$ as:

$$P_{\theta_i}(T) = \Re\left[I_A(x,y)\right] = \int_{-\infty}^{\infty}\int_{-\infty}^{\infty} I_A(x,y)\,\delta\left(x\cos\theta_i + y\sin\theta_i - T\right) dxdy \tag{11}$$

Combining equations (8-11), we find an important relationship between the scan distance derivative of the signal and the Radon transform of the apertured image:

$$P_{\theta_i}(T_i) = \frac{1}{dT_i}\left(\frac{dT_i}{dt}\right) P_{\theta_i}(T_i)\, dt = \frac{dS(t,i)}{dT_i} \tag{12}$$

This relationship between the extracted signal and the Radon transform of the apertured field is crucial, enabling the use of tomographic reconstruction methods from parallel beam projection. The appendix describes the image reconstruction in the continuous case.

## *2.5 Narrow slit reticle*

Physically, equation (12) is intuitive, given that the change in the signal corresponds to the signal integrated along a line at the knife-edge, and the Radon component is just such a line integral. Mathematically, the double integral in equation (5) is a rewritten line integral of the apertured image along the knife-edge. This means we can reconstruct the image scanning the scene across narrow reticle slits, the reticle transmission becoming a sequence of delta functions. Equation (2) becomes:

$$K(\boldsymbol{r}, t, i) = \delta\left(\boldsymbol{k_i} \cdot \left(\boldsymbol{r} - \boldsymbol{r_i}(t)\right)\right) \tag{13}$$

Equation (3) of the instantaneous signal is replaced by:

$$S(t,i) = \iint_{\boldsymbol{r}\in P} I_A(\boldsymbol{r},t) K(\boldsymbol{r},t,i) d\boldsymbol{r} = \iint_{\boldsymbol{r}\in P} I_A(\boldsymbol{r},t)\,\delta\left(\boldsymbol{k}_i \cdot \left(\boldsymbol{r} - \boldsymbol{r}_i(t)\right)\right) d\boldsymbol{r} \tag{14}$$

Comparing equation (14) and the development in equations (5-12), we find that:

$$P_{\theta_i}(T_i) = S(t,i) \tag{15}$$

## *2.6 Reconstruction algorithm*

We finally get the following reconstruction processing scheme in the continuous case:

1. For the knife-edge configuration, determine the scan length derivative of each knife-edge scan signal. For the narrow slit configuration, use the original signal.
2. Obtain the Fourier transform of the signal obtained in 1.
3. Multiply the frequency components in 2 by the absolute value of their frequencies.
4. Take the inverse Fourier transform of the filtered frequency components found in 3.
5. “Back project” the signal obtained in 4 along the scan lines in the image space.
6. Integrate the result in 5 for all scan angles.

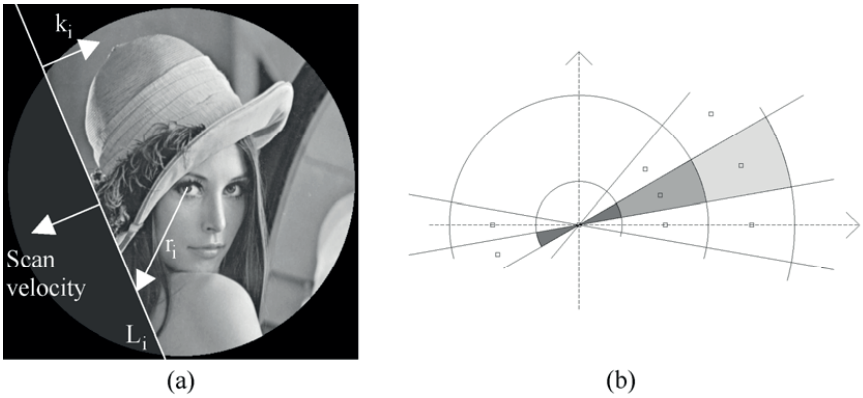


Fig. 3. Geometrical considerations. (a) Scene masked by circular aperture and knife-edge. The latter is defined by the line $L_i$ and the normal unit vector $\mathbf{k}_i$. Also indicated is $\mathbf{r}_i$, a point along $L_i$. The indicated scan velocity gives a positive scan speed and an increasing signal. The terms in equation (4) are due to scene variations and the moving knife-edge. (b) When reconstructing an image using discrete samples, the frequencies of a shaded area are represented by the value of its centre point. The sampled value is therefore multiplied by the area it represents in Fourier space. The two darkest patches are represented by the origin in the given scan. The angles are in the range $[0,\pi[$, and the frequency values include both positive and negative values.

## *2.7 Reconstruction in the discrete case*

A practical system will have a limited number of knife-edges or narrow slits, and a limited number of sample points for each angular scan. A discrete reconstruction is therefore more appropriate for a realistic approach. We must now account for several aspects:

- The Fourier transform components of the resulting samples maps onto a polar grid, which generally do not coincide with a rectangular grid. The replacement of a frequency component that falls in between the points on the rectangular grid by corresponding elements on the grid leads to a coupling to all the grid points, making this transition either inaccurate or computationally complex and time consuming.
- The sample point density in the Fourier domain is higher near the origin, but do not tend towards infinity as in the continuous case. The multiplication by the absolute value of the frequencies in the continuous case must therefore be modified at the origin, where the coefficient should equal ¼ of the frequency step length. This can be seen by considering the area of the elements surrounding each point in Fig. 3(b).
- In the continuous case, the time differentiated signal is Fourier transformed, multiplied with the absolute value of the frequency |U| and then inverse Fourier transformed. This corresponds to an aperiodic convolution. In the finite discrete case, the implementation of the fast Fourier transform (FFT) is periodic. A simple replacement of the aperiodic convolution with a periodic convolution leads to a "dishing" artefact due to an inter-period interference [17]. Zero-padding the time differentiated signal for each knife-edge scan with at least the number of original elements can remove this artefact. By making the total number of elements of each scan a power of 2, an efficient FFT algorithm can be used.
- A limited number of scan angles and low sampling density creates aliasing artefacts. The number of independent scan line angles and sample points along each

scan line should therefore satisfy the Nyquist sampling criterion. The higher tangential point density close to the origin in a polar grid means the lack of angular resolution is more pronounced at high frequencies. With a too coarse sampling, typical artefacts appear as regularly distributed rays around hot spots, or lozenge patterns in more complex images. Filtering the higher frequencies reduces these aliasing artefacts. Hsieh [23] gives examples and analyses of errors present when the Nyquist criteria are not met.

We still assume mathematically perfect components (scan mechanism, optics, detector, and sampling) in the system. The process is identical to that of the continuous case until sampling of the detected signal occurs. For a knife-edge configuration, equation (4) will be replaced by:

$$\frac{\Delta S\left(t_j,i\right)}{\Delta t}=\iint_{\mathbf{r}\in P}\frac{\Delta I_A\left(\mathbf{r},t_j\right)}{\Delta t}u\left(\mathbf{k}_i\bullet\left(\mathbf{r}-\mathbf{r}_i\left(t_j\right)\right)\right)d\mathbf{r}$$
$$+\mathbf{k}_i\bullet\left(-\frac{\Delta\mathbf{r}_i\left(t_j\right)}{\Delta t}\right)\iint_{\mathbf{r}\in P}I_A\left(\mathbf{r},t_j\right)\delta\left(\mathbf{k}_i\bullet\left(\mathbf{r}-\mathbf{r}_i\left(t_j\right)\right)\right)d\mathbf{r} \qquad (16)$$

Here, $\Delta t$ is the sampling time interval, and the other increments, annotated with a $\Delta$, correspond to the value differences between samples. The time $t$ is subscripted with a $j$ to indicate the sampling times, whereas the subscript $i$ denotes the $i^{\text{th}}$ knife-edge scan. Spatial information is still continuous, as it corresponds to the physical integration.

We define discrete samples $T_{i,j}$ of the scan distance $T_i$. The Radon transform is defined as before, but the sampled values $T_{i,j}$ replace the continuous values. Equation (12) then becomes:

$$P_{\theta_i}\left(T_{i,j}\right)=\frac{\Delta S\left(t_j,i\right)}{\Delta T_{i,j}} \qquad (17)$$

For the narrow slit configuration we retain equation (15), but replace $T_i$ and $t$ by $T_{i,j}$ and $t_j$.

We have not made any assumptions about the sampled values of $T_{i,j}$. By resampling the signals obtained in this known geometry, it is possible to find the values for constant scan distances. We may then follow the method proposed in for example [17] to do the reconstruction. This gives us the following processing scheme:

1. If necessary, resample the signal to obtain signals at equidistant scan length intervals.
2. With the knife-edge configuration, find the scan length derivative of each knife-edge scan signal. With a narrow slit configuration, use the signal obtained in 1.
3. Zero-pad the signal obtained in 2 and find the FFT of the result.
4. Create a discrete ramp filter with a length equal to the signal length in 3. The filter may be modified with a window function described in detail below.
5. Multiply the signal obtained in 4 value by value by the filter obtained in 4, and obtain the inverse FFT of the result
6. “Back project” the signal obtained in 5 along the scan lines in image space using interpolation, and sum up the result for all scan angles.

The filter applied to the signal in process steps 3-5 contains two parts:

a) The modified ramp (or RamLak) filter is given by [17,21,22]:

$$h(U)=\begin{cases}|U|, & |U|>0\\ \dfrac{\Delta U}{4}, & U=0\end{cases} \tag{18}$$

b) A windowing filter modifying the ramp filter. One alternative to equation (18) is:

$$h(U)=\begin{cases}|U|, & U_C \geq |U|>0\\ \dfrac{\Delta U}{4}, & U=0\\ 0, & |U|>U_C\end{cases} \tag{19}$$

This modification, termed a hard windowing filter, imposes a frequency limit on the system. The choice of frequency limit could be dictated by the matrix size, but could also be a lower limit. This can be used in for example over-sampling techniques.

A soft windowing filter can replace the hard windowing filter to yield better performance in noisy environments. A Hamming filter is proposed as a general purpose filter by Slaney and Kak [17], but the filter choice generally depends on the specific application.

## 3. TOSCA optimization and improvements

### *3.1 Reticle shapes*

If a circular moving aperture is used together with a reticle containing knife-edges, the maximum number of useful samples per scan angle is roughly the ratio between the optical spot size and the moving circular aperture diameter. The distance between consecutive knife edges measured along the scan circle has a lower limit determined by the aperture radius $r_{Aperture}$ and the scan circle radius $R_{Scan\ \mathrm{circle}}$. The maximum number of non-overlapping knife-edge scans is:

$$N_{Max} \leq \frac{\pi}{\arcsin\left(r_{Aperture}/R_{Scan\ circle}\right)} \tag{20}$$

The knife-edge orientations should be evenly distributed as all angles are assumed to be equally important. The radial sector distribution in Fig. 4(a) may seem logical, but is in fact not the best solution. The number of transparent and non-transparent fields is equal, making the number of knife-edge transitions between them even. Combined with the regular angular distribution, this means any knife-edge has a correspondent located diametrically opposite, the half of them thus being redundant. The number of independent knife-edge scans is thus:

$$N_{Eff,1}=\frac{N_{Max}}{2} \leq \frac{\pi}{2\arcsin\left(r_{Aperture}/R_{Scan\ circle}\right)} \tag{21}$$

A compact alternative is to use a configuration with knife-edges defined as follows:

1. The knife-edges are angularly evenly distributed, but the first and last are parallel. The angles between the $N$ subsequent (non-parallel) knife-edges is $2\pi/(N\text{-}1)$.
2. The knife-edges are separated such that the moving circular aperture located with its centre on the scan circle can be placed between two consecutive knife-edges.

We here use the term compact to indicate that this solution minimizes redundancy; hence the space wasted is minimized, leading to the smallest possible scan circle. Figure 4(b) shows a compact knife-edge reticle. Only one knife-edge pair represents a redundancy, but their crossing with the scan circle are separated slightly more than in the radial case, and we get:

$$N_{Eff,2} \le N_{Max} - 1$$

$$N_{Eff,2} < \frac{\pi}{\arcsin\left(r_{Aperture} / R_{Scan\ circle}\right)} - 1 \qquad (22)$$

Equation (22) is only an upper bound, and not the limiting function itself. With a circular scan with constant rotational speed, the effective scan speed $V_{C,i}$ varies as:

$$V_{C,i} = R_{\text{Scan circle}}\,\omega \cos\left(\omega\left(t - \tau_i\right) + \varphi_i\right) \qquad (23)$$

Here $\omega$ is the angular scan speed, and $\varphi_i$ is the angle between the scan line normal and the tangent of the scan circle where it crosses the scan line. The scan speed variation for the radial configuration is identical for all knife edges, symmetrical around each scan midpoint and approximately parabolic. The ratio between the lowest and the highest scan speed is given by:

$$V_{C,i,\min} / V_{C,i,\max} = \sqrt{1 - \left(r_{Aperture} / R_{Scan\ circle}\right)^2} \qquad (24)$$

The scan speed variation of an optimum compact knife-edge reticle is non-symmetrical and differs for each scan, the minimum ratio between the lowest and the highest scan speed being:

$$V_{C,i,\min} / V_{C,i,\max} = \sqrt{1 - \left(2r_{Aperture} / R_{Scan\ circle}\right)^2} \qquad (25)$$

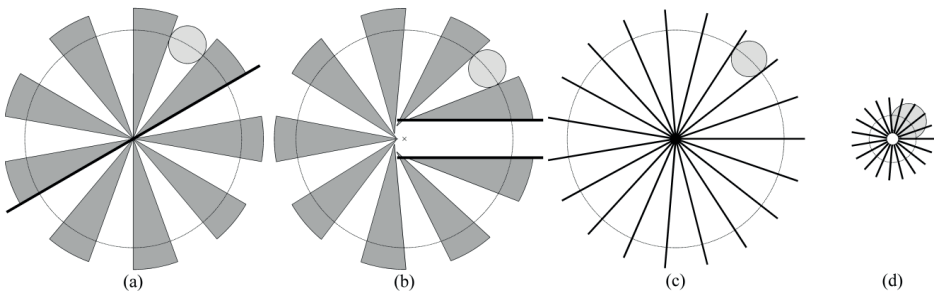


Fig. 4. Possible reticle and detector array configurations. Dark sectors are transparent regions, light grey circles show the maximum size of the moving circular aperture. Slashed circles show the scan circle. Thick lines in (a) and (b) indicates (some of the) redundancies due to parallel knife edges. (a) Radial spoke knife-edge reticle. (b) Compact knife-edge reticle. (c) Thin slit reticle configuration. (d) Circular detector array configuration, enabling a smaller scan radius.

The compact reticle version thus gives almost twice the angular resolution compared to a radial reticle for a given spot size and field of view at the price of a 4 times bigger scan speed variation. This variation, however, will be small and can be compensated for in the linear interpolation look-up tables, or the sample rate can be varied.

We now consider the narrow slit reticle, exemplified in Fig. 4(c). As parallel slits lead to redundancy, an odd number of slits is preferred. These reticles give several benefits:

1. Only the signal from a small part of the scene is integrated, reducing the required dynamic range, enabling higher radiometric resolution and reducing photon noise and the sensitivity to temporal scene variations, compared to the knife-edge configuration. The required dynamic range scales with the maximum number of pixels seen, which is proportional to the ratio between the aperture and spot diameters for the narrow slit reticle, and the ratio between the areas of the aperture and the spot for the knife-edge reticle. The photon noise levels scales with the square root of these figures. Omitting the differentiation used with knife edge scans also reduces sensitivity to high frequency detector and background noise.
2. An odd number of radial slits can be used, eliminating redundancy while maintaining a more regular scan speed. The effective number of line scans and the speed variation are given by equations (20) and (24), respectively.

### *3.2 Circular detector array configuration*

The reticle configurations have certain disadvantages. First, the collecting optics must be able to collect all the light passing through the moving circular aperture, either by bringing the light back to the rotational axis or by letting the detector follow (or even be) the moving aperture. The aperture then determines the detector diameter. Second, only one knife-edge or thin slit can be exposed through the aperture at a time, requiring a large scan radius. The scan circle perimeter is then given by the spot size, the sample number per angular scan and the number of scans. A small spot size requires optics with a small f-number. A short focal length is therefore desired, but the requirement of a large scan circle puts a lower limit to the focal length. Relay optics can be used, but adds weight, cost and complexity to the sensor. A small spot size also requires costly precision mechanics. These hurdles set aside, the required scan circle radius may still be so large that it becomes a system limiting factor. As an example, using a reticle with 129 scan lines, 129 samples per scan line and a 30 μm spot size gives a 79 mm scan circle radius.

Replacing the slit reticle by a circular array of radially oriented line detectors simplifies optics and reduces the required detector size, giving less noise and faster response. If each detector replacing a narrow slit has its own signal processing chain, several line detectors can scan the moving circular aperture simultaneously. The scan circle can then be reduced, enabling a shorter focal length and a simpler and smaller sensor. The scan radius is minimized when the (rectangular) detectors form a dense star shape as shown in Fig. 4(d), giving:

$$R'_{\text{Scan circle}} = ns\left(\frac{1}{2}+\frac{1}{2\pi}\right)=\frac{ns(\pi+1)}{2\pi} \qquad (26)$$

Here, $s$ is the detector element width, $n$ being the number of elements (of length $ns$). Compared to the smallest reticle based configuration, this corresponds to a scan circle radius reduction by a factor $n/(\pi + 1)$. With n = 129 and s = 30 μm, the scan radius is reduced to 2.6 mm. As the scan speed is proportional to the required frame rate and the scan radius, it can be reduced, along with the required detector bandwidth, leading to less detector and background noise. This increases the scan speed variations accordingly, but these variations can be accounted for in the re-sampling and/or filtering calculations. Another advantage is that a larger fill factor can be achieved, leading to a higher sensor responsivity.

The issues encountered are the same as for the narrow slit reticle configuration. An even number of detectors should be avoided due to redundancy. As an example, less information

is available from a crossbar detector (four detectors forming a cross) than the corresponding optimum configuration using three detectors.

## 4. Noise considerations

This section contains a simplified and fairly generic analysis of background and detector noise to indicate how the different TOSCA-configurations compare with other imaging solutions. Conventionally, two-dimensional images can be created in several ways: A single pixel detector scanned in 2-dimensions, linear detector array scanned linearly, and the staring 2-dimensional detector array. We will in the following analysis make several assumptions to enable the comparison to highlight general trends. These assumptions are:

- An image is represented as a matrix containing $n \times n$ pixels, and it is assumed that $n$ angular line scans are required to reconstruct the image with sufficient fidelity. The spot size and the frame rate are denoted $s$ and $F$, respectively.
- The dominating noise contribution is assumed to be either photon noise from the field of view (from now on termed just photon noise) or detector noise. The maturity of material science for detectors and optics and use of low noise electronics, shielding and cooling makes this assumption valid for a large range of systems operating in the ultraviolet, visible and infrared. Both types of noise are assumed to be proportional to the square root of both the active area and bandwidth. The active area for the photon noise is considered to be the transparent region (reticle + circular aperture) or the part of a line detector visible through the aperture.
- The photon harvesting efficiency is the average proportion of the incoming photons collected by the sensor, and is listed in table 1. The detector signal is proportional to this efficiency, and both noise types are proportional to its square root.
- As the reticle based TOSCA-configuration detector does not require imaging properties, the use of a concentrator enables a smaller detector. It is assumed (somewhat arbitrarily) that the detector area can be given approximately as $\frac{1}{4}n^2s^2$.
- The TOSCA processing contains an intrinsic noise reduction mechanism due to multiple sampling of each pixel with different angular scans. The total effect is a signal to noise improvement for both noise types by a factor $n^{1/2}$.

Mathematically, the noise reduction can be described as follows: If $N_A$ is the active area normalized by the spot size (i.e. the number of pixels covered by the active area) and $\langle\varphi\rangle$ is the expected sample noise level produced in each pixel, the expected sample noise level $\langle N_{Sample}\rangle$ in the whole active area, where the spatial noise adds incoherently, is:

$$N_{Sample} = N_A^{1/2} \left\langle \varphi \right\rangle \tag{27}$$

We denote the expected signal level from the contribution of one pixel in a sample as $\langle S_{Sample}\rangle$. The total signal contribution $\langle S\rangle$ from one pixel in a entire frame is the coherent linear addition from all the line scans, thus we get a total frame pixel signal to be:

$$\left\langle S \right\rangle = n \left\langle S_{Sample} \right\rangle \tag{28}$$

The noise on the other hand adds incoherently, giving an effective total frame pixel noise $\langle N\rangle$ to be:

$$\left\langle N \right\rangle = n^{1/2} \left\langle N_{Sample} \right\rangle \tag{29}$$

This gives an increase in the signal to noise ratio of the frame relative to that of the sample:

$$\langle S \rangle / \langle N \rangle = n^{1/2} \left\langle S_{Sample} \right\rangle / \left\langle N_{Sample} \right\rangle \qquad (30)$$

We now consider the bandwidths B required for the various TOSCA configurations. The bandwidth required for the reticle based narrow slit reticle configuration is given by:

$$B_{\text{Narrow line reticle}} = n^2 F \approx F \frac{2\pi R_{\text{Scan circle}}}{s} \qquad (31)$$

The maximum bandwidth required for the optimized circular array configuration is a function of the frame rate, scan perimeter and spot size. Using equation (20), we get:

$$B_{\text{Narrow line detector}} = F \frac{2\pi R'_{\text{Scan circle}}}{s} = F\, n(\pi + 1) \qquad (32)$$

Given the scan speed variation, bandwidth tuning during the scan can enhance performance.

Table 1 shows different factors accounting for the noise and signal levels (accumulated in a single frame) in 6 different configurations, normalized to the 2-dimensional array detector.

Table 1. General parameters governing noise performance of various detector configurations for a single image frame, normalized to the 2-dimensional array detector. A channel is here a pixel in the reconstructed image, and n denotes the array length or diameter, as well as the number of independent angular scans.

| Configuration | **2-D det. array** | Linear det. array | Single pixel det. | TOSCA knife-edge reticle | TOSCA slit reticle | TOSCA circular array |
|---|---|---|---|---|---|---|
| Photon harvesting efficiency | **1** | $n^{-1}$ | $n^{-2}$ | $n^{-1}$ | $n^{-1}$ | $(\pi+1)^{-1}$ |
| Required bandwidth | **1** | n | $n^2$ | $n^2$ | $n^2$ | $n(\pi+1)$ |
| Detector area | **1** | 1 | 1 | $¼n^2$ | $¼n^2$ | n |
| (Average) active focal plane area/channel | **1** | 1 | 1 | $½n^2$ | n | n |
| TOSCA noise reduction factor | **1** | 1 | 1 | $n^{-1/2}$ | $n^{-1/2}$ | $n^{-1/2}$ |
| Detector noise/channel | **1** | 1 | 1 | ½n | ½n | $n^{1/2}$ |
| Photon noise/channel | **1** | 1 | 1 | $2^{-1/2}n$ | $n^{1/2}$ | $n^{1/2}$ |
| S/N factor (detector noise limited) | **1** | $n^{-1}$ | $n^{-2}$ | $2n^{-2}$ | $2n^{-2}$ | $(\pi+1)^{-1}n^{-1/2}$ |
| S/N factor (photon noise limited) | **1** | $n^{-1}$ | $n^{-2}$ | $2^{1/2}n^{-2}$ | $n^{-3/2}$ | $(\pi+1)^{-1}n^{-1/2}$ |

To sum up, in terms of noise performance both TOSCA reticle versions perform better than the single pixel sensor configuration and worse than the linear array configuration. Between them, the thin slit reticle version has better background noise performance than

the knife-edge version. The TOSCA circular array configuration performs better than the linear array in terms of noise, while the 2-dimensional array performs even better.

## 5. Simulations

The algorithms used to generate the simulated detector signals as well as to reconstruct the images were implemented in Matlab® to demonstrate the concept. The source code is freely available upon request.

An original 512 by 512 pixel image "Lena", see Fig. 5(a) was filtered spatially by a 250 pixel radius circular aperture. The resulting image was then scanned by 51 independent knife-edges with regularly distributed orientations. The reconstruction is seen in Fig. 5(b). Angular artefacts are visible as a lozenge pattern in the image, but the scene is easily recognized despite a compression by 90%. Figure 5(c) shows the reconstructed image using 501 independent knife-edge orientations. Here there are no artefacts. There is no difference between this image and the image obtained using a line scan configuration in this noise-free, ideal environment.


Fig. 5. Monochrome "Lena" (a), reconstructed using 51 (b) and 501 (c) independent scans.

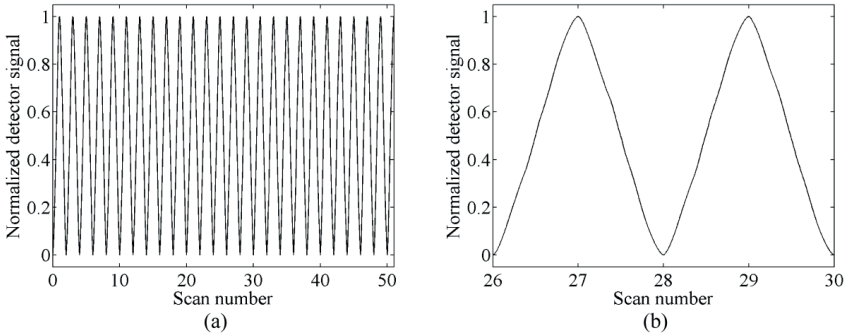


Fig. 6. Normalized detector signal from knife-edge reticle based TOSCA configuration with 51 independent scans. (a) Signal from integer frame (b) Detail from 4 angular scans.

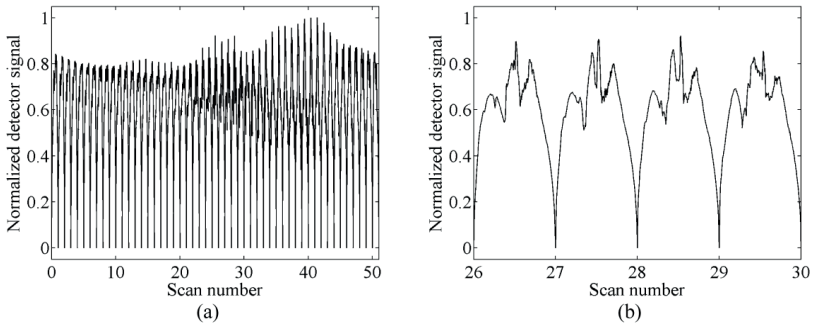


Fig. 7. Normalized detector signal from narrow-slit reticle based TOSCA configuration with 51 independent scans. (a) Signal from integer frame (b) Detail from 4 angular scans.

Figure 6 shows the detector signal from a knife-edge reticle sensor scanning the monochrome "Lena" original with 51 independent knife-edges. Figure 7 shows the corresponding signal from a narrow 51-slit reticle sensor scanning the same image. The structural differences between scans are more easily seen here. Besides the sign change in every second scan, this signal equals the scan length derivative of the signal from the knife-edge reticle sensor.

Figure 8(a) shows a colour version of "Lena". Figure 8(b) shows a reconstruction using 51 independent scan lines. The artefacts do not appear visually to distort the image to a significantly higher degree than was found for the monochrome image. As seen in Fig. 8(c), no artefacts are visible when using 501 line scans in the reconstruction, as it is a linear superposition of three artefact-free monochrome reconstructions. The lack of resolution for 51 scan lines appears to induce localized structural distortions. The feature induced distortions are less significant close to the feature. Localized features on an otherwise homogeneous background are therefore fairly well preserved, even with high compression.


Fig. 8. Colour "Lena" (a), reconstructed using 51 (b) and 501 (c) independent scans.

## 6. Discussion

### *6.1 Noise performance comparison of TOSCA imagers and alternative techniques*

As indicated in table 1, the single pixel TOSCA configuration performs better than a conventional single pixel configuration. The knife-edge reticles do not have any advantages compared to the thin slit reticles, except that it is possible to electronically

modify the number of sampling points per scan line. There might also be a manufacturability issue with very narrow slits, especially if air gaps are required.

The circular array TOSCA configuration performs better than a conventional linear array for larger array sizes ($n > 16$), at the cost of a four times larger maximum detector bandwidth. The latter is due to the increased scan distance compared to that of an ideal linear scan. The staring array imager has by far the lowest noise figure according to this simplified model. This noise analysis, however, only includes a simplistic model of the most fundamental errors. Available fill factor is not accounted for, and detector and background noise can also differ significantly from the above mentioned shot noise. As an example, low-frequency ("1/f") noise is typically a significant issue with staring systems, and can typically be a much bigger problem than normal shot noise. Non-uniformity correction is also an important issue with staring systems, and the possibility to let the system look at reference light sources during parts of the scan can significantly enhance the performance of scanning systems compared to staring arrays. Reconstruction errors can of course modify these comparisons.

Other errors and noise mechanisms can modify the picture. These include errors caused by optics and optomechanics, detectors, signal conditioning, analog to digital conversion and digital effects. Being outside the scope of this text, these issues will not be pursued.

## *6.2 Multispectral imaging*

The TOSCA imaging technique only requires a single pixel detector to create images. An interesting aspect of the system is that the image is created by temporal modulation. If the signal that comes through the reticle is sent through one or several spectral beam-splitters, it is possible to create a multispectral imager. The same can also be achieved using multispectral single-pixel detectors. Among the advantages of the TOSCA reticle configuration is that the detector only needs to collect the light, and there is therefore no need for an extremely precise detector alignment as only the fields of view are aligned and not the individual pixels. Furthermore, the signals in all the spectral bands can be sampled simultaneously and with the exact same geometry, giving the same point spread function in all spectral bands. In spectral imaging, geometrical registration between bands is crucial to avoid unphysical mixture spectra [24]. Any image blurring then creates only linear mixing between image constituents. Finally, adding extra sensor bands is relatively inexpensive.

The circular array configuration has superior noise performance compared to the corresponding reticle based system, but it is difficult to achieve multispectral detection with more than perhaps two or three detector layers (for example with the detectors stacked on top of each other), in which case the thin slit reticle configuration would be the first choice. Comparing the TOSCA system with spinning filter wheel systems is somewhat complicated. The initially high resolution and low noise gives the spinning wheel system an initial advantage. Increasing the number of bands reduces the photon harvesting efficiency reduction of the spinning wheel configuration, improving the relative TOSCA configuration performance. An increase in the number of bands might also limit the upper frame rate limit of the spinning wheel configuration.

## *6.3 Other issues*

Introducing mechanical scan mechanisms can induce vibrations, leading to wear and potential malfunction. On the other hand, the scan mechanism can, if well designed, be used to gyroscopically stabilize and even steer the sensor. The single pixel configuration features the most complex scan mechanism. The linear array detector and the TOSCA system will have a similar complexity. 2-dimensional staring arrays require no moving parts and this, together with the good noise performance currently makes the staring array

the configuration of choice for most imaging purposes. Certain aspects, however, might give an advantage to the TOSCA configurations:

- If the detector type generates too much heat in large array structures. As an example, Semiconductor material that cannot be doped to become both p- and n-type in a stable manner can only be operated in photoconduction mode. This can be the case for certain high-bandgap II-VI type and extremely low-bandgap semiconductors.
- If the radiation, such as ionizing radiation, can harm unshielded read-out electronics.
- If the detection process requires significant absorption lengths compared to detector structures or the focal depth in the image zone. This can be the case for detection with semiconductors at photon energies near or below the band gap energy, detection of very long wave infrared and THz radiation, and when using scintillation detectors.
- If the detector material supports neither embedded electronics nor flip-chip read-out.
- If feature sizes are too small for available readout electronics structures. An example of this is near-field microscopy with super-resolution using a super-lens [25-27].

A potential obstacle for the TOSCA configurations is to find sufficiently fast detector types. This is not only because of the high bandwidths required, but also the large detectors required.

## 7. Conclusion

This paper presents the tomographic scanning (TOSCA) imaging principle in detail. TOSCA is based on the extraction of imaging properties from a modified con-scan hot-spot tracker by means of computational tomography. Three versions of the TOSCA imaging configurations are presented. The configuration with the best noise performance consists of a simple nutating focusing optics which images a scene through an eccentrically rotating circular aperture. The light is then absorbed by a circular array of detectors. In the two other versions the circular detector array is replaced by a fixed reticle, collecting optics and a single element detector. The reticle contains transmitting and non-transmitting fields, either in the form of sectors or narrow slits. The light passing through the reticle is then collected by a detector.

A mathematical proof of the imaging capabilities of the system is provided, and the relationship between these imaging systems and the parallel ray tomography is demonstrated. Simulation results visualize the imaging capabilities of the system, and the consequences of limiting the angular resolution. It is shown that a system using narrow slits improves the number of useful samples for a given optical spot size and a given scan circle diameter, has better performance in terms of background noise and dynamics, and relaxes the requirements of scene stability compared to a system using knife edges to scan the scene. In terms of noise performance, a single element TOSCA sensor should be better than a single pixel imager using conventional scanning, and a TOSCA sensor with a circular detector array should be better than a linear array sensor using conventional scanning and the same number of scanning elements. The concurrent sampling and exact geometric match of all wavebands also makes the system an interesting candidate for multispectral imaging.

**Acknowledgements**

The author is very grateful to Prof. Svein Erik Hamran and Dr. Torbjørn Skauli for all the helpful discussions and able guidance they have provided.

## Appendix: Development of the continuous case reconstruction

We take the Fourier transform of the Radon transform of $I_A(x,y)$ in equation (11):

$$\begin{aligned} D_i(U) &= \mathrm{FT}\left[P_{\theta_i}(T)\right] = \frac{1}{\sqrt{2\pi}}\int_{-\infty}^{\infty} P_{\theta_i}(T)\, e^{-j2\pi UT}\, dT \\ &= \frac{1}{\sqrt{2\pi}}\int_{-\infty}^{\infty}\left(\int_{-\infty}^{\infty}\int_{-\infty}^{\infty} I_A(x,y)\,\delta(x\cos\theta_i + y\sin\theta_i - T_i)\, dxdy\right) e^{-j2\pi UT_i}\, dT_i \\ &= \frac{1}{\sqrt{2\pi}}\int_{-\infty}^{\infty}\int_{-\infty}^{\infty} I_A(x,y)\, e^{-j2\pi U(x\cos\theta_i + y\sin\theta_i)}\, dxdy \end{aligned} \quad \text{(A1)}$$

The 2-dimensional Fourier transform of $I_A(x,y)$ can be defined as:

$$F(u,v) = \mathrm{FT}\left(I_A(x,y)\right) = \frac{1}{2\pi}\int_{-\infty}^{\infty}\int_{-\infty}^{\infty} I_A(x,y)\, e^{-j2\pi(ux+vy)}\, dxdy \quad \text{(A2)}$$

From equation (A2), the expression in equation (A1) is proportional to Fourier components along the knife-edge normal:

$$D_i(U) = \sqrt{2\pi}\, F(U\cos\theta_i, U\sin\theta_i) \quad \text{(A3)}$$

Scans in opposite directions as well as scans in the same direction but with opposite knife-edge orientations give equivalent information. Switching knife-edge orientations corresponds to a change in knife-edge normal angles $\theta_i$ by $\theta_{i'} = \theta_i + \pi$, and using (A3), we have:

$$D_{i'}(U) = D_i(-U) \quad \text{(A4)}$$

Scans in opposite directions correspond to a time reversal of the initial signal, and means that the integral limits in the first line of equation (A1) should be switched. We then get:

$$D_{i'}(U) = D_i(-U) \quad \text{(A5)}$$

The signal extracted from each knife-edge scan determines the Fourier component values of the apertured image along the knife-edge normal. These lines cross the origin in Fourier space. An infinite number of knife-edge scans maps the entire Fourier space, enabling a perfect reconstruction of the image using the inverse Fourier transform. Practical systems, though, use a limited number of angular scans and samples per scan. Calculating the frequency spectrum through interpolation, followed by an inverse Fourier transformation is either inaccurate or time-consuming. A better and the most popular reconstruction technique by far is the filtered back projection technique invented by Bracewell and Riddle [22]. A modified version is presented in the following. The standard transition between polar $(U,\theta_i)$ and Cartesian $(X,Y)$ coordinates is found using the Jacobian, and we can rewrite (A3) to get:

$$D_i(U)\,U d\theta_i dU = \sqrt{2\pi}\, F(U\cos\theta_i, U\sin\theta_i)\,U d\theta_i dU = \sqrt{2\pi}\, F(X,Y)\, dXdY \quad \text{(A6)}$$

We now define $g(k)$ as an inverse Fourier transform of $D_i(U)\,|U|$:

$$g(k) = \mathrm{FT}^{-1}\left(D_i(U)|U|\right) = \frac{1}{\sqrt{2\pi}}\int_{-\infty}^{\infty} D_i(U)|U|e^{j2\pi Uk}dU \qquad \text{(A7)}$$

Using (A6) and the inverse of (A2), the reconstruction of the image is obtained as follows:

$$\begin{aligned} I_A(x,y) &= \mathrm{FT}^{-1}\left(F(X,Y)\right) \\ &= (2\pi)^{-1}\int_{-\infty}^{\infty}\int_{-\infty}^{\infty} F(X,Y)e^{j2\pi(xX+yY)}dXdY \\ &= (2\pi)^{-3/2}\int_0^{\pi}\int_0^{\infty} D_i(U)Ue^{j2\pi U\left(x\cos(\theta_i)+y\sin(\theta_i)\right)}dUd\theta_i \\ &\quad + (2\pi)^{-3/2}\int_{\pi}^{2\pi}\int_0^{\infty} D_i(U)Ue^{j2\pi U\left(x\cos(\theta_i)+y\sin(\theta_i)\right)}dUd\theta_i \end{aligned} \qquad \text{(A8)}$$

We then make a variable change in the last line, and use (A4) and (A7) to get:

$$\begin{aligned} I_A(x,y) &= (2\pi)^{-3/2}\int_0^{\pi}\int_0^{\infty} D_i(U)Ue^{j2\pi U\left(x\cos(\theta_i)+y\sin(\theta_i)\right)}dUd\theta_i \\ &\quad + (2\pi)^{-3/2}\int_0^{\pi}\int_0^{\infty} D_i(-U)Ue^{-j2\pi U\left(x\cos(\theta_i)+y\sin(\theta_i)\right)}dUd\theta_i \\ &= (2\pi)^{-3/2}\int_0^{\pi}\int_{-\infty}^{\infty}\left(D_i(U)|U|e^{j2\pi U\left(x\cos(\theta_i)+y\sin(\theta_i)\right)}\right)dUd\theta_i \\ &= (2\pi)^{-3/2}\int_0^{\pi}\int_{-\infty}^{\infty} D_i(U)|U|\left(\int_{-\infty}^{\infty}\delta(x\cos\theta_i + y\sin\theta_i - k)e^{j2\pi Uk}dk\right)dUd\theta_i \\ &= \frac{1}{2\pi}\int_0^{\pi}\int_{-\infty}^{\infty}\delta(x\cos\theta_i + y\sin\theta_i - k)g(k)dkd\theta_i \\ &= \frac{1}{2\pi}\int_0^{\pi} g(x\cos\theta_i + y\sin\theta_i)d\theta_i \end{aligned} \qquad \text{(A9)}$$

# Publication IV

# Construction and demonstration of a multi-spectral tomographic scanning imager (TOSCA)

**Harald Hovland**

**Optics Express, Vol. 21 No. 4, 4688-4702 (2013)**



The online publication also links to multimedia material.

# Construction and demonstration of a multispectral tomographic scanning imager (TOSCA)

**Harald Hovland**

*Norwegian Defence Research Establishment (FFI), Postboks 25, NO-2027 Kjeller, Norway*
harald.hovland@ffi.no

**Abstract:** This work presents the first experimental demonstrator of an imager based on a tomographic scanning (TOSCA) principle. The device described generates a stream of multispectral images of a scene or target using simple conical scan optics and a simple patterned reticle, followed by collecting optics and one or several single pixel detectors. Tomographic processing techniques are then applied to the one-dimensional signals to reproduce two-dimensional images. Various aspects of the design and construction are described, and resulting images and movies are shown.



**OCIS codes:** (070.6020) Fourier optics and signal processing; (100.6950) Tomographic image processing; (110.0110) Imaging systems; (110.3010) Image reconstruction techniques; (110.4234) Multispectral and hyperspectral imaging; (110.6960) Tomography.

## References and links

1. H. Hovland, "Tomographic scanning imager," Opt. Express **17** (14), 11371-11387 (2009).
2. H. Hovland, "Specialized tomographic scanning imaging seeker," Proc. SPIE **5778**, 725-731 (2005).
3. A. C. Kak, M. Slaney, *Principles of computerized tomographic imaging* (IEEE Press, New York, 1988). http://www.slaney.org/pct/pct-toc.html.
4. P. C. D. Hobbs, *Building Electro-Optical Systems* (John Wiley & Sons, Hoboken, NJ, 2000).
5. P. Mourolis, R. O. Green, T. G. Chrien, "Design of pushbroom imaging spectrometers for optimum recovery of spectroscopic and spatial information," Appl. Opt. **39**, 2210-2220 (2000).
6. J. Hsieh, *Computed tomography principles, design, artefacts, and recent advances* (SPIE Optical Engineering Press, Bellingham, WA, 2003).
7. R. D. Hudson, *Infrared System Engineering* (John Wiley & Sons, Hoboken, NJ, 2006).
8. E. Hecht, *Optics* (Addison-Wesley, Reading, MA, 2001).
9. J. S. Accetta, D. L. Shumaker, *The Infrared and electro-optical systems handbook*, vol. **1** (Infrared Information Analysis Centre, Ann Arbor, MI, 1993).
10. Thorlabs web pages, http://www.thorlabs.com.
11. Hamamatsu web pages, http://www.hamamatsu.com.
12. W. H. Press, "Discrete Radon transform has an exact, fast inverse and generalizes to operations other than sums along lines," Proc. Natl. Acad. Sci. U.S.A. **103** (51), 19249-19254 (2006).
13. E. J. Candès, J. Romberg, T. Tao, "Robust uncertainty principles: exact signal reconstruction from highly incomplete frequency information," IEEE Trans. Inform. Theory, **52** (2), 489-509 (2006).

## 1. Introduction

Tomographic scanning (TOSCA) imaging was presented earlier [1] as an alternative way of acquiring images using various types of radiation. It was shown that a single pixel sensor combined with a simple circular scan mechanism could produce images with better signal-to-noise ratio than achievable with classical single pixel imagers using 2-dimensional scanning.

Here, the first experimental demonstration of a working camera based on the TOSCA principle is reported. The aim of this TOSCA demonstrator is to show a practical implementation of the TOSCA imaging principle, together with artefacts that can be associated with such a system. The camera design is presented, including the signal processing necessary for the image reconstruction. Sources of noise and systematic errors are discussed. Simulations highlight important design considerations. Experimental results demonstrate that a single-pixel imager using a Si avalanche photodetector can generate useful images well above the noise floor under moderately bright and strongly varying light conditions.

## 2. TOSCA design

### *2.1 Basic principle*

The basic TOSCA sensor is illustrated in fig. 1(a). Here, thin line detectors are scanned across the scene at regularly distributed detector orientation angles, each scan producing 1-dimensional projection of the scene. The reconstruction process, described in detail in [1] and summarized in section 5.3, is similar to that used in parallel beam X-ray CAT scanners.

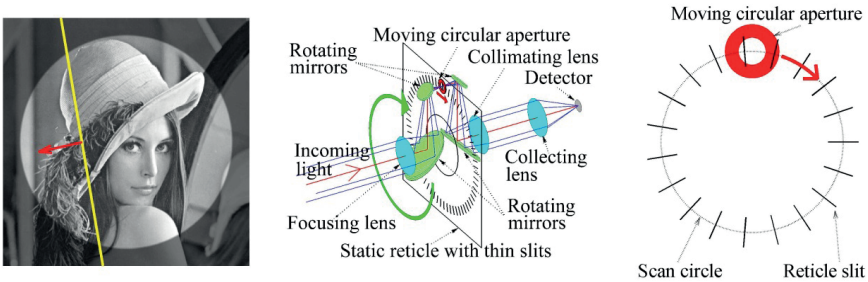


Fig. 1(a) Schematic image of a line scan: A thin line detector (yellow line) scans across the image of the scene. (b) Realization chosen in this work. The mirrors (green) and the moving circular aperture (red) rotate together as a unit around the optical axis of the incoming light. The use of a mirror pair to decenter the image on the reticle keeps the image orientation fixed relative to the reticle, making the thin slits scan the image at regular angular intervals. (c) Reticle pattern and moving aperture layout. The interior of the aperture (in red) defines the field of view, moving in a circular pattern indicated by the dashed circle. The use of an aperture enables the use of a single detector element to make all the angular scans.

The TOSCA principle can be realized in several ways. Using a circular array of line detectors is advantageous in terms of noise, size and bandwidth [2]. In the single pixel configuration, the optics could be kept stationary while the reticle is moved. Several solutions with circular translational and rotational movements were examined, but all had issues with complexity, bulkiness or other, and none are pursued further here.

The configuration chosen for this work is shown in fig. 1(b)-(c). Basically, the system consists of focusing optics to image the scene, two pairs of mirrors acting as rotating periscopes to move the optical axis sideways, through a reticle, and back to the rotational axis, where lenses collimate, then collect the light onto a detector. The image is scanned sequentially by thin transparent slits on the static reticle, oriented at regularly distributed angular intervals. A circular aperture rotating with the periscopes serves as a field stop.

Restricting the field of view (FOV) in a TOSCA system removes the effect of finite reticle slit or line detector length [2]. If a single detector is used to perform different

angular scans the aperture also separates signals from different angular scans. Circular apertures can be rotated without affecting the FOV, possibly simplifying the design.

The focusing optics requirement is somewhat relaxed compared to conventional optics: Image sharpness is only critical in the scan direction. In the direction along the slit, the signal is integrated across the FOV. The design target is thus to create a narrow line width across the reticle slit or detector line, rather than to create a small spot size.

The detector thus generates a signal corresponding to a sequence of line scans at regularly distributed scan angles. The line scan signal sequence is then amplified, digitized and processed using tomographic reconstruction algorithms to produce an image of the scene.

## *2.2 Optics, optoelectronics and A/D conversion*

The system main optomechanical components consist of the following:

1. Focusing optics, consisting of a 25.4 mm diameter, 75 mm focal length (FL) lens.
2. First rotating periscope, consisting of a 35.4 mm × 25.0 mm elliptical enhanced aluminium coated flat mirror, and a 12.7 mm diameter protected silver flat mirror.
3. Circular field stop. This 4.0 mm diameter circular aperture is made out of 0.2 mm thick Nickel/Teflon coated stainless steel.
4. The reticle is a metal coated 2.3 mm thick glass substrate (photolithography master mask) with 65 thin line segments each 6.0 mm long and 70 μm in a circular pattern. The distance from the centre to each slit centre is 43.0 mm. An odd number of slits avoids redundant information from parallel line pairs [1].
5. Second periscope, similar to the first, to realign the optical and rotational axis.
6. Collimating/collecting optics, consisting of a 30 mm diameter, 80 mm FL lens, and a 25.0 mm diameter, 20 mm FL aspheric lens.
7. Detector. The unit chosen was a Hamamatsu C5460-01 Si avalanche photodetector module, with a 3 mm diameter active area, and a 100 kHz detector bandwidth.

The camera was designed to use low-cost off-the-shelf optical components wherever possible. The optics was designed to handle wavelengths within the 400-1700 nm range, where relatively inexpensive optics and (uncooled) detectors with decent performance are available. A focal plane line width was chosen to be 70μm, determined more by moving parts in the scanning system (due to the roller bearings) than the optical limits. It was decided that a minimum 64 pixels across the reconstructed image would be sufficient for a useful general purpose image. Slaney and Kak [3] reported an equal number of angular scans and samples/scan to be suitable for general purpose imaging, and it was decided that 65 angular line scans with at least 65 samples/scan would be suitable, giving 4225 samples/frame. The 100 kHz bandwidth available with some large detectors enables ~25 Hz video rate imaging.

Combining the periscope scan mechanism with a single pixel detector means the scan circle radius is large compared to the FOV diameter on the reticle [1]. The FL of the focusing optics must equal or be larger than the sum of the scan circle radius and the optical entrance aperture diameter, as fig. 1(b) indicates. A small setup was favoured given the high rotational rate, and the approximate 4.5 mm FOV diameter on the reticle given by the line width and the initial number of lines in a scan was found suitable for 1” diameter optics.

Through simulations, a solution was found with a 43 mm scan circle radius, 1” diameter and 75 mm FL focusing optics, giving a 4.16 mm distance between scan lines. Aliasing is then avoided with a 4.0 mm aperture, giving a 53 mrad (~3°) full angle FOV. ZEMAX simulations showed the spot size would be smaller than the slit width within a 0.8 mm

focusing zone. After the reticle the light is brought back to the rotational axis using a periscope. The reticle metallization side faces the incoming beam to limit stray light.

After an 80 mm FL lens, the collimated optical beam could be split in several spectral channels using beam splitters, and then focused onto separate non-imaging detectors using lenses. The detector size is minimised to limit noise. Optimization through ZEMAX simulations showed a 20 mm FL aspheric lens to be an efficient solution. Assuming spectrally homogeneous incoming light within the 400-1700 nm range, 99 % of the light would hit the detector within a 1.35 mm diameter circle.

Even with a low-noise large-area PN detector, high capacitance (typically hundreds of pF) make them incompatible with the high bandwidth requirements (~100 kHz), even using cascode amplifiers [4] with state-of-the-art operational amplifiers. Avalanche or PIN photodiodes are a better choice, due to lower capacitance (a few pF). The Hamamatsu C5460-01 avalanche photodetector module was chosen due to bandwidth, low noise, and a fully characterized amplifier design with a suitable gain, reducing risk and development time.

The analogue to digital conversion prior to digital signal processing and display was done using a National Instruments NI PCI-6123 16-bit, 500 kS/s/ch simultaneously sampling card.

The sample rate can easily be modified in this setup, but we will in the following assume 119 samples/scan, higher than the originally 65 indicated. This makes the sample scan step versus slit width ratio near integer. An integer ratio means the resulting signal intensity due to a point source will be independent of its position. The oversampling can reduce quantization and aliasing errors, if the resulting signal is appropriately filtered.

## 3. Experimental set-up

Compared to the system described in section 2.2, the sampling rate of the A/D card was set to 200 kHz for each channel, with subsequent resampling as described in the following. The frame rate was ~25 Hz in all experiments.

The rotating optical unit base is a single piece of machined aluminium mounted with roller bearings, as seen in fig. 2(a). The mirrors forming the two periscopes are first surface mirrors, mounted with the reflecting surfaces towards the aluminium unit for better tolerances. The focusing and collimating optics are mounted in sideways adjustable holders using nylon-tipped set screws, and longitudinally adjusted with shims. The circular aperture was aligned with, and glued to the rotating unit using a jig, the soft coating facing the reticle.

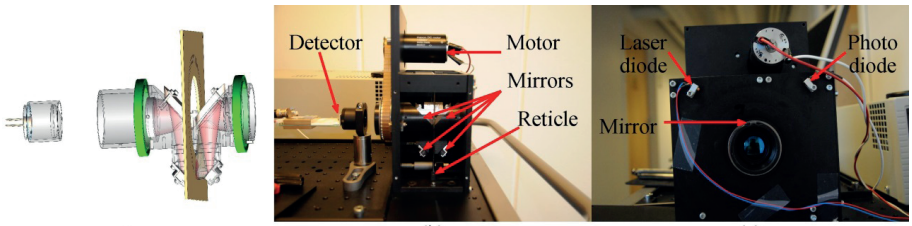


Fig. 2(a) Semi-transparent view of the rotating optics, reticle and detector unit. (b) Experimental TOSCA setup. The motor (top) drives the scan unit (centre) using a belt drive. The lens/ detector/amplifier assembly (left) is mounted on a post holder. The scan head and detector was enclosed to avoid stray light. (c) Laser based tachometer. A laser (top left, connected by red/ blue leads) was pointed at a mirror, mounted on top of the rotating unit. At each turn, the ref-lected light hit a photodiode, creating a sharp flank pulse used as an absolute angular reference.

Optics alignment was achieved by adjusting the focusing lens to minimize the aperture border circular movement as seen from several meters in front of the optics, the aperture back illuminated without the reticle. The reticle was first mounted in a plane between three adjustment screws with opposing springs, and was then aligned sideways by looking from the collimator side, where the slits should bypass the aperture by equal amounts in all orientations. The collimating optics was aligned with a bright light source several meters in front of the rotating optics (with the reticle mounted), adjusting the collimating lens sideways until the source appeared stable, as seen through the collimator.

Counterweights were used to minimize vibrations due to first and second order moments. The rotating unit was driven via a belt drive by a DC motor, as shown in fig. 2(b). The motor was powered by a 13.7 V, 7.0 A regulated power supply.

A 5 mm square mirror was fixed to the side of one of the ends of the rotating unit, facing outwards. Light from a collimated laser source hitting the mirror when the latter faced upwards was collected by a simple photodiode with integrated collector optics, as shown in fig. 2(c). The rising flank of the electrical pulse at each revolution was used as an absolute position trigger. Recording this gave a relative jitter of ±0.25 % of the roundtrip time.

This jitter level makes it necessary to resample the detected signal, as simulations (section 5.5) show that the image starts to deteriorate even with single sample shifts, making the trigger mechanism unsuitable as a sole reference. If the detector signal is significant at all time, the trigger can still be combined with the detector signal to get a useful reference:

The camera is sealed to avoid stray light. Without overlap between the rotating aperture and the reticle slits, little light reaches the detector. As the aperture starts to sweep across a slit, the signal starts increasing. The signal normally increases, and then decreases until the aperture and slit no longer overlap, as shown in fig. 3(a). Noise can make it difficult to determine the exact minimum signal position. A running (cosine segment) smoothing filter suppressed the signal noise fairly well, enabling position location. The minima sample positions were smoothed out to reduce time step quantisation errors. These sample minima correspond to regularly distributed angular orientations of the rotating unit. The signal was then resampled using linear interpolation to get estimated constant angle step sample points. The laser pulse position then determined absolute angular orientation.

With a relatively tight drive belt, a multi-component oscillation was observed in the minimum signal time intervals. The biggest components corresponded to the motor rotation frequency and the optical unit rotation frequency, likely caused by cogwheel eccentricity and tilted roller bearings/fixtures. Loosening the belt reduced oscillations, removing motor cogwheel contributions. Fig. 3(b) shows the resulting frequency components.

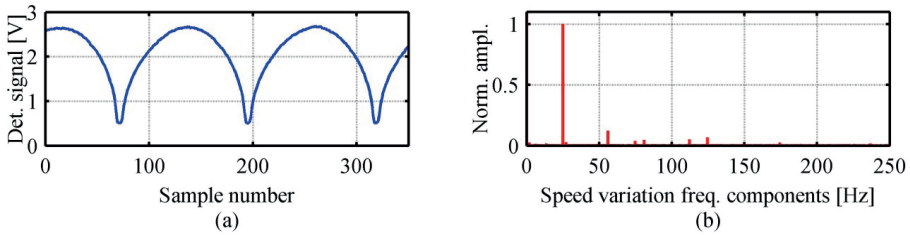


Fig. 3(a) Signal recorded from the Hamamatsu detector module (inverted). Minimum signal occurs when reticle slit and aperture do not overlap. (b) Rotation frequency components, measured by intervals between detector signal minima. The 25 Hz peak is the optics spin frequency.

## 4. Experimental imaging results

### *4.1 Single point reconstruction*

Single point sources, homogeneous and complex scenes were used to characterize the system. Recordings of single points were made at several FOV locations, using a 2 mm diameter spot from a 1.3 mW, 543 nm HeNe-laser reflecting off white paper, located 5.12 m from the camera. The spot featured some visible speckle. The paper was illuminated by an opposing white wall illuminated by sunshine through windows. An illumination level of 320 lux ±5% was measured using a lux meter in front of the paper, indicating the background was fairly homogeneous, and much dimmer than the reflected laser spot. The paper was estimated to diffusely reflect ~90% of the incoming light, filling the FOV. By estimating the TOSCA camera spectral responsivity bandwidth to be ~4 times larger than that of the luxmeter, and that the reflected sunlight is relatively constant over the detector spectral range, rough calculations indicates that the radiant power from the reflected laser spot should be ~1% the radiant power of the remaining reflected light from the whole 30 cm diameter circular disc seen by the camera. The 0.9% value determined from fig 4(a) is in good agreement with this estimate. The laser spot was moved to produce different single point reconstructions.

Reconstructions of centred and de-centred spots are shown in fig. 4(b) and (c). In both cases, the reconstructions exhibit a peak centred at the laser spot, surrounded by a ring of slight unstructured “noise”, then a ring with radial modulation, a region with slightly less structured modulation pattern, and then again a new modulation pattern, resembling fig. 8(b) and (c) in the simulation section, except that the simulated main lobes are thicker.

Temporal noise figures were determined by illuminating the paper as before, but with higher intensity. Lux measurements now gave reading of 2000 lux ±10%. We now assume the spectral distribution to be similar to that measured during the point reconstructions. Measurements with the laser spot, gave ratios consistent with previous measurements. Temporal statistics of each pixel in a 101 frame recorded reconstruction of the homogeneous background were made. The temporal mean and standard deviation values, a histogram of values within the field stop are shown in fig. 5(a)-(c). The noise is strong at the aperture border. We now focus on the region inside the border. Fig. 5(d) shows the relative noise level as a function of distance (in pixel units) from the image centre. The noise level error bars shorten with eccentricity due to the higher number of pixels considered.

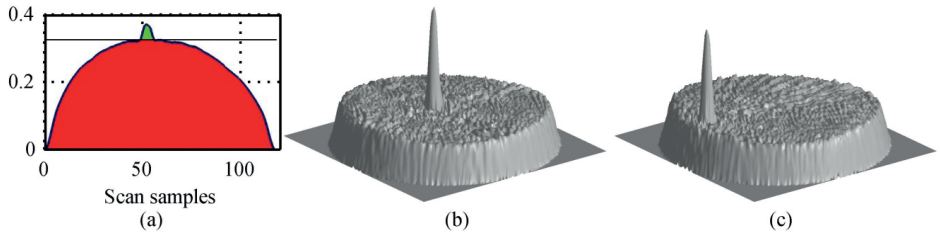


Fig. 4(a) Laser spot (green) and background illumination (red) contributions in a measured scan signal. The ratio of these areas is 0.009, close to the predicted 1%. Reconstruction of (b) centred and (c) de-centred laser spot reflected off a homogeneous background.

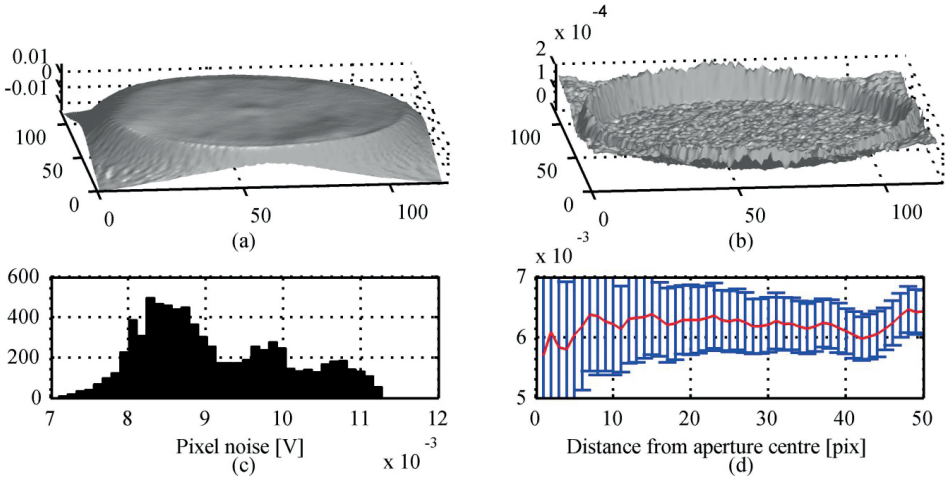


Fig. 5. Temporal statistics of 101 subsequent reconstructed frames: (a) Mean value. (b) Temporal standard deviation. (c) Histogram. Only pixels within a 50 pixel radius are accounted for to minimise the effect of the field stop. (d) Relative noise level (red curve) as a function of distance to the reconstructed image centre, in reconstruction pixel units.

To assess the photoelectron number generated per frame, we start by estimating the number of photons arriving at the camera entrance aperture. The reflection of the 1.3 mW, 543 nm HeNe laser corresponded to 0.9% of the reflected output when the copying paper source was illuminated with 320 lux light. With a diffuse reflectance of 0.9, the 2000 lux figure is equivalent to 0.81 W diffusely radiated at 543 nm. Including the optics transmission of 0.7, the 22 mm entrance aperture optics at a 5.12 m distance captures an equivalent 2.6 µW from the scene. The FOV pixels are exposed for 10 µs per angular scan. 65 scans per frame gives a 0.65 ms total exposure time per frame, with a total of 1.8 nJ arriving on the detector. These are distributed onto the $10.5\times10^3$ pixels within the FOV. The detector responsivity at 543 nm being 0.2 A/W (without the avalanche gain), each pixel receives $1.34\times10^{-13}$ C, or $2.1\times10^5$ photoelectrons per pixel, resulting in $4.6\times10^2$ centre pixel photon noise. This noise is incoherently added to the $1.2\times10^3$ photoelectrons of detector noise calculated in section 5.2, giving a total noise of $1.3\times10^3$ photoelectrons. The resulting relative noise level then becomes $6.2\times10^{-3}$, in good agreement with fig. 5(d). The theory presented in section 5.2 indicates a 20% reduction in photon noise at the border relative to the centre noise. The relative rim noise level would then be $6.0\times10^{-3}$ if the FOV border effect is ignored. This is consistent with the trend of fig. 5(d), but the results are inconclusive, given the data uncertainty.

### *4.2 Multispectral TOSCA imaging*

To demonstrate multispectral operation, a Thorlabs FD2G green interference filter was used as a 45° spectral beam-splitter after the collimator lens. The two resulting light beams were then collected using two lens/detector pairs. The modified setup is shown in fig. 6(a).

Operation was similar to before. The images from the 'non-green' and 'green' channels are shown in fig. 6(b) and (c), respectively, and a merged two-channel image is shown in (d). In this image, the black/white pattern is of particular interest. Both 'non-green' and 'green' dominance is visible elsewhere, but does not appear in any black/white transition. Colour artefacts can often be visible at such transitions in traditional multispectral cameras with spectral misalignment, and can cause problems when looking for objects with a specific spectral signature, particularly when looking at sub-pixel targets on a

homogeneous background [5]. In the TOSCA camera this problem is different, as the image geometry is defined by the narrow reticle slits and the aperture, which are common for all spectral components. Similar artefacts might instead appear if the detector/amplifier chains of different spectral channels have different temporal filter or non-linear characteristics. In addition, artefacts due to the point spread function could also affect this issue, as the colour of a strong intensity peak would create surrounding ripples.

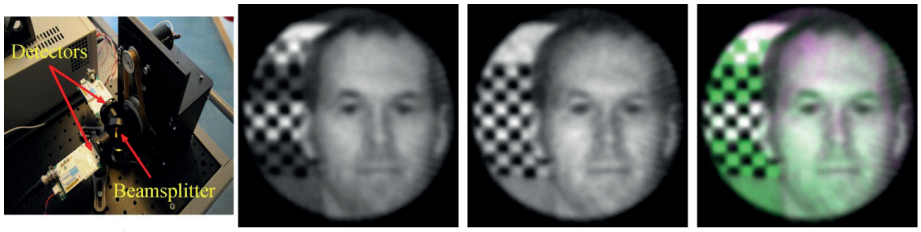


Fig. 6(a) Multispectral TOSCA setup. A spectral interference filter splits the beam in two. Each beam is detected with a lens/detector pair. (b)-(d) Author image with green/white, green/ black and white/black checkerboard patterns in (b) 'non-green' channel, (c) 'green' channel and (d) a colour-coded combined image. The white/black checkerboard pattern transition colour purity is due to perfect alignment between channels, inherent in the TOSCA system.

## 5. Design considerations

### *5.1 Sources of noise and systematic error*

In a TOSCA system, artefacts can occur in the image if the scene is undersampled [3], and an application-dependent tradeoff can be made between the image quality and the requirements on the camera hardware. To completely avoid aliasing, the Nyquist criterion must be met at the aperture periphery. The highest spatial frequency $k_{max}$ supported due to angular scan limitations is given by the number of angular scans $N$ and the aperture diameter $D$:

$$k_{\max} > N/(\pi D) \qquad (1)$$

In the worst-case, the system presented here supports spatial frequencies corresponding to ~20 line pairs across the aperture diameter due to the limited number of angular scans. If the region of interest is a small structure on a homogeneous background, the spatial frequencies supported will be higher, typically limited to the sampling density, and as a bonus, the artefacts are separated from the target.

Photon noise arises due to arrival statistics. The TOSCA measurement principle leads to a spatial smoothing of this noise [1].

Errors are induced by the scanning, for example due to rapidly moving or varying objects. Optical and optomechanical errors and noise sources due to imperfections and limitations in the optics and the scan mechanism also limit the system performance. The lack of angular resolution was covered in [1], and the general problem of undersampling in tomographic reconstruction is treated in [7]. Other errors arise due to detector response imperfections such as non-linearity, non-homogeneous frequency response and calibration errors, analogue signal conditioning and the digital-to-analogue conversion process, together with noise arising from the corresponding components. The TOSCA measurement principle also smoothes out detector noise spatially [1]. Finally, imperfections in the digital filtering and reconstruction methods can also contribute to image degradation.

Many of these effects are well described in textbooks [6-9]. We will here focus on those specific to the TOSCA configurations, namely geometrical and timing errors. Some of these errors are also explained further and exemplified through simulations in section 5.5.

With a misaligned circular aperture, the FOV moves in a small circle in the scene, and only parts of the angular spectrum of the peripheral structures are reproduced, leading to essentially peripheral artefacts. The misalignment is characterized by a revolving vector.

Reticle slits may be misaligned laterally or angularly. A translational reticle slit dislocation represents approximately a co-ordinate system shift. Unless two reticle slits are visible jointly through the circular aperture, the equivalent of a time shift can compensate such errors; using a sufficiently small aperture will avoid such double exposure. An overall rotational error implies an equal offset error for all lines, plus a common rotational error as the sampling and reconstruction lines are misaligned. Line scan signals due to a point will be shifted by a specific distance. The point spread function then becomes a circle, turning points into circles, and lines into line pairs. Edge artefacts will also occur. This rotational error is similar to an overall timing error, with the exception of the overall rotation.

## *5.2 Photon budget*

Prior to construction, a theoretical analysis was made using real component data to see if the system can produce signals beyond noise. The reference target is a 25 % reflectance horizontal Lambertian gray body, illuminated by the sun in zenith through a 1976 U.S. standard atmosphere. Fig. 7(a) shows the resulting target spectral radiant exitance $M_\lambda$ from published LOWTRAN 7 data [9]. A short scene-camera-distance is assumed, and the resulting atmospheric effects are ignored. Internal optics transmission/reflection losses are accounted for.

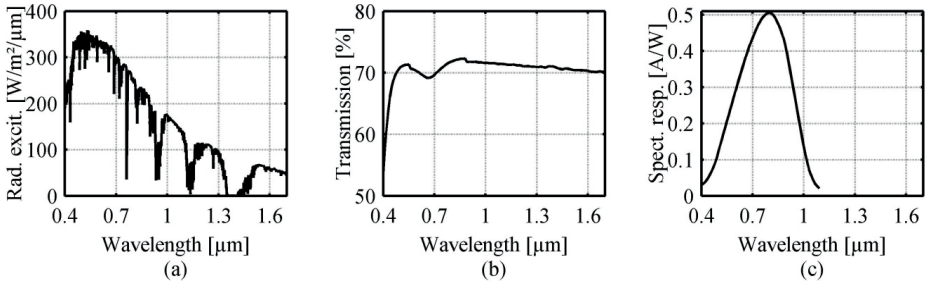


Fig. 7(a) Spectral radiant exitance from a 25% diffusely reflecting, horizontal test target in the 1976 U.S. standard atmosphere [9] with an air mass index $m_a$ = 1.0, the sun being in zenith. (b) Optics transmission for light passing through the reticle slit in the proposed system. (c) Spectral responsivity of the Hamamatsu C5460-01 detector, not including the avalanche gain.

The optics consists of 3 lenses, 4 mirrors and one reticle. With BK-7N surface transmission data and protected silver coating mirror reflectance data found on Thorlabs' web sites [10], a ~70% transmission is found in fig. 7(b). The Hamamatsu C5460-01 detector spectral responsivity [11] is shown in fig. 7(c). Diffraction losses are being ignored as the reticle slit width is much larger than the wavelength. Besides the ~30 % optical loss, all light passing through the entrance aperture, the rotating aperture and the reticle are assumed to hit the detector. Consider an image pixel as a 70 µm side square in the reticle plane. With the 75 mm FL, the image pixel solid angle is $\Omega_{Px} = 8{,}7\times10^{-7}$ sr. A Lambertian target filling the pixel illuminates the entrance aperture with spectral intensity:

$$P_{Px,\lambda} = M_\lambda A_{Ap} \Omega_{Px} / \pi \qquad (2)$$

With a 25 Hz frame rate, 65 slits and 119 samples/scan, the sample interval is $\Delta t$ = 5.1 µs. The number of photoelectrons $\langle S_{e,sample} \rangle$ generated by light incident on a pixel-size area of the reticle slit is:

$$\left\langle S_{e,sample} \right\rangle = e^{-1} \Delta t \int P_{Px,\lambda} R_\lambda \tau_\lambda d\lambda = (\pi e)^{-1} \Delta t A_{Ap} \Omega_{Px} \int M_\lambda R_\lambda \tau_\lambda d\lambda = 9.4 \times 10^4, \quad (3)$$

with the electron charge $e$, the detector spectral responsivity $R_\lambda$ and the optical spectral transmission $\tau_\lambda$. The total number of photoelectrons per image pixel is the sum from each angular scan:

$$\left\langle S_{e,frame} \right\rangle = N \left\langle S_{e,sample} \right\rangle = 6.2 \times 10^6 \quad (4)$$

To determine the actual "photon noise" of the photoelectron signal, some assumptions must be made. Only the FOV contributes to the photon noise. The detector sees an entire line within the circular aperture, meaning "hot spots" can give significant noise contributions to low intensity areas. Even homogeneous scenes produce uneven spatial noise distributions: Central pixels get more noise since the average line segment size, defined by the slit and the circular aperture, decreases away from the centre (where the line length is the full diameter for all angles). The centre noise level is ~1.25 times that at the rim, with an asymptotic value of $(\pi/2)^{1/2}$ in the limit of narrow scan lines relative to the FOV diameter. If the reference target fills the FOV, the centre pixel photon noise level $\langle N_{p,frame} \rangle$, given as the square root of the total number of photoelectrons collected in the central pixel, is therefore a conservative estimate:

$$\left\langle N_{p,frame} \right\rangle = \sqrt{\left\langle S_{e,frame} \right\rangle} = 2.5 \times 10^3 \quad (5)$$

The Hamamatsu C5460-01 noise equivalent power (*NEP*) is $2 \times 10^{-14}$ W/√Hz, at the peak responsivity $R_{Max}$ = 0.5 A/W. The detector sample noise level $N_{d,sample}$ in photoelectrons is:

$$N_{d,sample} = \frac{R_{Max} NEP \sqrt{\Delta t}}{e} = 1.4 \times 10^2 \quad (6)$$

The detector noise can be expressed as an equivalent number of frame pixel photoelectrons by incoherent addition of the 65 angular scans:

$$\left\langle N_{d,frame} \right\rangle = \sqrt{N} \left\langle N_{d,sample} \right\rangle = 1.2 \times 10^3 \quad (7)$$

This is about half of the photon noise and leads to a degradation of the signal-to-noise ratio by about 12 %, compared to photon noise alone. The chosen example is thus close to the detector noise floor. However, as can be seen in the simulations in section 5.6, spatial averaging makes image features visible at even lower signal levels.

Using the initial reference target and introducing beam splitters and multiple detectors, the detector noise per channel is unchanged. The signal is split between the detectors, and the photon noise per channel is therefore reduced. If the signal is equally split in 4 channels, the photon noise per channel is halved, equalling the detector module noise. The signal-to-noise ratio is then $9.1 \times 10^2$. Exploiting the range beyond the Si spectral band using InGaAs detectors do not affect the Si detector performance, but such detectors are typically noisier.

At the given light levels, the sensor is still photon noise limited, but for lower light levels the detector noise becomes the dominant source, and the signal to noise ratios then scales with the signal level. If the reference target is observed during overcast weather, the

light level could be reduced by some 2 orders of magnitude, making detector noise significant.

## *5.3 TOSCA simulation tool*

A simulation tool was developed in MATLAB to aid the design of an experimental realization. The software is available from the author upon request. The tool consists of:

- Scene generation. An arbitrary image is used as input, and photon shot noise is simulated.
- Circular aperture generation and superposition on the image. Parameters specify the aperture/scene misalignment, inducing a circular aperture movement relative to the scene.
- Reticle generation. Specifies the physical reticle shape, including overall offset and misalignment, as well as shape, position and orientation errors of each individual slit.
- Scan movement generation. Includes rotational errors and individual sample errors.
- Detection process, including detector/electronics noise generation and timing jitter.
- Reconstruction process using filtered back projection.

The filtered back projection is described in detail in [1]. Briefly, the steps are as follows:

- Each angular scan is zero-padded and FFT'ed to replace the discrete Fourier transform.
- The FFT components are multiplied element by element with a modified ramp filter to enhance high frequency components. This filter multiplies the frequency components by a coefficient proportional to the absolute value of the corresponding frequencies, except the DC coefficient value, set to ¼ the value of the lowest non-zero frequency coefficient.
- The filtered signal is inverse FFT'ed, giving the filtered back projection function.
- A matrix is filled with interpolated values of the filtered back projection function using the pixel positions orthogonally projected onto the scan line as input.
- The angular scan matrices are added together to complete the reconstruction

In the following, we separate between the image pixels in the reticle focal plane and the reconstruction (matrix) pixels; these can differ in size. The input image used in simulations has a much higher resolution than the simulated camera.

### *5.4 Simulated reconstruction accuracy*

The reconstruction technique used here is not unique, but is useful for real-time imaging, being fast and yielding relatively high resolution. It can, however, produce artefacts surrounding positive or negative spikes, especially with limited angular resolution. Alternative approaches, such as using an iterative search, could provide a better image reconstruction [3,12,13], but such algorithms are often application-specific and computationally demanding.

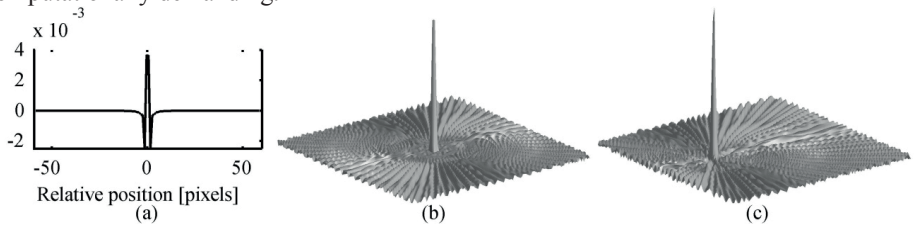


Fig. 8(a) Filtered back projection function and (b) reconstruction of a 512×512 image with a single centred unit pixel. (c) Reconstruction of a 512×512 image with a de-centred unit pixel.

Fig. 8(a) shows a single scan filtered back projection of a 512×512 pixel image with a single centred spike. The dips on both sides of the peak compensate line features from scans in other directions. Fig. 8 show mesh plots of centred (b) and de-centred (c) single pixel image reconstructions. Both reconstructions contain a central peaked main lobe, a transition region with irregular modulation, and then radial ripples, splitting in two due to the slit width. All modulations outside the main lobe are within ±5% of the peak value.

A sample reconstruction without noise or misalignment was made with a 512×512 pixel image 'Lena', shown in fig. 9(a). Fig. 9(b) shows the reconstructed image using a 118×118 pixel grid. Reconstructing onto a 512×512 pixel grid removes the effect of the pixel borders, as seen in fig. 9(c). Line artefacts appear due to a combination of low angular and high spatial resolution, seen in the prolongation of the hair line structure across the brim of the hat.


Fig. 9(a) Original 512×512 pixels high resolution 'Lena' image. Reconstruction using a 65 slit reticle, with 119 samples/scan, onto a 118×118 (b) and 512×512 (c) pixel grid.

*5.5 Geometrical and timing errors*

If the aperture is misaligned with the optical axis, as described in fig. 10(a), the aperture has a circular movement with respect to the nominal FOV, characterized by its radius and phase relative to the optics rotation. Resulting artefact are shown in fig. 10(b), (c) and (d), with a misalignment radius corresponding to 10% of the aperture diameter and a misalignment phase of 0°, 45° and 90°, corresponding to an aperture shift parallel, oblique and normal to the reticle lines, respectively. Compared with fig. 9(b), the shift normal to the reticle lines create a dark ring around the scene and a light background outside the aperture, whereas the shift parallel to the lines blurs rim features more subtly, as angular components are fetched from other parts of the image with similar intensities. This is more easily seen in gradient images.


Fig. 10. Aperture misalignment: (a) Misaligned (red) aperture is displaced from its ideal location (green). The red vector indicates the eccentricity relative to the direction towards the rotational axis (yellow). The misalignment rotates (dashed red circle), the aperture hiding different scene parts during the scan. (b-d): Reconstructions with aperture misalignments corresponding to 10% of the aperture diameter, with the phase angle being 0° (b), 45° (c), and 90° (d).

The distortion arising from a reticle rotation or a time shift is due to a change in the point spread function from a spike to a circle, as illustrated in fig. 11(a). The effect is shown with time shifts corresponding to (b) 1, (c) 5 and (d) 40 samples (recalling that a single scan takes 119 samples). A 1 sample time shift already gives a visible effect: The eyes are smeared out, and the hat brim has a surrounding halo. With a 5 sample time shift a 'double view' effect appears, with lines split in two. Also, an outer dark ring resembling that found in fig. 10(c) appears. A 40 sample time shift distorts the scene totally. Varying the time delay, a characteristic dark halo surrounding the circular image appears at significant time shifts, and when the time shift is reduced, the double line features are found to approach each other. Due to this effect, precise means for measuring scan orientation are necessary.

Using a trigger signal produced once per rotation can correct the previous effect, and enable long term orientation stability, but scan errors can still be introduced by a varying scan speed. We now focus on the effect of shifts caused by speed variations between two triggers. Noting that the distance between two consecutive triggers represents exactly one revolution, we can use resampling to force a zero phase error at these reference points. The phase error in the sample points can then be modelled as a sum of sine waves in between. Fig. 12(b) shows the effect of a phase shift in the range ±5 samples, varying sinusoidally with the rotation. The overall image resembles a shifted version of the ideal reconstruction in fig. 9(b), with an artefact in the region outside the aperture. With a speed variation frequency twice the rotational speed, the effect is visually more dramatic, as seen in fig. 12(c), resembling that of the constant time shift error in fig. 11(c). Simulations show higher speed variation frequency components also give important distortions. The triggered system can thus handle variations with frequencies lower than the rotational speed, but higher frequency variations can clearly cause problems. Potential sources of problems are roller bearings for the rotating optical assembly, the motor as well as its power supply, and the transmission linking the rotating unit and the motor. High rotational inertia reduces this effect.

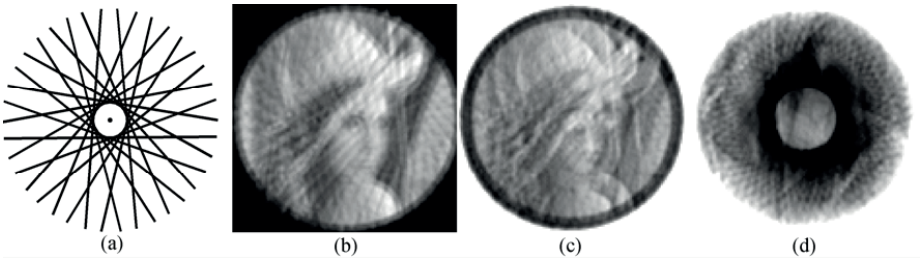


Fig. 11. Line shift errors: Effect of a constant difference between assumed and real scan line location. (a) The footprint of scan lines at the time where the reconstruction assumes them to pass through the centre. This causes point spread function to essentially become a circle-like structure. This error can be due to a fixed timing error or an angularly misaligned (rotated) reticle. Reconstruction similar to that in fig. 9(b), but with time shift errors, corresponding to (b) 1 sample, (c) 5 samples and (d) 40 samples, respectively.

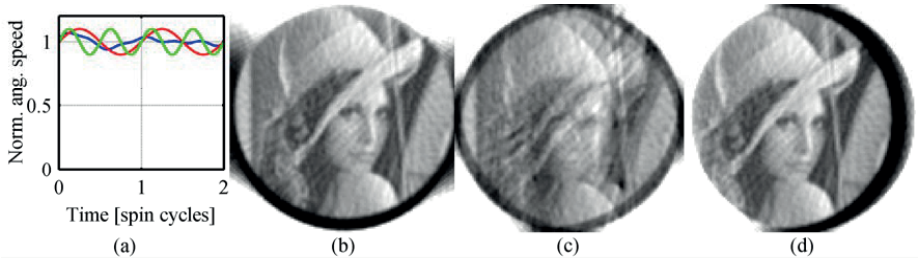


Fig. 12(a) Rotational speeds variations with once (red curve) and twice (green) the rotational cycle frequency, and a general variation (blue). (b) Reconstruction with sinusoidal scan speed variations with a frequency corresponding to one spin cycle, creating a difference between nominal and actual sampling location varying between ±5 samples. (c) Same as in (b), but with twice the scan speed variation frequency. (d) Reconstruction similar to that in fig. 9(b), but with a horizontal reticle offset corresponding to 10% of the aperture diameter.

The reticle may be misaligned by sideways translation. The effect, shown in fig. 12(d) with a misalignment representing 10% of the aperture diameter, resembles that in fig. 12(b): A translated image with a border distortion image. Analytically, these cases are indeed similar.

To sum up, aperture alignment errors essentially produce FOV rim artefacts. Timing and reticle orientation offset is more serious, necessitating a precise angular measurement. It is desirable to avoid jitter in the speed of the scan rotation.

### *5.6 Noise simulations for single- and multi-channel TOSCA configurations*

The simulation includes photon noise and detector noise. Fig. 13 shows simulation results for bright, medium and low light conditions. In bright light, reconstruction artefacts due to the finite number of angular scans represent the dominant distortion effect. Noise is a significant source of error at lower light levels. In fig. 13(c) detector noise is the most

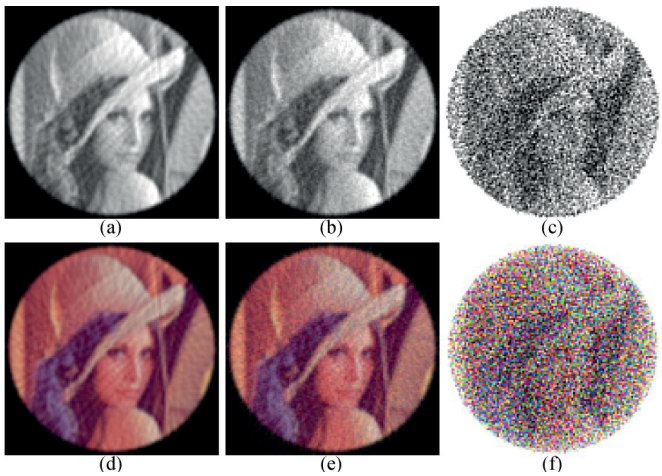


Fig. 13. Reconstruction with detector + photon noise in (a) bright, (b) medium, and (c) low light conditions, where the brightest pixel is scaled to have (a) the same spectral radiant exitance as the reference target in fig. 7(a) ($M_{\lambda,max}$ = 350 $Wm^{-2}\mu m^{-1}$), (b) $10^{-2}$ and (c) $10^{-4}$ of the value in (a). (d)-(f): As in (a)-(c), but with the energy spread to 3 spectral channels.

significant deterioration. The pixel-level signal-to-noise ratio is here < 0.5, but the eye's spatial averaging capabilities still enables recognition of large features. For image sequences, temporal averaging could lower the feature recognition threshold even further.

In multi-channel systems, detectors share the signal photons. Photon noise is then also reduced, whereas the detector noise per channel remains the same. This is shown in fig. 13(d)-(f), where we have 3 channels in the same bright, medium and low light conditions as above. Noise is still not noticeable in the bright light image. In the medium light image, the noise is more significant than in the corresponding monochrome image, and the visual recognition threshold is approached in the low light image, with a signal-to-noise ratio less than 0.3.

## 6. Discussion

There are several ways to enhance the images, but enhancements often tend to be application specific. This is not the main topic of this paper, and only indications as to certain solutions will be given. Kak and Slaney give indications of several possibilities [3]. First, they indicate that the number of angular scans (or projections) should be roughly equal to the number of samples (or rays) per scan, but this is for a general image. Increasing the number of angular scans will reduce the relative ripple, but one then have to increase reticle scan radius, reduce the pixel size, or reduce the number of samples per scan. This is difficult due to design, mechanical and optomechanical constraints.

Adding intermediate scans using a linear interpolation of successive scans can typically remove artefacts in peripheral regions of the image, but at the same time introduce blur in the same locations. Instead of using the simple ramp filter described above, one might choose a modified back projection filter to remove frequency components that are known not to exist in the image, or remove or dampen undesirable components.

It is seen that fig. 8(b) and (c) contains artefacts around the main lobe. These ripples are mainly due to the limited number of angles and the mismatch between a circular and rectangular grid. The first limitation is fundamental, but in the case of the latter, better approximations to the discrete Radon transform employed here could be used [12]. Improved inverse transforms could flatten the area close to the main lobe and narrow the main lobe.

One could also calculate the point spread function of the image, and determine some kind of inverse function to reduce artefacts through convolution. Unfortunately, the point spread function is position dependent, as shown in fig. 4(b) and (c), rendering this task difficult.

It is also possible to use iterative approaches, where the reconstructed image is sent through a construction process. Ideally, this would recreate the original signal, but the difference obtained can be used to modify the reconstruction. This process can be repeated until the error is sufficiently small, provided the process converges. This process is susceptible to noise. An inconvenience is that the iterative process can be time consuming, and will typically not be interesting in real-time applications. In images with high contrast, particularly in the presence of a few very bright "hot spots", signals corresponding to images of these bright objects could be generated and subtracted from the original signal. This simplified iterative approach could potentially remove the biggest artefacts, easing the image analysis.

High frequency illumination variations, low light conditions and strongly asymmetric scene illumination is likely to affect system performance, calling for a more direct scan speed control, but the current solution was deemed sufficient for the demonstration. An optical encoding pattern outside the thin slit reticle pattern could be used as an angular reference.

Better roller bearings and fixtures would be costlier, but could reduce mechanical vibrations and lead to a smaller spot size, enabling a smaller reticle or higher resolution.

The focusing/collimating optics could be separated from the rotating unit, enabling better and more flexible optics. In the setup, focus was adjusted by optics in front of the system.

## 7. Conclusion

This paper presents the first working tomographic scanning (TOSCA) imager. Detailed analysis first show that an imaging camera system using a single pixel sensor and a simple circular scan mechanism can operate as a photon noise limited system in realistic lightning conditions with existing optical and electro-optical components. A detailed physics-based simulation was used to quantify the effect of error sources such as misalignment, temporal sampling errors and scan speed variations. The analysis identified the need for a precise angular reference, but initial simulations indicated that it might not be necessary to have detailed angular position readout for each sample, provided rotational inertia is significant. The effect of noise was also examined through simulation, supporting the initial assumption that the system should have adequate performance. The proposed configuration has some limitations in pure imaging due to a low number of angular scan orientations creating characteristic line artefacts, but is sufficient if objects of interest are located on an otherwise homogeneous background, as artefacts manifests themselves at a distance from the object of interest. Measurements using the experimental setup verified the performance predicted through theory and simulations. Advantages of the inherent geometric co-registration of several spectral channels were highlighted and demonstrated.

**Acknowledgments**

The author is grateful to prof. Svein Erik Hamran and dr. Torbjørn Skauli for helpful discussions and able guidance, to dr. Stéphane Nicolas for doing the ZEMAX simulations, and to mr. Sverre Dyrkorn for doing the SolidWorks construction of the camera.

# Publication V

# Experimental Tomographic Scanning (TOSCA) Imagers

**Harald Hovland**

**Proc. SPIE 9070, Infrared Technology and Applications XL, 90700H (2014)**

# Experimental Tomographic Scanning (TOSCA) Imagers

H. Hovland,
Norwegian Defence Research Establishment, Postboks 25, N-2027 Kjeller, Norway
harald.hovland@ffi.no; phone (+47) 6380 7312; fax (+47) 6380 7212

## ABSTRACT

The tomographic scanner (TOSCA) detects signals using line detectors scanning a scene at regularly distributed angles. These line scan signals are then processed to reconstruct 2-dimensional images. In the simplest form, a 1-axis rotating conical scan optics scans across a simple patterned reticle, the signal collection being done with a single pixel detector. Experimental mono- and multispectral cameras using this approach are demonstrated under varying illumination conditions. Of particular interest is the TOSCA system's ability to handle and compensate for light sources modulated with a frequency higher than that of the frame rate. We also demonstrate for the first time a TOSCA imager operating in the infrared region. The device is put together using 3D-printed key parts and low cost optical components, leading to a very economical infrared camera.

**Keywords:** Tomography, tomographic image processing, imaging systems, infrared imaging, image reconstruction techniques, Fourier optics and signal processing.

## 1. INTRODUCTION

Tomography, from Greek *tomos* (slice), is a means for reconstructing higher dimensional signals from a collection of projections. The technique itself was invented and published back in 1917 by Radon[1], but became famous through Hounsfield's invention of the CAT scanner[2], which earned him a Nobel prize in 1972. When x-rays are radiated through the body, it is not possible to directly determine directly at which point along the path the radiation is absorbed, but it is possible to measure the total radiation loss along the path. Several such measurements are made using measurements from parallel beams to obtain a cross section across the body in one direction. By making similar measurements in different directions, corresponding cross sections in different orientations can be built up. The information thus obtained can be used to reconstruct a 2-dimensional image of the absorption.

With increasing computational capability, newer approaches have been made where scattering is modeled to handle both acoustic and optical waves in strongly scattering media, and most papers on optical tomography deals with this kind of scenarios. The TOSCA concept, however, is much more similar to the parallel beam X-ray case. Here, the detection process is achieved with one or several line detectors scanning the scene. A line detector is here understood either as a detector whose active area has the shape of a thin line, or that the light passes a thin slit before hitting the detector.

The TOSCA camera concept was first presented and then demonstrated in the visible band by the author[3,4]. In this work we show that the TOSCA concept is capable of handling

very rapidly varying scene illumination. We also demonstrate for the first time a TOSCA camera operating in the infrared spectral range. Of special interest is the fact that most of the camera was printed using a 3D-printer, and the optics are low cost, making the system relatively affordable.

In this paper, a simplified presentation of the TOSCA process is explained, before experimental setup and results are presented. Of particular interest is the TOSCA system's ability to handle and compensate for modulated light sources with a modulation frequency higher than the frame rate.

## 2. THEORY

The basic principles behind and the background leading up to the TOSCA detection process is described in previous publications [3, 4, 5, 6, 7], including the mathematics and noise processes, so this chapter is intended to serve as a simplified introduction to the theory. In the simplest case, the line detector scans across an image of the scene, the latter being restricted by an aperture. The scans are done at regularly distributed angles relative to the image of the scene. In this way, each scan represents a plane wave in a specific direction given by the normal to the line detector orientation. All information about spatial plane waves in one direction can be represented as amplitude and phase along a line crossing the origin in Fourier space. The Fourier transform of the scan signal can therefore be used to fill out a line in the Fourier space representation of the scene. In principle, making several scans with different orientations can thus be used to fill out the information about the Fourier space representation of the scene. In principle, once all information about the Fourier space of the scene is known, an inverse transform can be performed to reconstruct the scene.

There are several issues with this approach. First, the discrete nature of the sampling means a discrete number of points will be obtained in Fourier space. Second, the angular density of points in Fourier space decreases with increasing distance from the origin. Notably, the origin is determined several times during the recording of one frame, once per angular scan. Third, the representation in the Fourier domain obtained in the TOSCA measurement process is done in polar co-ordinates, whereas the traditional transforms between frequency (Fourier) and spatial representation are done between sets of Cartesian co-ordinates. And, finally, there are a limited number of samples per scan, meaning that the cyclic properties of the Fourier transform could affect the results.

To take the last issue first, zero-padding the spatial signals before the Fourier transform limits the effect of the cyclic boundary conditions[8]. After filtering and transforming back to the spatial domain, the signal is then truncated.

As for all sampling, artifacts will appear if the sampling relative to the Nyquist criterion is not sufficient[9]. In the TOSCA reconstruction, insufficient angular sampling typically takes the shape of radiating lines away from hot spots at a certain distance, but the artifacts will typically not severely affect structures in close proximity to the hot spot.

The transform between polar and Cartesian coordinates in Fourier space represents an important issue. The coupling between frequency components during an interpolation process in the Fourier domain can significantly affect the results in the spatial domain. The filtered back projection process introduced by Bracewell and Riddle[10] has been found to avoid the coordinate transform interpolation in the Fourier domain altogether, and is also both memory and computationally efficient. In the filtered back projection approach, a transform of each line scan to Fourier space is followed by a multiplication of each frequency component with its distance from the origin. An exception is done at the origin,

where the factor is not 0, but ¼ of the smallest nonzero frequency value to account for the discrete nature of the sampling[3]. If needed in the specific application, additional smoothing coefficients are also included in this process. After this filtering, the result is brought back to the spatial domain by an inverse Fourier transform. The resulting filtered signal is then projected onto a Cartesian grid, where each grid point is assigned the value of its projection onto the filtered scan line, typically using linear interpolation. Summing up the resulting plane waves in different directions, one for each angular scan, finalizes the reconstruction.

## 3. EXPERIMENTS

### 3.1 Visible single color operation

The first experimental TOSCA demonstrator[4] was based on the theoretical concepts in previous work[3]. A sketch of the first demonstrator system is shown in Figure 1. A focusing lens, followed a pair of flat mirrors were used to project an image of the scene onto a fixed reticle with 65 radially oriented slits. While the lens and mirror pair rotates, the reticle remains stationary, and the scene is scanned across the reticle slits sequentially. A circular aperture, rotating with the mirrors and lens, limits the field of view. Behind the reticle, the transmitted light is brought back to the rotational axis using a pair of mirrors, and collimated by another lens before being collected by the lens/detector assembly.

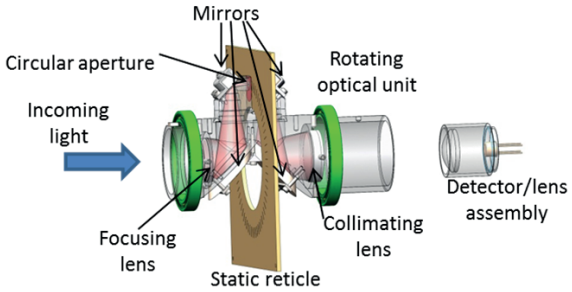


Figure 1. Sketch of the TOSCA configuration used in the first experimental setup.

A characterization of the point spread function is shown in Figure 2. A homogeneous background is created by reflecting sunlight off plain copying paper, and a point is created by reflecting a laser source off the paper at different positions.

To demonstrate the imaging capabilities, an image from the first ever TOSCA recording is shown in Figure 3. Sun light was illuminating the scene indirectly, to obtain stable light intensity as a function of time. This image is part of a 12 Hz image frame video recording.

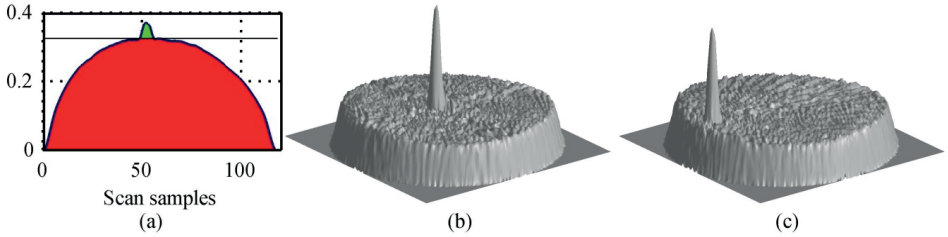


Figure 2. (a) Laser spot (green) and sun (red) reflection contributions in a single scan. Reconstructed images with (b) centred and (c) de-centred laser spots. Images from Hovland[4].

Figure 3. Imaging properties demonstrated during the first ever recording with the TOSCA demonstrator, showing the author looking into the camera lens.

### 3.2 Compensation of illumination modulation with frequency components higher than the frame rate

An interesting property of the system appears when using artificial illumination. In Norway, indoors illumination using fluorescent lamps have a significant 100 Hz modulation frequency, almost an order of magnitude higher than the 12 Hz frame rate. This is shown in Figure 4 (a), where the illumination variation, measured to be around 20-30 % of the average level, is not compensated for, giving the hair of the subject an almost wavy look. Despite the high modulation frequency, it is nevertheless possible to compensate for this. The reason is that the total intensity is recorded for each angular scan, at the much higher rate of 780 Hz. The determination of the intensity at each line scan is inherent in the processing, and it is therefore possible to both detect and characterize the intensity modulation, and to compensate for it using a simple normalization. The result is shown in Figure 4 (b), where the hair no longer shows the wavy feature.

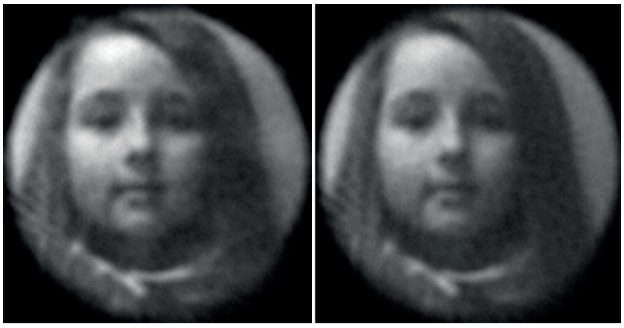

(a) (b)

Figure 4. (a) “Victoria”, recorded using artificial illumination, featuring 100 Hz modulation, much a frequency much higher than the 12 Hz frame rate. The apparent waviness of the hair is an artifact of this illumination modulation. (b) “Victoria”, image, where the illumination modulation level has been determined from the recordings and compensated for, by determining the intensity at each line scan.

### 3.3 Multi-spectral operation

To demonstrate multispectral operation, a Thorlabs FD2G green interference filter was used as a 45° spectral beam-splitter after the collimator lens shown in Figure 1. The two resulting light beams were then collected using two (identical) lens/detector assemblies. The modified setup is shown in Figure 5 (a).

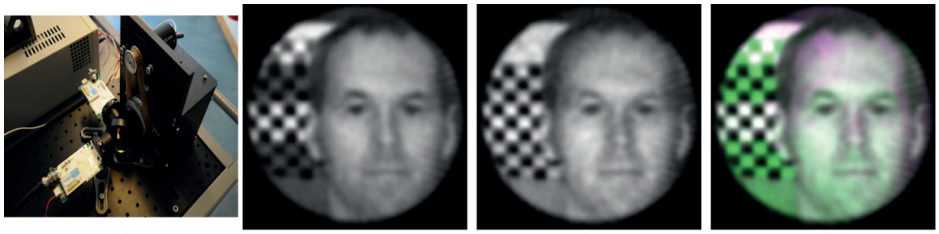

(a) (b) (c) (d)

Figure 5. (a) Multispectral TOSCA setup. A spectral interference filter splits the beam in two. Each beam is detected with a lens/detector pair. (b)-(d) Author image with green/white, green/ black and white/black checkerboard patterns in (b) 'non-green' channel, (c) 'green' channel and (d) a color-coded combined image. The white/black checkerboard pattern transition color purity is due to perfect alignment between channels, inherent in the TOSCA system. Images from Hovland[4].

Operation was modified by changing the recording from one detector channel to two. The resulting images from the 'non-green' and 'green' channels are presented in Figure 5 (b) and (c), respectively, and a composite two-channel image is shown in (d). The black/white pattern is of particular interest. Both 'non-green' and 'green' dominance is visible elsewhere, but does not appear in any black/white transition. Color artifacts often appear at such transitions in multispectral images from cameras with spectral misalignment, and can cause problems when looking for objects with a specific spectral signature or during anomaly detection, particularly when looking for sub-pixel targets[11]. In the TOSCA camera this problem is different, as the image geometry is defined by the narrow reticle slits and the aperture, which are common for all spectral components. Similar artifacts might instead appear if the detector/amplifier chains of different spectral channels have different temporal filter or non-linear characteristics. In addition, artifacts due to the point spread function could also affect this issue, as the color of a strong intensity peak would create surrounding ripples.

### 3.4 Infrared TOSCA

An infrared (IR) TOSCA-demonstrator setup has been built. The setup is very similar to Figure 1, except that the focusing and collimating lenses no longer rotate with the mirrors and circular aperture. The main components (except the motor, drive belt, roller bearings, optics and detector assemblies) were printed on a Makerbot Replicator 2X using ABS plastic. The focusing and collimating lenses were Thorlabs best form 75 mm focal length, 1" diameter uncoated BK-7 lenses, whereas the collecting optics in front of the detector consisted of a Thorlabs 40 mm focal length, 1" diameter BK-7 best form lens. The detector used was a 3 mm × 3 mm Thorlabs PDA30G-EC PbS detector. A Umicore germanium substrate was used just in front of the detector as a 1.8 µm long-pass filter. Given the transmission curves of the BK-7 lenses, the germanium filter and the PbS detector responsivity, the overall system spectral responsivity should be in the 1.8-2.5 µm range, although this has not been confirmed by measurements.

Figure 6. IR TOSCA reticle, printed with the 3D printer. The reticle incorporates the fixture frame with mounting holes leading to an automatic centering of the mask. As seen, not all the 21-slot air gaps are open, so a grinding process was necessary to produce acceptable slits. A simple hand tool was found sufficient.

The reticle, shown in Figure 6, was also 3D-printed using ABS plastic used 21 air gap slits with a designed 0.6 mm slit width, for a slightly less than 6 mm diameter circular aperture (which would nominally result in a 10 pixel wide scene). This proved to be too demanding for the printer, but acceptable results were obtained using a hand tool to grind the slits after printout. Slots into which the 1.3 mm aluminum first surface mirrors could be inserted proved to be of acceptable accuracy, also in terms of parallelism, and the mirrors were simply pushed in place with only minor adjustments being necessary. The adjustments were made using paper in some locations on the mirror back sides. When the optical unit was rotated slowly around its axis prior to mounting the lenses, a small movement was observed when looking along the rotational axis, but the rotating aperture was observed to move together with the scene, which would indicate a sufficient alignment, provided the detector/lens assembly field of view is sufficient to cover the whole reticle.

The IR TOSCA setup did not include a reference sensor to determine absolute orientation, so the target orientation had to be determined during post processing. Once aligned, it retained the alignment throughout a recording, though, even if the motor speed was only stabilized in a stand-alone circuit. One of the reasons is that the reconstruction algorithms feature minimum signal detection, corresponding to the time when no reticle slits overlap the circular aperture between each line scan. By tracking the temporal location of these minimum signals, and then resampling the line scan between consecutive minima, it is possible to compensate for both offset and slowly varying scan speeds. This has the advantage that no particular control loop is strictly required for the motor steering, as inertia limits the speed variations within the millisecond time span between detection minima.

The lenses were put in place using simple press fit fixtures consisting of three small half-cylinder shapes in a circular hole slightly larger than the lens diameter. Ball bearings were press-fitted onto the spinning optical unit. The optical unit was made in two parts, fixed together using four screws. The ball bearings were press-fitted inside fixtures that also held the lenses on each side, and the lens/detector assembly was press-fitted inside a unit that also held the collimator lens.

The motor used was a SmartMotor, from Moog Animatics. The detector signals were recorded using a National Instruments NI PCI-6123 A/D-card. Sampling was done at 100 kHz prior to digital low-pass filtering and resampling.

The complete assembly is shown in Figure 7.

Figure 7. IR TOSCA camera, seen from two angles. The unit consists of, from left to right: Lens holder (red), roller bearing fixture (black), roller bearing (steel), periscopic mirror holder with circular aperture (black, circular barrel), 21-slot air gap reticle (black rounded square shape), motor fixture with motor (black), periscopic mirror holder with toothed wheel incorporated (black, connected to the motor toothed wheel), roller bearing (steel), collimator lens holder with press fit tube for lens/detector assembly (red), detector/lens assembly (black).

Figure 8. Halloween target mask used for the IR TOSCA experiment.

The target, shown in Figure 8, was made as a Halloween cardboard mask. At the back of the cardboard mask, plain white copying paper was illuminated using a halogen lamp to create a (relatively) uniform target.

The IR TOSCA camera was operated at a 5 Hz frame rate. A sample reconstruction is shown in Figure 8. As can be seen, the target is relatively easy to recognize, despite the inherently low sampling and relatively crude optics. The image was observed to move and degrade somewhat during the recording; this is partly due to camera motion, partly to the 100 Hz modulation of the Halogen lamp, which in this case was close to the 105 Hz line scan frequency.

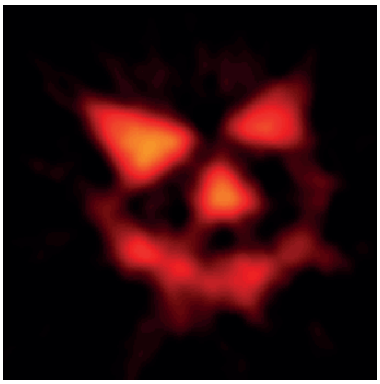

Figure 9. Halloween target mask reconstruction. The camera operated at 5 Hz, and the 21 slit reticle had a 0.6 mm slit width. In combination with the 6 mm circular aperture, this would indicate a nominal 10x10 pixel resolution.

## 4 CONCLUSIONS

The TOSCA imager has been demonstrated in both the visible and the infrared band. It has been shown that practical systems can be created, and due to its special scanning properties it is found capable to handle significant illumination modulation at frequencies far higher than the sampling rate. The use of a relatively low cost 3D-printer has proven to be sufficient to create a very low cost infrared camera, where a PC would represent the most significant cost component. The motor used in the setup could be replaced with a cheaper unregulated unit, and the A/D card could be replaced by the sound card input of a regular PC, making IR imaging accessible on a limited budget.

## ACKNOWLEDGEMENTS

The author is grateful to Prof. S E Hamran, Dr. T Skauli and Dr. J Moen for helpful discussions during this work.

## REFERENCES

[1] Radon, J., "Über die Bestimmung von Funktionen durch ihre Integralwerte längs gewisser Mannigfaltigkeiten," Ber. Verh. Sichs. Akad. Wiss. Leipzig, Math.-Nat. KI. 69, 262-277 (1917).

[2] Hounsfield, G. N., "A method of and apparatus for examination of a body by radiation such as X- or gammaradiation," UK Patent 1283915 (1972).

[3] Hovland, H., "Tomographic scanning imager," Opt. Express 17(14), 11371-11387 (2009).

[4] Hovland, H., "Construction and demonstration of a multispectral tomographic scanning imager (TOSCA)," Opt. Express 21 (4), 4688-4702 (2013).

[5] Hovland, H., "Tomographic scanning imaging seeker," Proc. SPIE 5430, 76-85 (2004).

[6] Hovland, H., "Specialized tomographic scanning imaging seeker," Proc. SPIE 5778, 725-738 (2005).

[7] Hovland, H., "Optimization of the tomographic scanning (TOSCA) imager," Proc. SPIE 6569, 65690I (2007).

[8] Kak, A., Slaney, M., [Principles of computerized tomographic imaging], IEEE Press, New York, 70-71 (1988).

[9] Hsieh, J., [Computed tomography principles, design, artefacts, and recent advances], SPIE Optical Engineering Press, Bellingham, WA, 167-240 (2003).
[10] Bracewell, R. H., Riddle, A. C., "Inversion of fan beam scans in radio astronomy," Astrophy. Journ. 150, 427-434 (1967).
[11] Mourolis, P., Green, R. O., Chrien, T. G., "Design of pushbroom imaging spectrometers for optimum recovery of spectroscopic and spatial information," Appl. Opt. 39, 2210-2220 (2000).

# Publication VI

# SPIN SCAN TOMOGRAPHIC ARRAY-BASED IMAGER

**Harald Hovland**

**Optics Express Vol. 22, No. 6, 31999-32015 (2014)**

The publication is open access, available at:

http://www.opticsinfobase.org/oe/abstract.cfm?URI=oe-22-6-31999

The online publication also links to multimedia material.

# Spin scan tomographic array-based imager

**Harald Hovland**

*Norwegian Defence Research Establishment (FFI), Postboks 25, NO-2027 Kjeller, Norway*
*harald.hovland@ffi.no

**Abstract:** This work presents a novel imaging device based on tomographic reconstruction. Similar in certain aspects to the earlier presented tomographic scanning (TOSCA) principle, it provides several important enhancements. The device described generates a stream of one-dimensional projections from a linear array of thin stripe detectors onto which the (circular) image of the scene is rotated. A two-dimensional image is then reproduced from the one-dimensional signals using tomographic processing techniques. A demonstrator is presented. Various aspects of the design and construction are discussed, and resulting images and movies are presented.



**OCIS codes:** (070.6020) Fourier optics and signal processing; (100.6950) Tomographic image processing; (110.0110) Imaging systems; (110.3010) Image reconstruction techniques; (110.6960) Tomography.

## References and links

1. H. Hovland, "Tomographic scanning imager," Opt. Express **17** (14), 11371-11387 (2009).
2. H. Hovland, "Construction and demonstration of a multispectral tomographic scanning imager (TOSCA)," Opt. Express **21** (4), 4688-4702 (2013).
3. H. Hovland, "Experimental tomographic scanning (TOSCA) imagers," Proc. SPIE **9070**, 90700H (2014).
4. A. C. Kak, M. Slaney, *Principles of Computerized Tomographic Imaging* (IEEE, 1988). http://www.slaney.org/pct/pct-toc.html.
5. R. N. Bracewell, A. C. Riddle, "Inversion of fan-beam scans in radio astronomy," Astrophys. J. **150**, 427-434 (1967).
6. G. T. Herman, *Image Reconstructions from Projections* (Academic, 1980).
7. A. H. Andersen, A. C. Kak, "Simultaneous algebraic reconstruction technique (SART): A superior implementation of the art algorithm," Ultrason. Imaging **6**, 81-94 (1984).
8. H. Hovland, "Specialized tomographic scanning imaging seeker," Proc. SPIE **5778**, 725-731 (2005).

## 1. Introduction

Tomographic scanning (TOSCA) imaging was presented earlier [1] as an alternative way of acquiring images using various types of radiation. In the TOSCA imager, thin lines scan the scene at regular angular intervals, as seen in Fig. 1(a). These 1-dimensional scans are then processed with tomographic reconstruction techniques to reproduce a 2-dimensional image.

In [1], it was shown that a single pixel sensor combined with a simple circular conical scan mechanism could produce images with better signal-to-noise ratio than achievable with classical single pixel imagers using 2D scanning, and demonstrators were presented in [2, 3] as proofs-of-concept. The working principle used in the demonstrators is shown in Figs. 1(b) and 1(c). It was shown that the concept could give adequate image quality for a low-noise silicon detector with reasonable light conditions, but the typical noise levels of detectors operating in the infrared domain restricts the useful imaging to very hot objects, very limited resolution or imaging of static objects with relatively long exposure times.

An array-based TOSCA imager concept was also proposed in [1], potentially producing images with better signal-to-noise ratio than that of a classical broom-scan linear array. The circular array would then be similar to the reticle shape in Fig. 1(c), but because several line detectors can be in the field of view (FOV) simultaneously, the detector spacing could be so small that the detectors touch each other, reducing the scan circle and simplifying the optics.

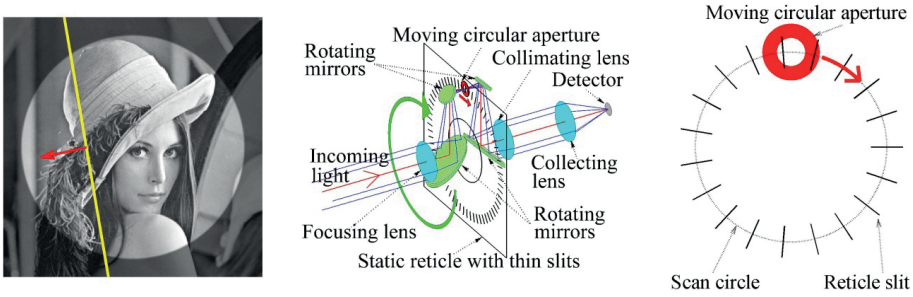


Fig. 1. (a) TOSCA imaging: A thin line detector (yellow line) scans across the image of the scene, the latter being restricted by an aperture. Alternatively, an array can replace the single line detector. The scan is repeated at different angles. (b) Conical scan TOSCA working principle used in the demonstrator presented in [2, 3]. The mirrors (green) and the aperture (red) rotate as a unit around the optical axis of the incoming light. The image orientation remains fixed relative to the reticle, therefore the thin slits scan the image at regular angular intervals. (c) Reticle pattern and moving aperture layout. The aperture (in red), defining the field of view, moves in a circle. The use of an aperture enables the use of a single detector element to make all the angular scans without aliasing as only one slit transmits light from the scene to the detector at any time. All images are reproduced from [2].

This paper presents a new array-based tomographic scanning imager design making use of spin scan optics. The spin scan TOSCA imager has a potentially better noise performance than a conventional line scan imager, and with the right readout electronics it has a capability for detection and, to a certain degree, also characterization and localization of transients that can be faster than the time constants associated with the frame rate. It is therefore suitable for use in low cost sensor in unmanned aerial vehicles, especially systems looking for or at fast phenomenons.

The new design represents a clear improvement to the previously presented conical scan TOSCA design, both in terms of performance and manufacturability. Several implementations are proposed for the optics of such a system.

An experimental demonstrator based on this design is presented, operating in the mid-infrared range. The aim of this demonstrator is to show a practical implementation of this TOSCA imager concept, also illustrating artifacts that can arise. The camera design is presented, including the signal processing necessary for the image reconstruction. Sources of noise and systematic errors are discussed. Simulations highlight important design considerations.

## 2. Spin scan TOSCA design

### *2.1 Basic principle*

The basic spin scan TOSCA sensor principle is illustrated in Fig. 2. It consists of optics that focuses an image of the scene onto a linear detector array, while rotating the scene image relative to the linear array.

The detector array FOV could be limited either by a circular aperture in front of it, or by adapting the active length of each detector to a corresponding circle. Thus the number of spatial samples across the FOV for one angular scan is given by the physical linear array, but the number of angular scans is given by the sample rate and the optics rotational speed. This is the opposite of the conical scan TOSCA, where the rotational speed defines the number of samples per angular scan, whereas the array or reticle determines the number of angular scans.

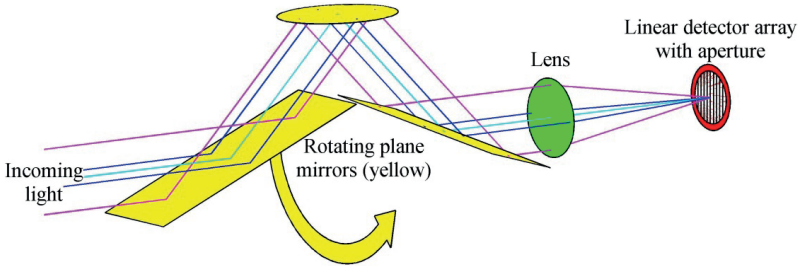


Fig. 2. Spin scan TOSCA imaging: A rotating image of the scene is projected onto a linear detector array. This example features the use of three rotating plane mirrors and a lens. The mirrors (yellow) that flip the image of the scene rotate as a unit with respect to the scene, while the detector array remains stationary.

Once the signal has been sampled, the reconfiguration follows classical parallel beam tomography reconstruction [4]. A short description of the procedure used here is as follows:

1. The signals are sampled for $M$ regularly distributed angular positions around the circle for each TOSCA reconstruction.
2. $N$ samples are made per angular position, one for each of the $N$ detectors.
3. Zero pad the $N$ samples to limit the fast Fourier transform (FFT) continuous boundary effects, adding at least $N$ extra samples. Letting the number Z of zero-padded samples be a power of two optimizes the subsequent processing.
4. Take the FFT of each zero-padded sample series.
5. Multiply the components of the resulting FFT series value by value with its corresponding absolute frequency value, with the exception of the first (zero frequency) coefficient, which should be ¼: {¼, 1, 2, … , Z/2, Z/2-1, … 2, 1}. If needed, modify this ramp filter with an application-specific smoothing filter.
6. Take the inverse FFT of the product. Remove excess samples added in point 3.
7. For each angular position, produce a back projection matrix where each pixel is given the (linearly) interpolated value of the series found in point 6, the indices being based on the pixel's orthogonal projected position on the scan line. The back projection matrix resolution can be different from that of the initial scan.
8. The reconstruction is completed by summing up all the filtered back projection matrices (and normalizing if needed).

The filtered back projection technique, originally developed by Bracewell et al [5], has been found to be an efficient first order method. It is possible to improve the result by (iterative) algebraic reconstruction techniques [6, 7]. This, however, might not be acceptable in a real-time system due to unwanted latency or high computational requirements.

## *2.2 Optical configurations*

The spinning scan optics can be realized in several alternative ways, as shown in Fig. 3. In the simplest form, the focusing optics and the linear detector array are rotating together as in Fig. 3(a), a concept useful in for example rotating projectiles.

A combination of rotating optics with an odd number of reflecting surfaces such as the depicted dove prism in Fig. 3(b), or the three reflecting mirrors shown in Fig. 2, provides the flipping of the field of view and rotation, while regular focussing optics provides the imaging.

A particularly compact solution is seen in Fig. 3(c), where a toroidal concave primary mirror opposes a cylindrical (or toroidal) concave secondary mirror, both rotating as a unit. This configuration, not seen before in the literature by the author, enables a compact combined focussing and flipping of the image using only two optical elements. An equivalent, but less compact solution based on regular and cylindrical lenses is shown in Fig. 3(d).

If only the optics is rotating, the FOV angular speed will be twice that of the optics. In [1, 2, 8], a point was made in having an odd number of angular scans, as two angular scans with a 180° shift contain equivalent information. For the spin scan configuration, the situation is the same for a symmetrically mounted linear array, and scans during a ½ FOV rotation relative to the linear array enable a complete image reconstruction. If, however, the linear array is shifted by ¼ pixels sideways, a doubling of the sampling density can be achieved with a 32 element linear array sampling 64 pixels across the FOV based on two angular scans separated by 180°. A complete scan then requires a 360° scene image rotation relative to the linear array. This doubling in spatial resolution should also be followed by an additional doubling of the number of angular steps, quadrupling the number of angular scan positions.

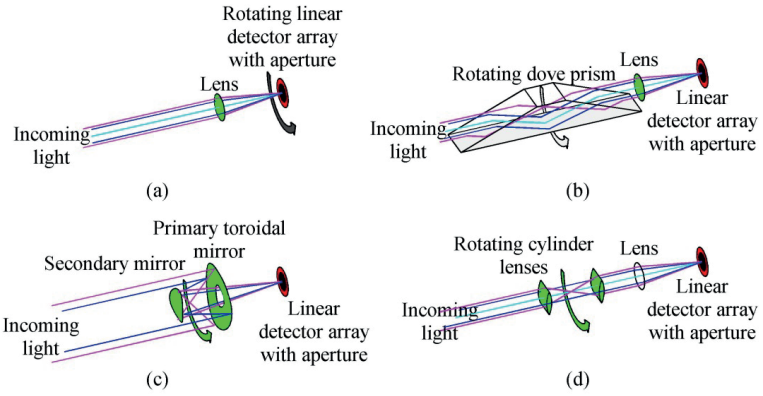


Fig. 3. Alternative TOSCA spin scan optical configurations: (a) Rotating detector array. (b) An odd number of reflecting, rotating planes, for example a dove prism (or three reflective mirrors as in Fig. 2). (c) A toroidal primary mirror facing a secondary toroidal or cylindrical mirror. A similar effect can be obtained using thick refractive optics, with one toroidal front surface and one toroidal or cylindrical back surface. (d) A similar realisation using a combination of two cylindrical lenses and one spherical lens.

## 3 Comparison of the spin scan versus the conical scan TOSCA configurations

### *3.1 Photon efficiency*

In the reticle based (single pixel) conical scan TOSCA configuration, only one scan line can be in the FOV at the same time. This limits the FOV covered by the detector active area at any given time. Define, as before [1], the photon harvesting efficiency as the average proportion of the incoming photons collected by the sensor. Assuming an idealized sensor and optics where the aperture diameter is $N$ times the slit width, the maximum photon harvesting efficiency for the reticle based configuration is $N^{-1}$. This can be seen by noting that the slot in the reticle covers the equivalent of one of the N pixel rows at any time.

If the reticle is replaced by $M$ individual line detectors arranged in a radial pattern, several detectors can be in the field of view at the same time. This allows a reduced scan circle diameter, and also increases the photon harvesting efficiency compared to the reticle based configuration. M then represents the number of scan angles. We assume in the following that the aperture diameter is $N$ times the detector width. This means N represents a measure of the number of pixels both along and across the scan direction.

The theoretical upper limit of the photon harvesting efficiency is found by geometric considerations to be $M/(M+\pi N)$: In this optimum conical scan array-based configuration, the M radially oriented detectors are arranged in a star-shaped circular array, such that one end of each of the M radially oriented detectors touches those of its two neighbours, forming a closed inner circle from which the detectors extend, with a diameter of $M/\pi$ times the detector width. If the scan circle crosses the middle of each line detector, the scan circle diameter is $M/\pi+N$ detector widths, giving a scan line perimeter of $M+\pi N$ detector widths. Assuming one sample is made per detector width along the scan circle, and noting that each pixel is scanned one time by each of the $M$ detector lines per frame, the photon harvesting efficiency becomes approximately $M/(M+\pi N)$. This is an approximation, as the scan velocity vector is generally not exactly normal to the line detector orientation.

The expression $M/(M+\pi N)$ degenerates to the value $(1+\pi)^{-1} \approx ¼$ reported in [1] in the case where $N=M$. The value of this expression could in principle approach unity if the number of scan angles (and hence detectors) is much larger than the aperture to slit width ratio $N$. For practical configurations, however, the photon harvesting efficiency is likely to be below ½ for the array based conical scan TOSCA configuration. In contrast, the parallel structure of the line detector array in the spin scan TOSCA configuration presented here allows practically the whole scene to be projected onto active detector surfaces at any time, giving an idealized system a unity photon harvesting efficiency. This would be on par with a 2D focal plane array.

As was described in [8], the conical scan TOSCA configuration was demonstrated to be able to handle modulation levels higher than the frame rate. The reason for this capability is that the total FOV is scanned many times per frame, so that an assessment of the total signal level could be made and compensated for. The spin scan TOSCA has a similar, but better assessment capability, due to both the potential near unit photon harvesting efficiency and simultaneous 1-dimensional localization possibility of strong transients. The detection of fast transients could be done by monitoring the total energy of the FOV for one angular position, and the localisation could be made by comparing the energy in individual detectors from neighbouring angular positions or previous frames. The same comparison could also be used to compensate for undesirable transients.

### *3.2 Signal to noise performance*

The detector bandwidth required to adhere to the Nyquist criterion is $2\times f\times$<*samples/frame*>. For the TOSCA spin scan array configuration here would be $2\times f\times M$, where $f$ is the image frame rate and M the number of angular scan positions per frame. In comparison, the TOSCA conical scan array configuration detector bandwidth required would be slightly higher, $2\times f\times(M+\pi N)$, as higher scan speed is required to scan across the more sparsely distributed detectors, the number of scans being developed above. In line with the analysis in [1], the signal to noise level would be around $(1+\pi) \approx 4$ times better in a spin scan TOSCA configuration than in a corresponding optimized conical scan array based TOSCA configuration, and with a signal-to-noise ratio $M^{-½}$ relative to that of an idealized 2D detector array, based on the pure detector bandwidth requirement.

A more detailed noise analysis can be made by considering the TOSCA model with the following assumptions: The scene is uniformly illuminated, and the detectors are shot noise limited with Poisson noise statistics, with negligible noise in the readout electronics. We can define (virtual) pixels in the scene image on the detector array, each pixel being square with the side equal to the width of each line detector.

The inverse fast Fourier transform (IFFT) of the ramp filter (which is in the Fourier domain) used to create the filtered back projection of each scan represents the coefficient with which each pixel will contribute to the final central pixel for a given angular scan. As was also found in [1] for the conical scan TOSCA configuration, the central pixel will get the highest noise contribution from the other pixels in a scene, and therefore represents a conservative noise estimate for the system. Assuming a uniformly illuminated scene that does not change during one frame, a well reproduced filter with a sufficiently high number of angular scan positions and detectors per scan will ideally create orthogonality, so that all signal contributions that are not from the central pixel will cancel out. The noise from all the pixels, however, will add together incoherently with a coefficient that equals the corresponding absolute value of the IFFT components of the ramp filter. The IFFT of the ramp filter represents a "line spread function" of the filtered back projection and has some useful properties for noise estimation. The sum of the absolute values of the points on each side of the zero position approximates well to the centre point value. For a given scan orientation, this means that the noise contribution of all the detector elements except the one that is aligned with the central pixel, approximates well to the noise contribution of the central detector element (neglecting for simplicity the effect of the circular aperture). Because all $N$ pixels along the central detector element have the same coefficient, they will, for the uniform scene, give the same noise contribution for this particular angle (including the central pixel). A conservative estimate of the noise contribution to the signal of all the pixels is therefore $(2N)^{½}$ times the noise contribution of the central pixel for each angular sample. The incoherently added noise for all the $M$ angular positions is similar, resulting in a total noise figure of $(2N\times M)^{½}$ times the noise of the central pixel for one angular sample. If $P$ photoelectrons are created in each pixel during each angular scan, and we assume shot noise to be the main contribution, the intrinsic central pixel noise during one sample would be $P^{½}$.

A 2D detector array with the same frame rate would have the potential to accumulate $M\times P$ photoelectrons per pixel, with $(M\times P)^{½}$ pixel noise, giving a signal-to-noise ratio of $(M\times P)^{½}$. The ideal spin scan TOSCA sensor would also accumulate $M\times P$ photoelectrons per pixel, but with a central pixel noise level of $(2N\times M\times P)^{½}$ times, giving a signal-to-noise ratio of $(M\times P/2N)^{½}$. For array sizes between 32 and 128 this represents approximately an order of magnitude worse results than for an ideal 2-dimensional detector array in terms of noise.

### *3.3 Effect of misalignment and other optomechanical imperfections on the recorded signal*

Noise and errors can also arise from optomechanical imperfections of a mechanically scanning system. In [1], a temporal constant offset by one or a few samples in the reticle based conical scan TOSCA configuration transforms the system point spread function into a doughnut shape, creating blurring and double line features in the scene. A sufficiently large offset degrades the image completely. This issue is less severe in the array based conical scan TOSCA configuration, with a star-shaped detector array, where the number of samples per rotation is significantly smaller due to a smaller scan circle, easing the control requirements of the optics rotational speed.

In this spin scan configuration, the effects of timing jitter or offset are different. A simulation of high resolution reconstruction similar to the one used in [2] was implemented, with a nominal 299 angular scan steps. The nominal case reconstruction is shown in Fig. 4(a).

Because the sample positions across the field of view are defined by the geometrical layout, a constant temporal shift will not affect detector positioning along the scan line. Instead, the scan line angle is shifted, such that a constant offset will rotate the entire image without any other deformation. This was not simulated, as the argument is straightforward. In a practical application, the detector array geometry is defined by photolithography which, thanks to the demands of microelectronic manufacturing, tends to be more than accurate enough to neglect geometrical imperfections such as nonparallellism of the detector elements.

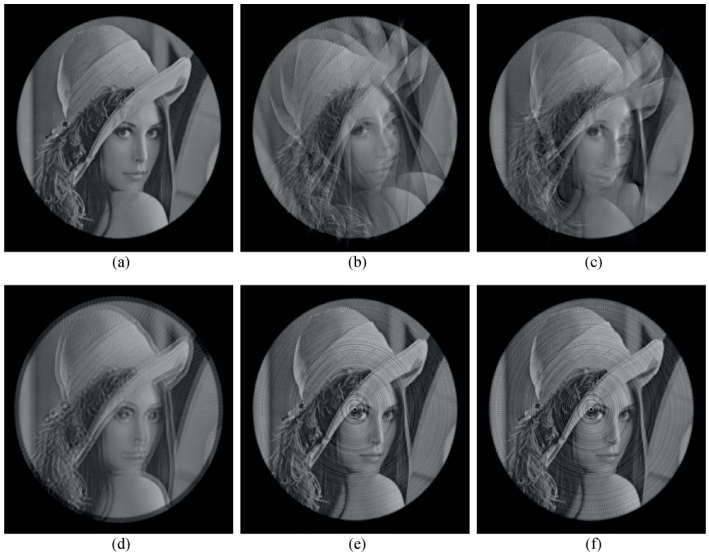


Fig. 4. Simulated high resolution spin scan TOSCA reconstruction to highlight errors related to spin speed errors. (a) Normal reconstruction with 299 angular scans. (b) Reconstruction with a constant, 10% speed error (too high). (c) Reconstruction with a sinusoidally varying phase shift in the scan speed. (d) Reconstruction with the camera misaligned with the rotating optics, orthogonally to the detector orientation. Reconstruction with nonuniform gain (e) and offset (f).

A constantly varying shift can appear if the rotational speed is different from that required by the sample rate and number of angular scans per frame. The reconstructed images will then rotate, and also deteriorate. This is shown in Fig. 4(b), where the

rotational speed is 10% too high. This is most likely higher than what might be expected in a real system, but highlights the effects. The image looks almost like a multiple exposure, with a rotation, but there is also an additional angular distortion. The multiple exposure effect arise as the angular scan is done with a 360° rotation, and all scans separated by ~180° will be shifted by the same amount. As this is an angular distortion, the effect is more accentuated for features closer to the edge. Central features will be less deteriorated, but they will be affected by artifacts generated by peripheral features, typically creating a "veil" over the central part of the image.

Various other errors are possible in the rotational movement, such as jitter and instability. As an example, the reconstruction in Fig. 4(c) shows a phase shift during the angular scans varying sinusoidally from 0° to 15° and back during one rotation. The resulting features are similar to those of the constant speed variations, with the central "veil" and shape deformation on the sides, but the double exposure effect is only visible in parts of the scene. Also, the scene would not appear to rotate, and small errors of this kind might therefore be slightly more difficult to notice.

Misalignment of the sensor position relative to the rotating optics axis can create severe deformations if the misalignment is in a direction across the detector element orientation, very similar to the constant offset timing deformations seen in the conical scan TOSCA imager [2]. This is illustrated in Fig. 4(d). The deformations observed here, point sources deformed into rings, and lines deformed into double line features are due to the doughnut shaped point spread function. The misalignment that is parallel to the detector orientation, not shown here, is less significant, and creates mainly a circular deformation zone at the edge of the circular scene, similar to the artifacts created in the conical scan TOSCA imager with a misaligned aperture.

The less than 100% fill factor might affect the imaging properties, as point sources passing across the resulting spatially regularly modulated responsivity variations could create unwanted signal modulation. A more generalized modulation could also arise due to spatial inhomogeneity of both detector gain and offset. If temporally stable, this kind of modulation could create circular pattern artifacts, due to the circular detector movement relative to the scene. A simulation of nonuniform gain is shown in Fig. 4(e), and a simulation of nonuniform offset is shown in Fig. 4(f). As can be seen from the reconstructions, the effects of these nonuniformities have very similar appearances, here exaggerated by using the same random sequence.

## 4. Experiments

### *4.1 Experimental setup*

A spin scan TOSCA array based imager was built to demonstrate the concept, shown in Fig. 5. The implementation uses three rotating plane mirrors as shown in Fig. 2. The focusing optics, the aperture and the detector array is implemented using a 32×32 pixel uncooled PbSe Matrix Core-S focal plane array (FPA) USB camera from New Infrared Technologies with 24 mm focal length, f#=1.2 germanium optics. By combining signals from columns of pixels, this fast camera can emulate a 32×1 array of long detector elements. The uncooled detector chip is specified to have a spectral range from 1.0 to 5.0 μm, with peak responsivity at 3.7 μm. With the germanium optics, the spectral range is reduced to 1.8-5.0 μm.

The camera is not capable of analog binning of a full column; therefore it is running as a 2D focal plane array, with a subsequent software binning. This limits the operation to 100 angular positions per second and limits the photon harvesting efficiency, but enables monitoring of the intrinsic 2D imaging during the angular scans and also eases the camera alignment to the rotating optics. The selective use of pixels inside a 32 pixel diameter

circle also enables the emulation of an aperture, which is then unnecessary to implement in hardware. The camera operates in a free-running mode, reporting acquired images when finished.

The rotating optics consists of a rotating mount which holds the three flat mirrors that flip the scene. The unit is connected to a Moog Animatics SmartMotor stepper motor via a timing belt. The angular orientation is slaved to the camera frame rate, with the desired number of angular scan positions per revolution as an input to the control software. Control of the rotating optics and the camera, the signal processing, image reconstruction, live visualization and data storage is implemented in National Instruments' LabView.

Given the limited resolution, simple targets were chosen for the imaging experiments:

1. A mask with a 5 mm diameter circular pinhole, made with a 20 mm diameter circular steel plate mounted on a thick cardboard plate in front of a 300°C blackbody. The TOSCA image was reconstructed from 99 angular scan positions.
2. A mask with two 5 mm pinholes, separated by 30 mm center-to-center in front of a 300°C black body. The reconstruction used 99 angular scan positions.
3. The same setup of two 5 mm pinholes where one pinhole was covered by an uncoated 2 mm thick germanium wafer.
4. "Halloween lantern" cardboard mask shown in Fig. 6, back illuminated by a 300°C black body. Reconstructions were made using a range of angular scan step sizes.
5. Halloween mask, back illuminated by halogen lamp light reflected off white paper. The TOSCA image was reconstructed from 99 angular scan positions.
6. Halloween mask, back illuminated by a 300°C black body, but with the triangular nose of the mask covered by the germanium wafer. The TOSCA image was reconstructed from 99 and 199 angular scan positions, respectively.

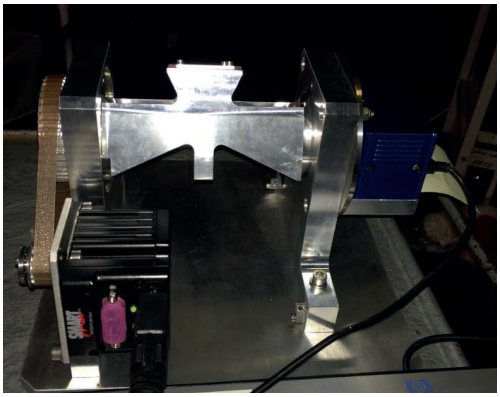

Fig. 5. Experimental spin scan TOSCA camera setup. The main components are the step motor (black, left), the 32×32 pixel FPA camera (blue, right), and the rotating optical unit with the three mirrors is in the centre. The optical unit features a counterweight to minimise vibrations.

Fig. 6. Cardboard Halloween mask target used in the experiments.

The germanium substrate approximately halves the transmitted signal from the hot blackbody, reducing the contrast between the mask and the substrate covered apertures by almost an order of magnitude, compared to the contrast between the mask and the blackbody.

The PbSe camera raw images recorded were found to exhibit a non-negligible amount of offset drift. Therefore, a 100 frame temporal average 1-point non-uniformity correction (NUC) was made with a room temperature black body at the beginning of each recording.

### *4.2 Results*

The recording of a 5 mm diameter pinhole back illuminated by a 300°C black body is shown in Fig. 7. Figure 7(a) depicts the raw image from one of the 99 angular scans used to reconstruct a TOSCA image, including the 1-point NUC. In Fig. 7(b), the pixels from the imager that are inside a 32 pixel diameter circle are summed up column by column, creating a 1-dimensional projection of the apertured image. The fact that the background appears as a downward curve stems from the fact that the in-band radiation emanating from the mask through emission and reflection is slightly less than that of the room temperature black body, combined with the fact that the number of pixels summed up on the sides is smaller on the sides than in the middle of the curve. Figure 7(c) shows the effect of the ramp filter on the angular scan in Fig. 7(b). Note the amplification of high-frequency components. Figure 7(d) shows the result of back-projecting the filtered signal onto a matrix. The back projection is here done on a 64×64 pixel matrix, using linear interpolation. Figure 7(e) shows the TOSCA reconstruction, the result of summing up all the filtered back projections of the 99 angular scans.

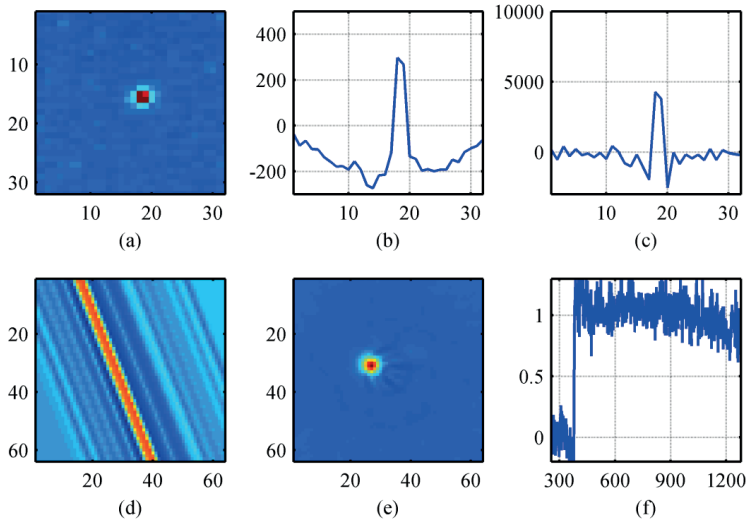


Fig. 7. Recording of a 5 mm diameter pinhole with spin scan TOSCA imager (Media 1). A 300°C black body is behind the pinhole. (a) 32×32 pixel FPA snapshot before software binning to the linear format. One such image is used per angular scan step. The scene image is rotated relative to the FPA at each scan. (b) Columnwise sum of FPA pixels inside a 32 pixel diameter aperture. (c) Ramp filtered detector signal. (d) Back projection of the filtered angular scan. (e) TOSCA image reconstructed from 99 filtered back projections. (f) Normalised temporal variation in the total scene (temporal unit: angular scans).

Two noticeable features are the curved fringe patterns and the otherwise relatively smooth background. Finally, Fig. 7(f) shows the total signal from the scene, each point on this curve representing the sum of the curve in Fig. 7(b), indicating the significant temporal

detector noise in the FPA. The first part of the curve was made with a room temperature blackbody inserted in the optical path, resulting in a step when it was removed. Figures 7-14 all have a similar structure. The curved fringe pattern in the TOSCA reconstruction appears to be extending from the pinhole-to-center axis. The curvature of the fringes is seen to be stronger closer to the axis of rotation. It could be due to a slight decentering of the focal plane array relative to the rotational axis of the rotational scan. It could, however, also be due to the fact that the pinhole is not entirely centred in the scene.

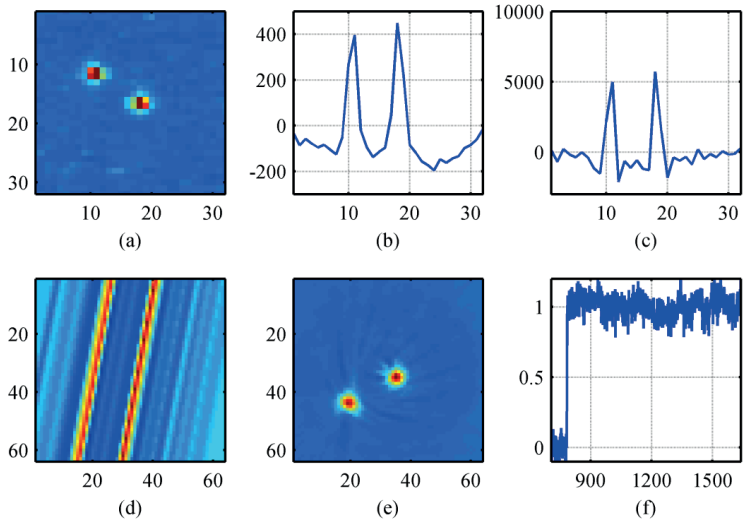


Fig. 8. Double pinhole recording (Media 2). The experiment is similar to that in Fig. 7, but here the target consists of two 5 mm diameter pinholes backlit with a 300°C blackbody. (a) 32×32 pixel FPA snapshot. (b) Columnwise sum of FPA pixels inside a 32 pixel diameter aperture. (c) Ramp filtered detector signal. (d) Back projection of the filtered angular scan. (e) TOSCA image reconstructed from 99 filtered back projections. (f) Normalised temporal total scene variation.

Figure 8 shows the TOSCA reconstruction of the double 5 mm diameter pinhole mask, with a 30 mm center-to-center distance. The almost vertical, straight line observed in the reconstruction is due to temporal signal intensity variations in the scene. Again, a curved fringe pattern appears to emanate from the line between the pinholes and the axis between the pinhole and the optical rotational centre.

Figure 9 shows another double pinhole image with properties similar to that of Fig. 8, but here a 2 mm uncoated germanium window is reducing the contrast with the mask by a factor ~8. Even though the fringe pattern arising from the dominant pinhole, similar to the one in Fig. 7 is significant, it is easy to discern the second, dimmer pinhole.

Figure 10 shows the reconstruction of the Halloween mask, backlit by the 300°C blackbody. The signal is significantly above the noise level of the detector array, as seen by the temporal signal in Fig. 10(f). A circular fringe pattern can be observed in the reconstruction in Fig. 10(e), especially at the forehead, and between the nose and the eyes. This pattern is consistent with the gain/offset patterns seen in Figs. 4(e)-4(f), and suggests that the 1-point NUC made is not sufficient, and that a 2-point NUC is necessary. The pixellation of the triangular shape of the eyes have all but vanished. Structural mouth details are visible.

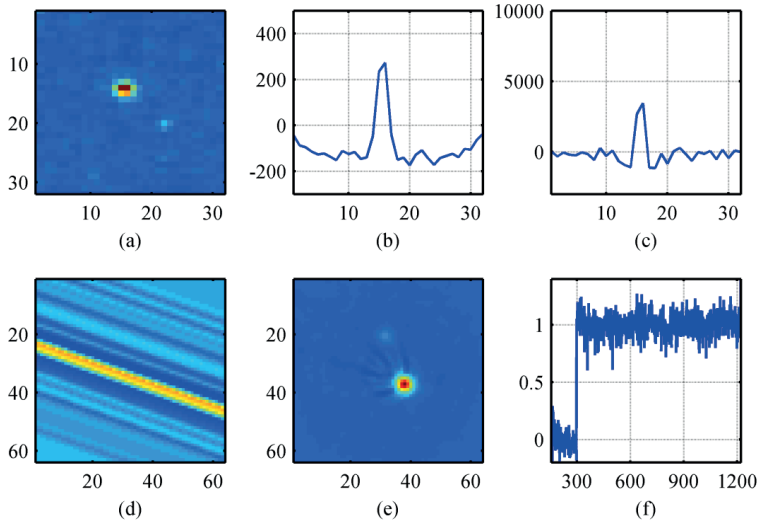


Fig. 9. Double pinhole recording, similar to that in Fig. 8, but with one pinhole covered with an uncoated germanium substrate (Media 3). (a) 32×32 pixel FPA snapshot. (b) Columnwise sum of FPA pixels inside a 32 pixel diameter aperture. (c) Ramp filtered detector signal. (d) Back projection of the filtered angular scan. (e) TOSCA image reconstructed from 99 filtered back projections. (f) Normalised temporal variation in the scene.

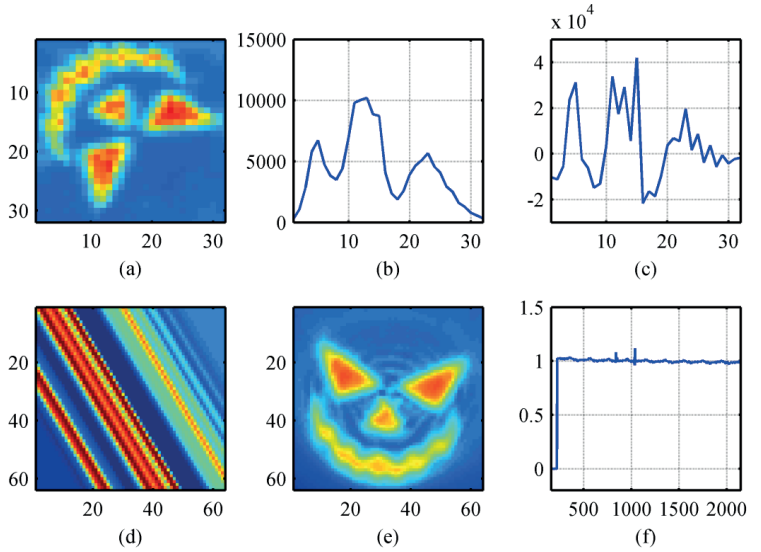


Fig. 10. Recording of Halloween mask backlit by a 300°C blackbody (Media 4). (a) 32×32 pixel FPA snapshot. (b) Columnwise sum of FPA pixels inside a 32 pixel diameter aperture. (c) Ramp filtered detector signal. (d) Back projection of the filtered angular scan. (e) TOSCA image reconstructed from 99 filtered back projections. (f) Normalised temporal total scene variation. The video associated to Figs. 10-14 shows the effect of scene dynamics (rotation).

The Halloween mask reconstruction in Fig. 11 is similar to that of Fig. 10, but with a halogen lamp illuminated copying paper replacing the blackbody backlighting. The signal is much weaker, the (contrast) signal-to-noise level of the FPA frames being only 3-5. This

is an order of magnitude lower than in Fig. 10. A similar fringe pattern is also visible, but weaker. The pixellation of the eyes have again essentially vanished and the mouth structure is recognizable, but the fringe pattern has deteriorated parts of the image, particularly the nose sides. Figure 11(f) shows temporal intensity drift, which may account for part of the deterioration.

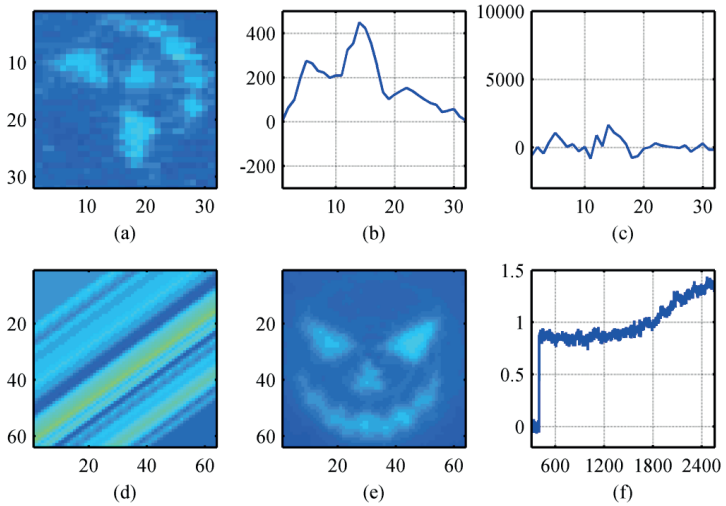


Fig. 11. Recoding of Halloween mask target backlit by halogen lamp illuminated copying paper (Media 5). (a) 32×32 pixel FPA snapshot. (b) Columnwise sum of FPA pixels inside a 32 pixel diameter aperture. (c) Ramp filtered detector signal. (d) Back projection of the filtered angular scan. (e) TOSCA image reconstructed from 99 filtered back projections. (f) Normalised temporal total scene variation.

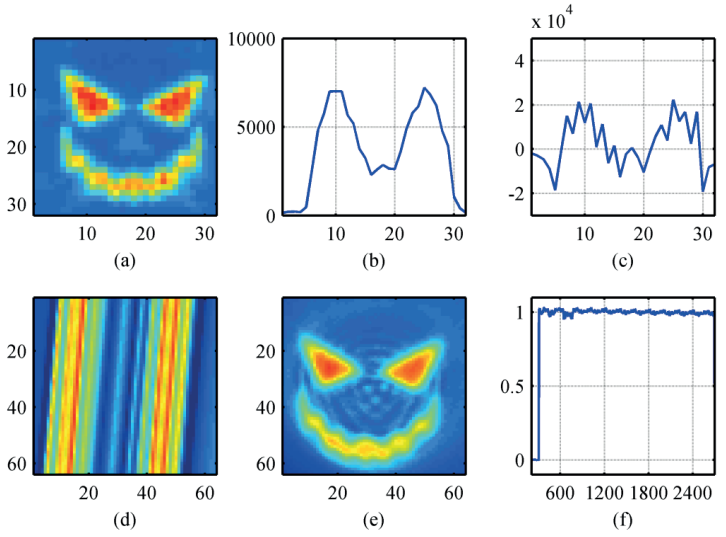


Fig. 12. Recording of Halloween mask target backlit by a 300°C blackbody as in Fig. 10, but with an uncoated germanium substrate covering the nose (Media 6). (a) 32×32 pixel FPA snapshot. (b) Columnwise sum of FPA pixels inside a 32 pixel diameter aperture. (c) Ramp filtered detector signal. (d) Back projection of the filtered angular scan. (e) TOSCA image reconstructed from 99 filtered back projections. (f) Normalised temporal variation in the total scene.

In Fig. 12, the Halloween mask is imaged as in Fig. 9, but with a 2 mm thick uncoated germanium substrate covering the nose of the mask. Two fringe patterns are clearly visible, a circular fringe pattern, and a centrally located approximately triangular interference pattern. The nose section is barely visible in the raw FPA image. Due to the strong interference, the nose is indistinguishable from the fringe pattern in the reconstructed image. With the strong signal the total intensity, shown in Fig. 12(f), shows relatively limited relative variations in the scene intensity integrated over the synthetic circular aperture.

To verify that the fringe pattern is not due to insufficient angular resolution, the experiment in Fig. 12 was repeated, but with more than twice the number of angular steps, from 99 in the previous experiment to 199. The result is shown in Fig. 13. As can be seen in Fig. 13(e), the image is virtually identical to Fig. 12(e), the nose still blurred by the fringe pattern. This shows that the 99 angular scans are not limiting the system imaging properties.

In order to check if the interference pattern could be due to the low number of elements used in the imaging, the 32×32 pixel array was shifted slightly to simulate a 64 linear array by using two frames with an approximate 180° shift to generate an interleaved pattern, as described in section 2.2. The result is shown in Fig. 14. This time the processing was not done live, but post-processed, as the original system software did not have the interleaving algorithm implemented. The setup did not use an exact 180° shift, as 199 angular scans were used to generate the first series of 32 pixel measurements, corresponding to a complete rotation, and 199 angular scans, shifted by 100 samples, were used to generate the second series of measurements. This represents a systematic angular error for the interleaved samples of ½ angular step, or less than 1°. For the central (software binned) detector, this corresponds to a maximum sideways error of ¼ detector pixel unit at the edge. In comparison, the 64 elements synthesized detector pattern has a ½ detector pixel unit separation.

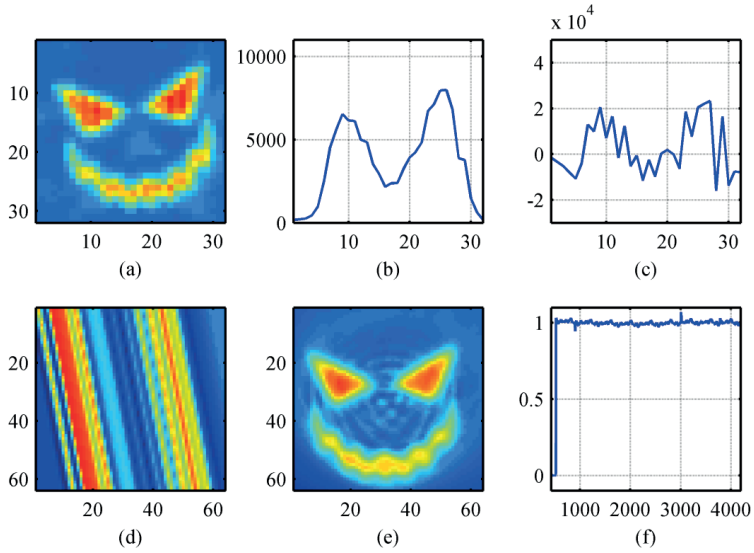


Fig. 13. Recording of Halloween mask with a germanium nose as in Fig. 11, but now using 199 angular scans (Media 7). (a) 32×32 pixel FPA snapshot. (b) Columnwise sum of FPA pixels inside a 32 pixel diameter aperture. (c) Ramp filtered detector signal. (d) Back projection of the filtered angular scan. (e) TOSCA image reconstructed from 99 filtered back projections. (f) Normalised temporal variation in the total scene.

As seen in Fig. 14(a), the stitching of the ~180° images leads to jaggedness due to misalignment. The jaggedness is enhanced by the ramp filter due to its high frequency nature, as seen in Figs. 14(b) and 14(c). The reconstruction in Fig. 14(d) has significant thin circular ring artifacts and, to a lesser degree, Moiré patterns. Specifically, the more pronounced ring pattern as compared to previous reconstructions suggests that there is a considerable low-frequency component in the nonuniformity. A slowly varying responsivity across the array will appear in the processing as alternating high and low values in the interlaced detector element responses.

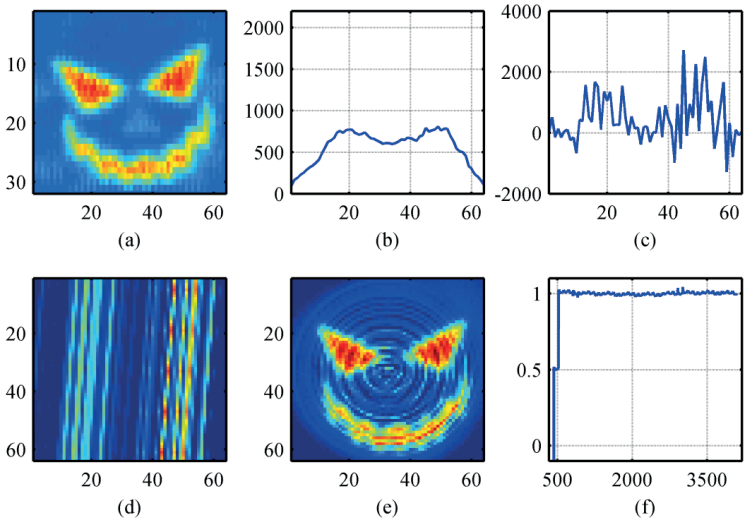


Fig. 14. Recording of Halloween mask with a germanium nose as in Fig. 12, but using two sets of 199 angular scans, shifted by 99 FPA frames (Media 8). (a) 32×64 pixel fusion of two interleaved 32×32 pixel FPA frames, separated by a ~180° field of view rotation. (b) Columnwise sum of FPA pixels inside a 32 by 64 pixel diameter elliptic aperture. (c) Ramp filtered detector signal. (d) Back projection of the filtered angular scan. (e) TOSCA image reconstructed from two 199 filtered back projections, separated by 100 angular scans. (f) Normalised temporal variation in the total scene. The behaviour is peculiar in the beginning due to the 100 sample shift.

Kak and Slaney [4] have indicated that the number of samples per scan and the number of angular scan steps should be approximately equal to give a well-balanced image. A test was made to see the difference as the number of scans was increased. This is shown in Fig. 15, with 3, 5, 9, 11, 33 and 99 scans, respectively. As can be seen, with 3 scans, it is extremely difficult to recognize even very crude aspects of the mask. With 5 scans, it is possible to recognize the mask if given an image. The general outline of the major components becomes visible with around 10 scans, and fine structures become recognizable with 33 scans, approximately equal to the number of detector elements. At 99 scans, the jagged angular aspects of the artifacts have disappeared, at around $\pi$ times the detector count. This corresponds to the aperture perimeter, measured in detector element width units.

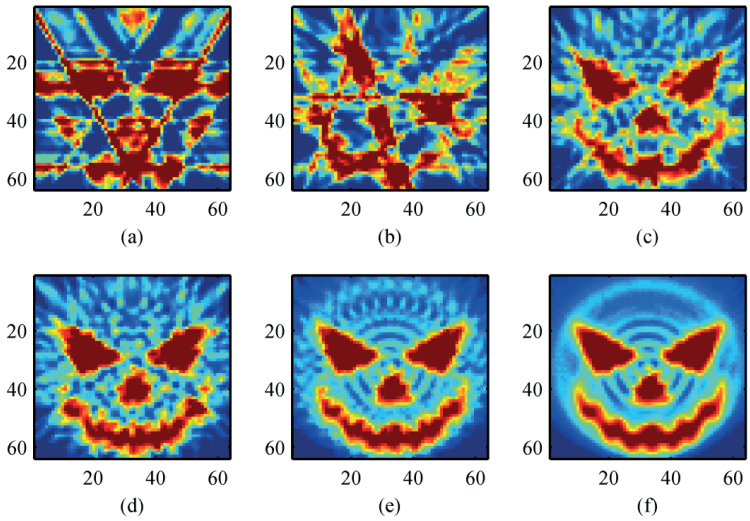


Fig. 15. TOSCA reconstructions of Halloween mask with 32 elements and a varying number of angular scans: (a) 3 scans, (b) 5 scans, (c) 9 scans, (d) 11 scans, (e) 33 scans and (f) 99 scans.

## 5. Discussion

The new spin scan TOSCA imager has demonstrated clear imaging properties, despite the low number of detector elements used in this implementation. An issue with so few elements is that even with a high number of angular scan steps, significant interference fringe patterns will occur, also close to the objects in the scene. One advantage is that the outline of the objects can be relatively accurately represented with a sufficient number of angular steps. With few samples and angular steps for a given desired end resolution, the artifacts will inevitably be of a higher importance than in the case of a high detector count and a large number of angular scans, limiting faithful reproduction of features in images with high dynamics. Complexity also affects this capability. In the reconstructions in Figs. 7-9, the artifacts are relatively easy to separate from the scene features, even with order of magnitude variation in contrast. With the more complex scenarios seen in Fig. 10 onwards, however, the artifacts accumulate, deteriorating low contrast features beyond recognition. The main frequency component of the artifact ripples had frequency values close to the Nyquist limit of the detector array density. Increasing the number of angular steps in this scenario proved to not add significant enhancements, as, at 99, the number of steps was already ~$\pi$ times the number of the 32 detector elements across the field of view. This showed that the main reason for the artifacts was the limited number of detector elements.

It was initially assumed that shifting the detector array sideways ¼ pixel would enable a doubling of the resolution and hence reduce the artifacts somewhat. However, in the experiment with this implementation several hurdles were encountered that actually degraded the image compared to the results achieved without the stitching. One hurdle was the difficulty with doing sub-element alignment, creating jaggedness in the sensor image, and the other was the detector nonuniformity.

The circular artifacts highlight the need for good sensor uniformity. In this demonstrator, a 2-point NUC could have reduced the magnitude of the artifacts, but in a linear detector array configuration, inhomogeneities within each detector cannot be taken away directly using a simple 2-point NUC. In principle, vignetting could also affect system nonuniformity, but if the vignetting effect is circularly symmetrical to the field of view, it

can easily be compensated for after the reconstruction. Some inhomogeneities could also stem from stray light entering the camera, partly because the scan mechanism was made out of reflective materials. Evidence of this is difficult to assess in the still images, but some are visible in the videos, in particular the videos depicting the pinhole masks. Another less problematic issue was the synthetic aperture used, which had a different resolution in the two directions. This would represent less of a problem here, however, as the Halloween mask is homogeneous outside the facial features. Another issue that was not tested here is that the interleaving structure presented at the end would be particularly vulnerable to temporally changing scenes.

## 6. Conclusion

This paper presents the first spin scan tomographic scanning (TOSCA) imager, together with several optical scanning solutions. An uncooled imager operating in the 1.8-5.0 μm mid-infrared spectral range was demonstrated. The system here used a camera structure with a resistor network readout electronics limiting the readout to 100 angular scans per second, but a dedicated sensor architecture should be able to operate at least one to two orders of magnitude faster. With 32 line detectors and 99 angular steps, the system was able to image simple scenes with contrast dynamics of about one order of magnitude. In very complex scenes, though, this was proven to be insufficient due to artifacts accumulating. The artifacts observed were mainly due to a limited number of detector lines, combined with nonuniform detector responsivity.

An attempt was made to double the imaging resolution by using a ¼ pixel detector offset, combined with 180° detector shift, interleaving the resulting signals. Several hurdles were making this particular implementation less successful. Allthough images were produced, the resulting quality was degraded, mainly due to errors provoked by the interleaved fusion of the two images, rotated relative to each other.

Detailed physics-based simulations were used to identify the effect of error sources such as misalignment, temporal sampling errors and scan speed variations. The analysis identified the need for a precise angular reference, but initial simulations indicated that it might not be necessary to have detailed angular position readout for each sample, provided rotational inertia is significant. Simulations and experiments also highlighted the sensitivity to nonuniform detector responsivity. The corrections to the nonuniformities are not trivial and hence put requirements on detector quality. The proposed configuration has some limitations in pure imaging with high contrast due to a low number of angular scan orientations creating characteristic curved or circular line artefacts, but is sufficient if objects of interest are located on an otherwise homogeneous background. Measurements using the experimental setup verified performance predicted through theory and simulations.

**Acknowledgments**
The author is grateful to Prof Svein Erik Hamran and Dr Torbjørn Skauli for helpful discussions and able guidance, and to Mr Pål Halvorsen for doing the SolidWorks implementation of the camera design.